

**INVESTIGATION OF DEEP FOUNDATIONS AT THE SPRING VILLA NATIONAL
GEOTECHNICAL EXPERIMENTATION SITE**

by

Chao Shi

A thesis submitted to the Graduate Faculty of
Auburn University
in partial fulfillment of the
requirements for the Degree of
Master of Science

Auburn, Alabama
May 5, 2018

Keywords: GIS database, Spring Villa NGES, Drilled shafts, Numerical simulation

Copyright 2018 by Chao Shi

Approved by

Jack Montgomery, Chair, Assistant Professor of Civil Engineering
J. Brian Anderson, Associate Professor of Civil Engineering
Marta Miletic, Assistant Professor of Civil Engineering

ABSTRACT

The Spring Villa test site is a National Geotechnical Experimentation Site located near Opelika, Alabama and managed by Auburn University. The test site is located at the southern end of the Piedmont geologic province and is underlain by residual silts and sands which grade with depth into partially weathered rock. The site has been extensively characterized through borings, penetration tests and geophysical tests. Several types of deep foundations, for instance pipe piles, H-piles and drilled shafts, have previously been installed at the Spring Villa test site and many have been load tested. This combination of characterization and foundation data at a single site makes the Spring Villa site a unique location to test new characterization methods and develop correlations to load test data in residual soils. However, there is no comprehensive database to summarize the foundation and in-situ test locations and the results from the various tests. This thesis will provide a new publicly available GIS database which contains the locations of foundation and in-situ tests and a summary of results from the in-situ and load tests. The site history and geology of Piedmont residual soils are briefly described. The final map with the location for each deep foundation and in-situ test of the GIS database and the previous load test results in the attribute table of the GIS database are provided.

The second part of this thesis describes the three-dimensional numerical modeling of a new non-destructive testing method for the drilled shafts at the Spring Villa test site. The preliminary models consider a single drilled shaft with the same material properties and dimensions as the drilled shafts located at the Spring Villa test site. The shaft is modeled using the commercial finite difference software FLAC 3D. The non-destructive test is simulated by applying a sinusoidal force

to the side of the upper portion of the drilled shaft and the acceleration time history of four different points are recorded. Simulations are performed using different loading frequencies and three different shaft lengths. The properties of the concrete and soil are also varied to see the effect on the response. The results from these models will be analyzed by future researchers in order to identify correlations and assist with the design of a field testing procedure. The database and the numerical results described in this thesis should make it possible for future researchers to better utilize the Spring Villa site to develop and test methods for evaluating deep foundations in residual soils.

ACKNOWLEDGMENTS

I would like to thank the Highway Research Center at Auburn University for providing funding for this research project. I would also like to acknowledge my committee chair, Dr. Jack Montgomery for his encouragement and support. I would also like to acknowledge my committee members, Dr. J. Brain Anderson and Dr. Marta Miletic. I would also like to thank the following people for their help with this project: Matt Barr, Jonathan Hogan, Michael Kiernan, Hongyang Wu and Dakota Basham. Finally, I would like to thank my family for their support and encouragement.

CONTENTS

ABSTRACT	ii
ACKNOWLEDGMENTS	iv
LIST OF FIGURES	ix
LIST OF ABBREVIATIONS AND SYMBOLS	xi
CHAPTER 1: INTRODUCTION	1
1.1 Background	1
1.2 Objective	2
1.3 Scope of Work	2
CHAPTER 2: BACKGROUND AND LITERATURE REVIEW	4
2.1 Site History	4
2.2 Site Geology	6
2.3 In-situ tests	8
2.4 Types of Deep Foundations	11
2.4.1 Pile Groups	12
2.4.2 Drilled Shafts	18

2.4.3 H-Pile Bents.....	23
CHAPTER 3: DESCRIPTION OF THE GIS DATABASE	26
3.1 Location Survey at Spring Villa Test Site.....	26
3.2 Convert Coordinates into GIS Database.....	27
3.3 Description of Attribute Table for Foundation Layers	28
3.3.1 Drilled Shafts.....	28
3.3.2 Pile Groups.....	31
3.3.3 H-Pile Groups	31
3.3.4 Other Foundations.....	33
3.4 In-Situ Test Layers and their Attribute Tables in the GIS Database	33
3.5 Limitation of this database.....	49
CHAPTER 4: NUMERICAL MODELLING OF THE DRILLED SHAFT.....	50
4.1 Introduction	50
4.2 Background.....	51
4.2.1 Overview of Non-Destructive Test Method.....	51
4.2.2 Numerical Simulation of Non-Destructive Test.....	52
4.3 Numerical Simulation	52
4.3.1 FLAC 3D	53
4.3.2 Shaft and Soil Properties	53
4.3.3 Geometry of the Simulations	55

4.3.4 Equilibrium Stress-State of the Simulations	58
4.3.5 Dynamic Analysis of the Simulations.....	60
4.4 Simulation Results.....	62
4.5 Discussion.....	70
CHAPTER 5: CONCLUSIONS AND FUTURE DIRECTION	72
5.1 GIS Database Summary	72
5.2 GIS Database Conclusion	72
5.3 Numerical Simulations Summary.....	73
5.4 Numerical Simulations Conclusion	74
5.5 Recommendations for future research	74
REFERENCES.....	76
APPENDIX A: ACCELERATION TIME HISTRIES FOR THE NUMERICAL SIMULATIONS	78
APPENDIX B: POWER SPECTRAL DENSITIES FROM THE NUMERICAL SIMULATIONS	108

LIST OF TABLES

Table 1. References for the in-situ tests performed at the Spring Villa Test Site.....	11
Table 2. References for the foundations currently installed at the Spring Villa Test Site.....	12
Table 3. Summary of load test results on the CFA piles (Brown and Drew 2000).....	13
Table 4. Properties of the drilled shafts.	20
Table 5. Applied load for LVDT measurement of tested shafts (Simpson and Brown 2003).....	21
Table 6. Applied load for inclinometer measurement of tested shafts (Simpson and Brown 2003).	22
Table 7. Surveyed coordinates from the Spring Villa test site	27
Table 8. Baseline material properties for the drilled shaft simulations.....	54
Table 9. Stiffness for the concrete and the soil from case 1 to case 7.....	55
Table 10. Summary of frequency and property combinations for all simulations.....	61

LIST OF FIGURES

Figure 1. Map showing the location of the Spring Villa National Geotechnical Experimentation Site (NGES). Street map from ESRI (2015).	4
Figure 2. The NCAT test track facility (NCAT 2009).	5
Figure 3. The Spring Villa NGES in August 2017, looking northwest across the site (photo courtesy of Dakota Basham).	6
Figure 4. The geographic extent of the Piedmont residual soil region (Mayne et al. 2000).	7
Figure 5. Detailed in-situ tests location at NGES (Vinson and Brown 1997).	9
Figure 6. Surveyed map of CPT tests location at NGES (Vinson and Brown 1997).	10
Figure 7. Composite load deflection plot for the CFA piles installed in groups (TP1 and TP2) and isolated (TP3-TP5) (Brown and Drew 2000).	13
Figure 8. Photo of the 5-pile group looking from east to west taken in March 2018.	14
Figure 9. Numbering of the 9-pile group (Brown et al. 2001).	15
Figure 10. Photo of 9-pile group looking from west to east taken in March 2018.	16
Figure 11. Load vs. Displacement for 9-pile group (Brown et al. 2001).	16
Figure 12. Bending moment profiles for pile 4, 10, 11 of 9-pile Group (Brown et al. 2001).	17
Figure 13. Bending moment profiles for pile 5, 6, 13 of 9-pile Group (Brown et al. 2001).	17
Figure 14. Layout of drilled shafts with other in-Situ test (Simpson and Brown 2003).	19
Figure 15. Photo of drilled shafts looking from south to north taken in March 2018.	19
Figure 16. Photo of drilled shafts looking from north to south taken in March 2018.	20
Figure 17. Lateral deflection vs Depth from inclinometer tests for shaft 1 (Simpson and Brown 2003).	23
Figure 18. Battered bent, taken from north to south (Marshall et al. 2017).	24
Figure 19. Vertical bent, taken from south to north (Marshall et al. 2017).	25
Figure 20. GR-3™ GPS receiver, Topcon FC-200 and operator's manual for survey (Topcon Positioning Systems, Inc.).	26
Figure 21. The first segment of the attribute table for the drilled shaft layer.	29
Figure 22. Load vs Deflection from LVDT data (Simpson and Brown 2003).	29
Figure 23. The second segment of the attribute table for the drilled shaft layer.	30
Figure 24. The third and final segment of the attribute table for the drilled shaft layer.	30
Figure 25. The attribute table of the pile group layer.	31
Figure 26. The first segment of the attribute table for the two bents layer.	32
Figure 27. The final segment of the attribute table for the two bents layer.	32
Figure 28. The attribute table of H pile layer.	33
Figure 29. The attribute table of pipe pile layer.	33
Figure 30. The first segment of the attribute table for the crosshole seismic testing layer.	34
Figure 31. The second segment of the attribute table for the crosshole seismic testing layer.	35
Figure 32. The result of sounding jag01 (Georgia Tech 2000).	36
Figure 33. The result of sounding jag02 (Georgia Tech 2000).	37
Figure 34. The result of sounding jag03 (Georgia Tech 2000).	38

Figure 35. The result of sounding jag04 (Georgia Tech 2000).	39
Figure 36. The first segment of the attribute table for the Georgia Tech CPTs.	39
Figure 37. The final segment of the attribute table for the Georgia Tech CPTs.	40
Figure 38. The first segment of the attribute table for the PMT layer.	40
Figure 39. The second segment of the attribute table of PMT layer.	41
Figure 40. The third and final segment of the attribute table of PMT layer.	41
Figure 41. The first segment of the attribute table for the SPT layer.....	41
Figure 42. The final segment of the attribute table for the SPT layer.....	42
Figure 43. The first segment of the attribute table for the CPT layer.	42
Figure 44. The second segment of the attribute table for the CPT layer.....	43
Figure 45. The third and final segment of the attribute table for the CPT layer.	44
Figure 46. The attribute table of seismic CPT layer.	44
Figure 47. The first segment of the attribute table for the borehole shear test layer.....	45
Figure 48. Borehole shear test results from Vinson and Brown (1997).....	45
Figure 49. The second segment of the attribute table for the borehole shear test layer.....	46
Figure 50. The third segment of the attribute table for the borehole shear test layer.	46
Figure 51. The fourth and final segment of the attribute table for the borehole shear test layer. .	46
Figure 52. The result summary of DMT from Vinson and Brown (1997).....	47
Figure 53. The attribute table of DMT layer.	47
Figure 54. The result summary of seismic DMT from Vinson and Brown (1997).....	48
Figure 55. The attribute table of seismic DMT layer.	48
Figure 56. Model of drilled shaft grid and the soil grid for 11-meter shaft length simulation.	56
Figure 57. Model of the drilled shaft in soil for 11-meter shaft length simulation.....	57
Figure 58. Model of the drilled shaft in soil for 8-meter shaft length simulation.	58
Figure 59. Model of the drilled shaft in soil for 6-meter shaft length simulation.	58
Figure 60. Contours of the initial equilibrium stress-state for 11-meter shaft length simulation. 59	
Figure 61. Contours of the initial equilibrium stress-state for 8-meter shaft length simulation.. 60	
Figure 62. Contours of the initial equilibrium stress-state for 6-meter shaft length simulation.. 60	
Figure 63. Cross-section through the center of the shaft showing the location of recording points.	62
Figure 64. Plan view of half of the shaft showing the locations of the recording points.	62
Figure 65. Acceleration time histories for three directional components and a loading frequency of 60 Hz. Simulation results for an 11 m shaft length with the baseline properties.....	63
Figure 66. Power spectral densities for x acceleration at point 1 on the 11 m shaft over a wider range (a) and a narrower range (b) of frequencies.	65
Figure 67. Power spectral densities for point 1 on the 11 m shaft using the y-acceleration (a) and z-acceleration (b) time histories.....	65
Figure 68. Median power spectral densities for the 11 m shaft using each of the acceleration components for points 1 (a), 2 (b), 3 (c) and 4 (d).....	67
Figure 69. Median power spectral densities are shown for acceleration in the z-direction at point 3 using the baseline properties and three shaft lengths.....	68
Figure 70. Median power spectral densities are shown for acceleration in the z-direction at point 3 using the 8 m shaft and three sets of properties.	69
Figure 71. Median power spectral densities are shown for acceleration in the z-direction at point 3 using the 8 m shaft and five sets of properties.....	70

LIST OF ABBREVIATIONS AND SYMBOLS

ALDOT	Alabama Department of Transportation
BST	Borehole Shear Test
CFA	Continuous Flight Auger
CHT	Crosshole Test
CPT	Cone Penetration test
CPMT	Cone Pressuremeter Test
DMT	Dilatometer test
FHWA	Federal Highway Administration
GIS	Geographic Information System
IFCEE	International Foundations Congress and Equipment Expo
LVDT	Linear Variable Differential Transformers
NCAT	National Center for Asphalt Technology
NCHRP	National Cooperative Highway Research Program
NDT	Non-Destructive Test
NGES	National Geotechnical Experimental Site
NSF	National Science Foundation
PCPT	Piezocone Penetration Test
PMT	Pressuremeter Test
PSD	Power Spectral Density
SCPT	Seismic Cone Penetration Test

SDMT	Seismic Dilatometer Test
SPT	Standard Penetration test
TPS	Topcon Positioning Systems

CHAPTER 1: INTRODUCTION

1.1 Background

The Piedmont geologic province underlies large population centers in the eastern United States as it runs from New Jersey to east Alabama. The Spring Villa National Geotechnical Experimental Site (NGES) is located at the southern end of the Piedmont province near Opelika, Alabama and managed by Auburn University. The Spring Villa test site is underlain by residual silts and sands near the surface which transition into partially weathered rock at depth (Sowers and Richardson 1983). The soil properties of the Piedmont residual soil are unique and important for geotechnical design in many parts of the eastern United States. Several researchers have performed in-situ tests and foundation load tests at this test site. Vinson and Brown (1997) performed different types of in-situ tests to determine the soil properties of the Piedmont residual soil, including Standard Penetration tests (SPT), Cone Penetration tests (CPT), and Dilatometer tests (DMT). Mayne et al. (2000) summarized the characterization of the Piedmont residual soil in their research at the Spring Villa test site, including data from four additional CPTs. Brown (2002) and Simpson and Brown (2003) described the construction of ten drill shafts and performed six full-scale lateral load tests to develop p-y curves for laterally loaded piles in the Piedmont residual soil. Marshall et al. (2017) described load tests on two H-pile bents at the test site.

Despite this large number of studies, there is no comprehensive database for the Spring Villa test site that includes the test results and locations for these in-situ tests and foundations. In order to compile the data from previous research into a single location, a Geographic Information System (GIS) database was developed. This database includes the coordinates of deep foundations, previous load test results, in-situ test locations and summarized in-situ test results.

The Spring Villa test site also serves as a unique location for the development of new

methods to perform and analyze non-destructive tests due to the variety of foundations installed in one well characterized location. This thesis describes the use of numerical simulations to examine the response of a drilled shaft to low amplitude dynamic loading. Simulations are performed for shafts of different lengths and variations in properties.

1.2 Objective

The primary objective of this research was to develop a GIS database which combines the results of in-situ tests and foundation tests from previous research papers in a single location, that can be easily updated by future researches. A secondary objective was to use the information in this database to examine the response of a drilled shaft to low amplitude sinusoidal loading using numerical simulations.

1.3 Scope of Work

To accomplish the first of these objectives, the coordinates of all existing foundations were surveyed at the Spring Villa test site. Information from previous studies was collected and the test results were included in the database. The final GIS database presented the locations, in-situ test types, foundation types and all load test results, while including some pictures and links to original documents. This thesis provided the background information and relevant literature review on the history of the Spring Villa test site and summarized results from previous studies. The procedure of making each layer and each column in this database for each in-situ test or foundation layers was described and abbreviations used for column names were defined. Discussion of the results and limitations are discussed.

The second objective was accomplished through the development of a three-dimensional (3D) numerical model of a single drilled shaft. This model was then used to examine the response of the shaft to low amplitude sinusoidal loading. This loading replicates the type of loading that

might be applied during a dynamic non-destructive test on a drilled shaft. The response of the shaft was examined for three shaft lengths and variations in the properties of both the shaft and soil. Based on the results of these simulations, modifications to previous testing procedures are proposed.

Portions of this thesis have been published in the proceedings of the 2018 International Foundations Congress and Equipment Expo (IFCEE). The reference for this paper is Montgomery et al. (2018).

CHAPTER 2: BACKGROUND AND LITERATURE REVIEW

2.1 Site History

The Spring Villa test site was established on land purchased by Auburn University, the Auburn University Highway Research Center and the National Center for Asphalt Technology (NCAT) to establish a pavement test track facility (Vinson and Brown 1997). The facility is located southeast of Opelika, Alabama near the community of Spring Villa. The Spring Villa NGES provides a place for full-scale field research of in-situ tests and foundation load tests. The Spring Villa test site was funded by the National Science Foundation (NSF) and the Federal Highway Administration (FHWA). This test site is available for geotechnical researchers to develop new techniques for soil characterization and foundation construction. The site also allows geotechnical researchers to perform in-situ tests to determine the properties of Piedmont residual soils. Figure 1 presents a map of the Spring Villa test site location.

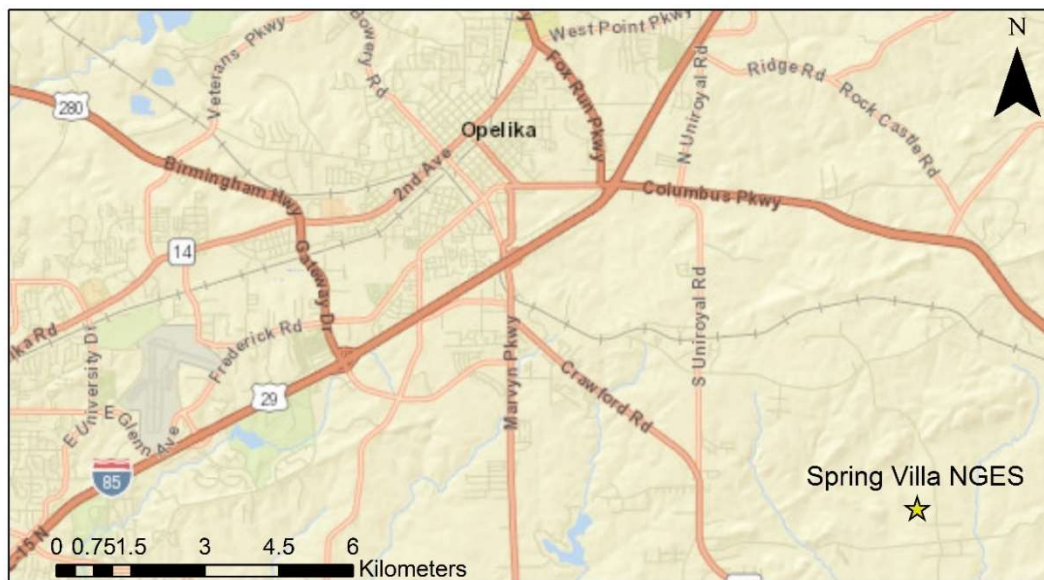


Figure 1. Map showing the location of the Spring Villa National Geotechnical Experimentation Site (NGES). Street map from ESRI (2015).

Original characterization of the geotechnical site began in 1996 and was completed prior to the first drilled shafts being installed in 1997 (Vinson and Brown 1997). Figure 2 shows the entire test track area including the Spring Villa NGES (NCAT 2009). Cone penetration tests (CPTs) were used for initial exploration of the site and a one-acre area was selected to the southeast of the test track that was found to be relatively homogeneous. This one-acre area is referred to as the Spring Villa test site and a recent aerial photo of the site is shown in Figure 3. Deep foundations currently installed at the site include ten drilled shafts, four single pipe piles, two single H-piles, a pipe pile group, a continuous flight auger (CFA) pile group and two H-pile bents. Details of each of these foundations are discussed in subsequent sections. There are also a variety of concrete slabs and structures at the site which have been constructed for non-geotechnical projects and are not described in this thesis. There are some areas of the site which have been excavated and replaced during removal of drilled shafts installed by Mullins and Ashmawy (2005) and again during construction of two test trenches by Burrage (2016). As these features are no longer present at the site, they have not been included in the current database.



Figure 2. The NCAT test track facility (NCAT 2009).



Figure 3. The Spring Villa NGS in August 2017, looking northwest across the site (photo courtesy of Dakota Basham).

2.2 Site Geology

The Spring Villa test site is located at the southern end of the Piedmont geologic province. Several major cities and large population centers in the eastern United States from New Jersey to east Alabama are underlain by this province. Figure 4 presents the extent of the Piedmont province along the eastern United States and the major cities, such as Philadelphia, Washington, D. C., Charlotte and Atlanta, in this region (Mayne et al. 2000). The Spring Villa test site, is located at the southern end in this map (labeled as the Opelika test site).

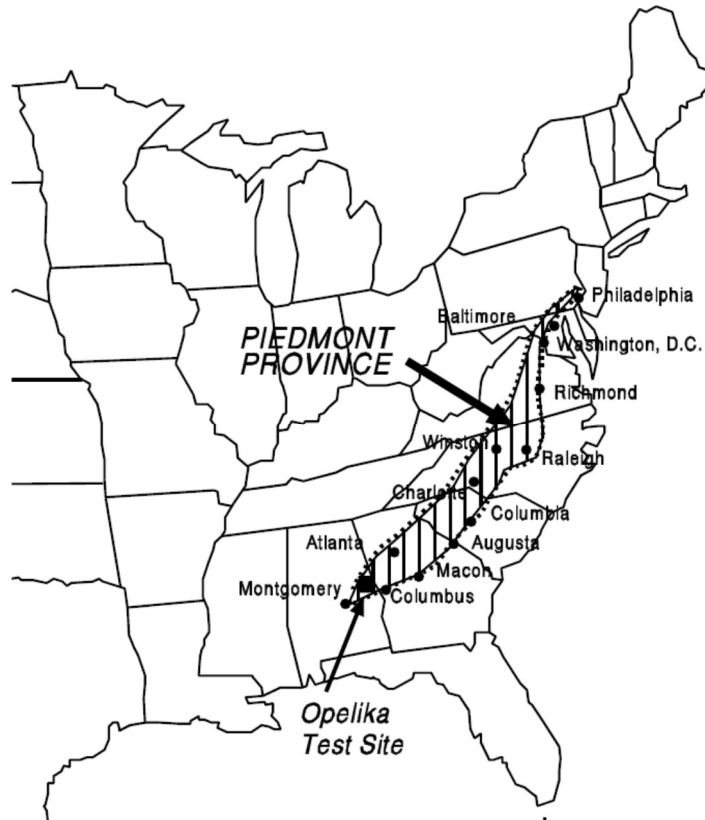


Figure 4. The geographic extent of the Piedmont residual soil region (Mayne et al. 2000).

The residual soils at the Spring Villa NGES range from sandy silt to silty sand which grades into partially weathered rock (Mayne et al. 2000). The Piedmont residual soil is originally formed by the weathering of ancient mountains, which have been decomposed and eroded to form rolling terrain and hillsides (Mayne et al. 2000). The Piedmont residual soil is challenging for geotechnical engineers, because the soil presents characteristics of both fine-grained soils and coarse-grained soils properties depending on the loading (Mayne et al. 2000). This makes the Piedmont residual soil different than other soils and unique for geotechnical design and construction.

The water table at the Spring Villa test site can fluctuate, but on average is located 2 to 3 m below the ground surface. Mayne and Brown (2003) mentioned the water table was about 4.5

meters deep in May 2002. Quartz sand seams and weathered mica schist are prevalent across the site (Vinson and Brown 1997).

2.3 In-situ tests

Vinson and Brown (1997) documented the largest characterization effort of the site, including the results of several different types of in-situ and laboratory tests. These tests included the Standard Penetration tests (SPTs), Cone Penetration tests (CPTs) which also including piezocone (PCPT), conventional Menard pressuremeter tests (PMTs), cone pressuremeter tests (CPMTs), Dilatometer tests (DMTs) and Iowa borehole shear tests (BSTs). They also presented results from several crosshole tests (CHTs), seismic cone penetration tests (SCPTs) and seismic dilatometer tests (SDMTs) to measure the shear wave velocity (Vinson and Brown 1997). Vinson and Brown (1997) performed consolidated undrained triaxial and unconsolidated undrained tests to determine drained and undrained strength parameters. The Atterberg Limits, water contents, unit weights, grain size distributions and soil classifications were also determined (Vinson and Brown 1997).

The locations of four SPTs, six CHTs, two seismic CPTs, fourteen CPTs, four CPMTs, two Menard PMTs and two BSTs presented in Figure 5 (Vinson and Brown 1997). The full survey of the area along with the locations of the CPTs used for the original characterization is shown in Figure 6 (Vinson and Brown 1997). Table 1 summarizes the in-situ test type, author of the source paper and the boring or sounding number where the test was performed.

Georgia Tech also performed additional CPT tests during two separate studies (Georgia Tech 2000 and McGillivray 2007) at the Spring Villa test site. Several of these tests were seismic CPT tests. These test locations were provided as latitude and longitude by the authors of those

studies and the names of these soundings are listed in Table 1. Georgia Tech researchers performed additional CPT tests at the Spring Villa test site in 2016 which will be added to the database when published.

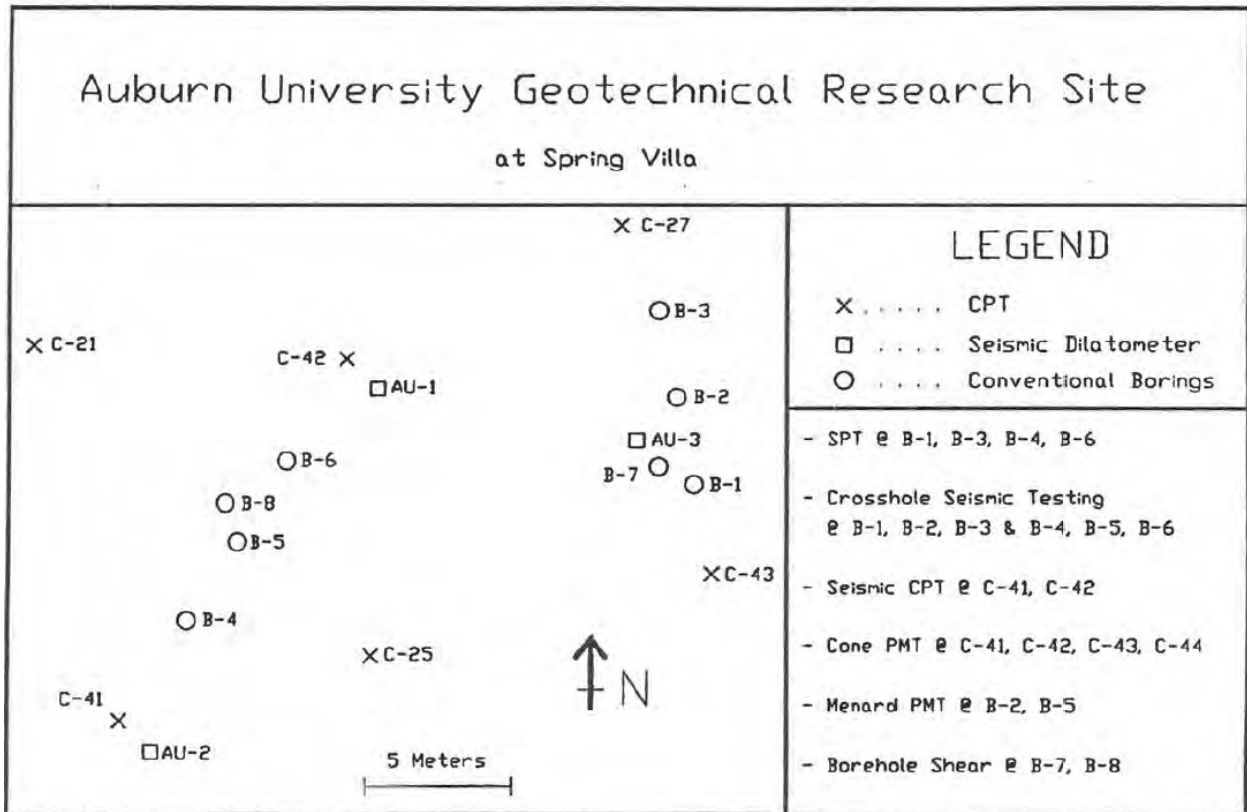


Figure 5. Detailed in-situ tests location at NGES (Vinson and Brown 1997).

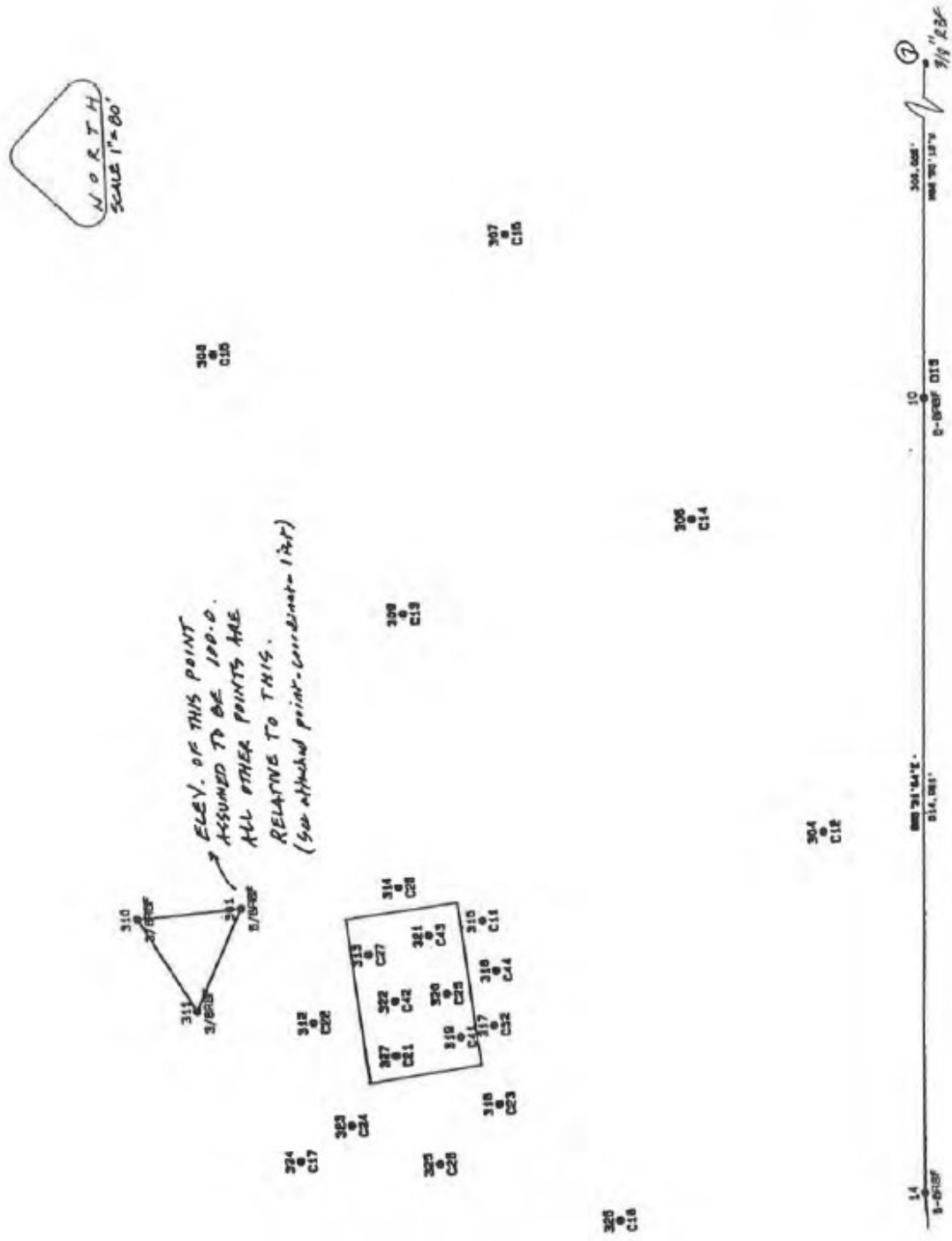


Figure 6. Surveyed map of CPT tests location at NGES (Vinson and Brown 1997).

Table 1. References for the in-situ tests performed at the Spring Villa Test Site.

Reference	Test Type	Test Name
Vinson and Brown (1997)	Standard Penetration Test	B-1, B-3, B-4, B-6
	CPT/Seismic CPT	C-11, C-13, C-14, C-17, C-21, C-23, C-25, C-27, C-28, C-32, C-41, C-42, C-43, and C-44
	Dilatometer/ Seismic Dilatometer Test	AU1, AU2, AU3
	Pressuremeter Test	C-41, C-42, C-43, C-44 and B-2, B-5
	Crosshole Seismic Test	B-1, B-2, B-3 and B-4, B-5, B-6
	Iowa Borehole Shear Test	B-7, B-8
Georgia Tech (2000)	CPT/Seismic CPT	jag01, jag02, jag03 and jag04
McGillivray (2007)	Seismic CPT	OPETRU, OPETRUSEIS, OPEAUT and OPELI2

2.4 Types of Deep Foundations

The Spring Villa test site was originally established as a test site for deep foundations in residual soils. To support this mission, several types of deep foundations were installed at the site and many were load tested in some manner. Brown and Drew (2000) constructed one 5-pile group (CFA piles) at the test site and performed the standard static axial compressive load test (ASTM D1143) for those piles. Brown et al. (2001) documented the construction a 12-pile group which, after load testing, was removed and re-driven as a 9-pile group. The static lateral load tests and dynamic load tests were performed for each pile group. Brown (2002) documented the construction of ten drilled shafts at the test site. These ten drilled shafts are all approximately 0.91 m (36 inches) in diameter and 11 m (36 feet) deep with an additional 0.3 m (1 foot) of stick-up above the ground surface. Marshall et al. (2017) constructed two H-pile bents at the test site and performed load tests on these two bents. Additional details on each of these foundations is

presented in the following sections. Table 2 lists the foundations which currently remain at the site and were previously load tested in some manner.

Table 2. References for the foundations currently installed at the Spring Villa Test Site.

Reference	Type of Foundation
Brown and Drew (2000)	One 5-pile group (CFA piles)
Brown et al. (2001)	One 9-pile group (pipe piles) and a single pipe pile
Brown (2002)	Ten drilled shafts
Marshall et al. (2017)	Two H-Pile bents

2.4.1 Pile Groups

Brown and Drew (2000) described the construction and testing of a pile group made up of five 0.46-meter diameter DeWaal piles (displacement-type CFA piles) and a reinforced concrete pile cap. Brown and Drew (2000) installed two pile groups with different IDs ranging from TP1 to TP2 and three individual piles with ID numbers from TP3 to TP5. The installation for these five piles were different. TP1 and TP2 were grouped at 3-diameter spacing, in which the tested piles were at the center of the 5-pile group. TP1 also used sand during drilling to improve the pile-soil interface. Unfortunately, it is not clear which of these two groups remains at the site, so the exact properties are unknown. For both groups, the center pile was tested using a static axial load. The four surrounding piles were not tested. It is not clear when the pile cap was added or whether the piles were tested as a group. TP 3,4, and 5 were isolated single piles which were tested without adjacent piles. The standard static axial compressive load tests (ASTM D1143) were performed for each of tested piles. The pile ultimate capacity and average shaft friction are summarized in Table 3 and the load deflection curves are shown in Figure 7 (Brown and Drew 2000). Figure 8

displays the recent picture of this 5-pile group. The concrete cap can be clearly seen, but the individual piles are not visible in the picture.

Table 3. Summary of load test results on the CFA piles (Brown and Drew 2000).

ID	D	L	Ult. Capacity	$F_{s,AVG}$
	(m)	(m)	(kN)	(kPa)
TP1	0.46	8.2	1250	105
TP2	0.46	11.6	1500	91
TP3	0.46	11.0	710	45
TP4	0.46	7.6	760	68
TP5	0.46	8.2	670	56

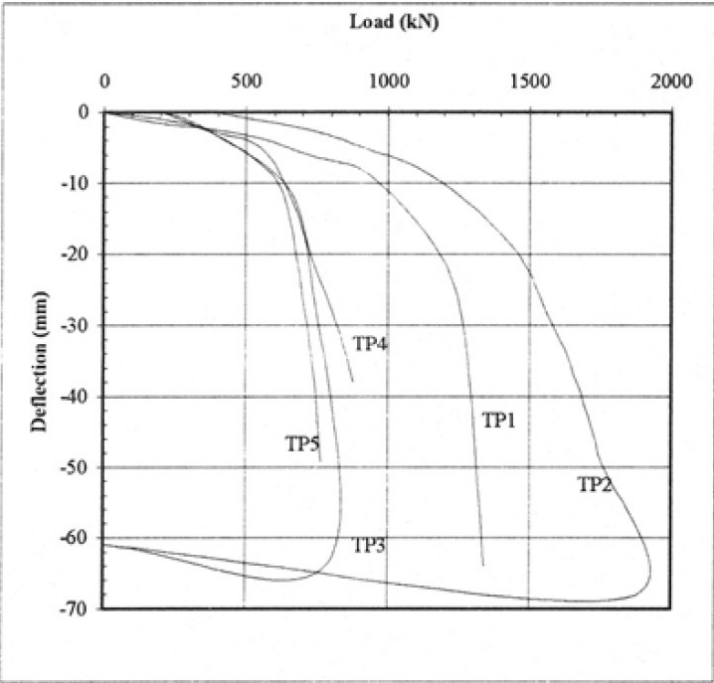


Figure 7. Composite load deflection plot for the CFA piles installed in groups (TP1 and TP2) and isolated (TP3-TP5) (Brown and Drew 2000).



Figure 8. Photo of the 5-pile group looking from east to west taken in March 2018.

Brown et al. (2001) describe the installation and testing of two pipe pile groups as part of a NCHRP study on lateral loading of pile groups. Thirteen instrumented steel pipe piles (0.27 m diameter and 12 m long) were used for the study. A 12-pile group and adjacent single pile was driven first and laterally load tested. The pile group was installed at a spacing of 3 diameters (center to center). The loading sequence was as follows: a static lateral load test was performed on the group using the DeWaal group (TP1 or TP2) as a reaction; dynamic loading of the group was performed in the opposite direction using a rapid load test; a static lateral load test was performed on the single pile using the pipe pile group as a reaction.

All thirteen piles were then extracted and the piles were re-driven as a 9-pile group with a reinforced concrete cap and a single pile adjacent to the group. A vibratory hammer was used to extract the piles, but approximately 0.5m from the top of each pile were removed after extraction because this portion was damaged by the hammer. The group and single pile were laterally tested after being re-driven using the same sequence described above. The three leftover piles were re-driven near the drilled shafts, but were not load tested. Each pile in the 9-pile group was numbered and the numbering is shown in Figure 9. A recent picture of this 9-pile group is presented in Figure 10. New numbers were spray painted on the piles during the tests performed by Marshall et al. (2017) and, do not match the numbers from Brown et al. (2001). The deflection response during load testing was measured for each pile group and the results from 9-pile group are shown in Figure 11 (Brown et al. 2001). The interpretation of strain measurements of 9-pile group was also provided (Figure 12 and 13). Details of the test results and instrumentation are described in Appendix E of Brown et al. (2001) and Chakraborty (2000).

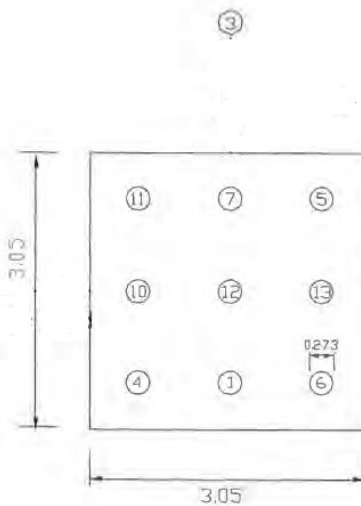


Figure 9. Numbering of the 9-pile group (Brown et al. 2001).



Figure 10. Photo of 9-pile group looking from west to east taken in March 2018.

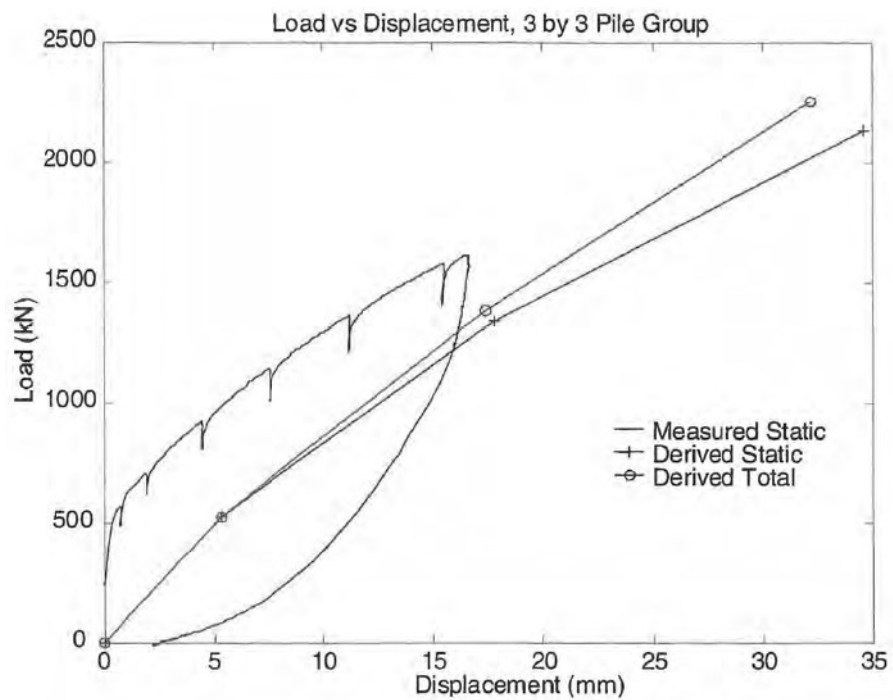


Figure 11. Load vs. Displacement for 9-pile group (Brown et al. 2001).

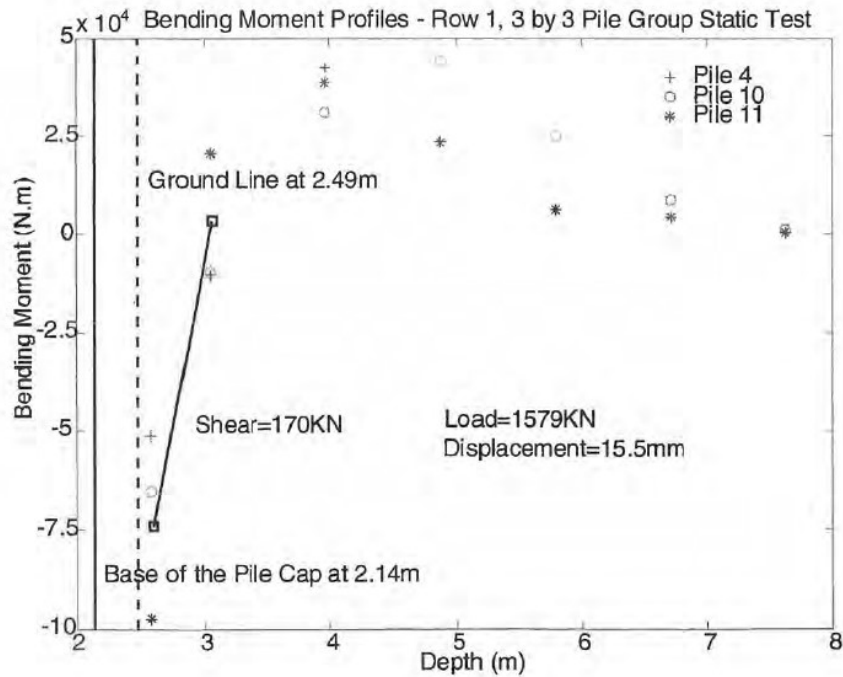


Figure 12. Bending moment profiles for pile 4, 10, 11 of 9-pile Group (Brown et al. 2001).

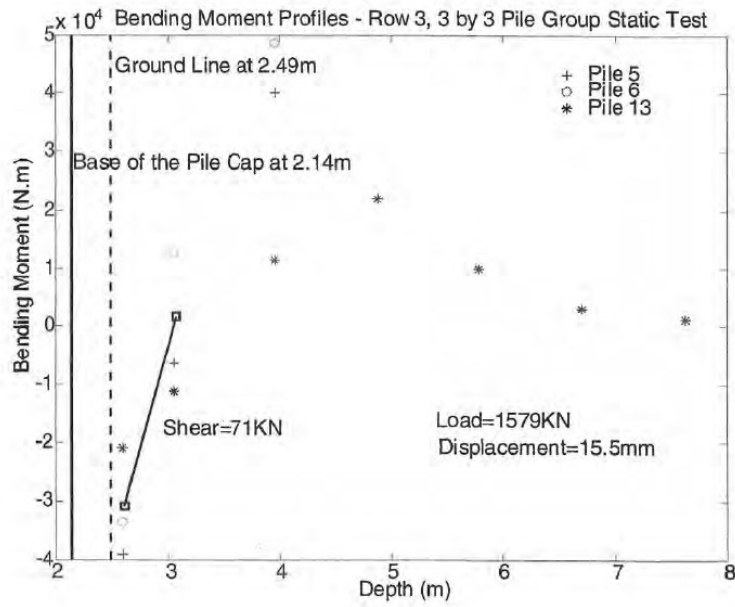
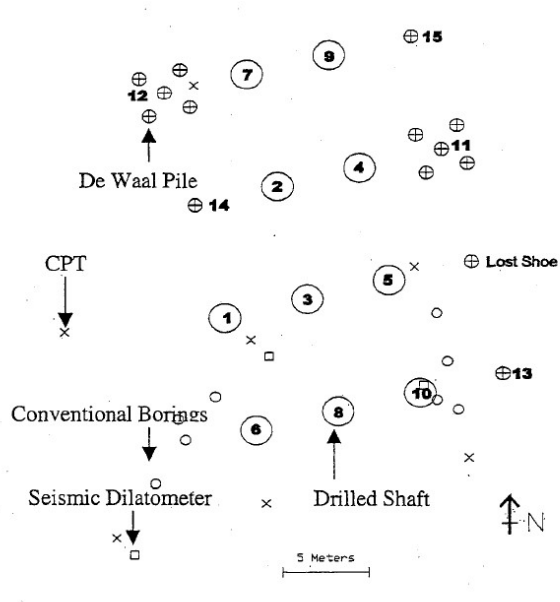


Figure 13. Bending moment profiles for pile 5, 6, 13 of 9-pile Group (Brown et al. 2001).

2.4.2 Drilled Shafts

Brown (2002) describes the installation of the ten drilled shafts currently installed at the Spring Villa test site (Figure 14). The shafts were all 0.9 m (3 feet) in diameter and 11 m deep (36 feet) and were constructed using either a casing advanced ahead of the hole or with drilling slurry (polymer or bentonite). The locations and identification (ID) numbers of the shafts are shown in Figure 14. Recent photos of these drilled shafts are shown in Figures 15 and 16. In Figure 15, the closest row of shafts from left to right is number 6, 8 and 10. The middle row of shafts from left to right is number 1, 3 and 5 and the furthest row of shafts (close to the equipment shed) is number 2 and 4 from left to right. In Figure 16, the closest row of shafts from left to right is 9 and 7. The other shafts can be seen in the background.

Details for each shaft are listed in Table 4 along with the shaft names used by Brown (2002). There were two drilled shafts (shaft number 3 and 10) constructed by using bentonite slurry, four shafts (shaft number 1, 5, 6 and 8) were constructed using polymer slurry, and four shafts (shaft numbers 2, 4, 7 and 9) were constructed using temporary casing advanced ahead of the shaft excavation. Defects were placed in shafts 4 and 9. These defects consisted of sand bags tied to the rebar cage at a depth of 4 m for shaft 4 and a depth of 8 m for shaft 9. All of shafts were placed by using a concrete with 13 mm maximum size gravel aggregate, a slump of 175 to 226 mm, and a design compressive strength of 28 MPa.



Auburn University Geotechnical Research Site Layout

Figure 14. Layout of drilled shafts with other in-Situ test (Simpson and Brown 2003).



Figure 15. Photo of drilled shafts looking from south to north taken in March 2018.



Figure 16. Photo of drilled shafts looking from north to south taken in March 2018.

Table 4. Properties of the drilled shafts.

ID Number² (Figure 14)	Shaft Name¹	Construction Technique¹	Defect¹	Axial Load Test¹	Lateral Load Test²
1	24LP	Polymer Slurry		X	X
2	24C	Casing		X	X
3	24B	Bentonite Slurry		X	X
4	1CDef	Casing	X	X	
5	1LP	Polymer Slurry		X	X
6	24DP	Polymer Slurry		X	X
7	1C	Casing		X	
8	1DP	Polymer Slurry		X	
9	24CDef	Casing	X	X	
10	1B	Bentonite Slurry		X	

¹Brown (2002) ²Simpson and Brown (2003)

The shafts were axial load tested statically (Brown 2002) and select shafts (1, 2, 3, 4, 5 and 6) were lateral load tested, statically (Simpson and Brown 2003). The axial load tests were performed against a reaction frame, which was anchored using four CFA piles, and compared the effect of different drilling techniques. Brown (2002) mentioned that the bentonite slurry shafts had a lower capacity compared to the other construction techniques and the polymer slurry had an excellent bond between the concrete and soil.

The lateral load tests were performed in pairs by pushing the shafts together using a hydraulic jack on the outside of one of the shafts and tension bars between the two shafts. Movement of the shafts was monitored using both displacement transducers mounted to reference beams and inclinometers in the shafts. The inclinometer test was used to measure the deflection along the shaft during the test, and the Linear Variable Differential Transformers (LVDT) was used to measure the pile head deflections during the test.

Table 5 presents the lateral load that was applied to each tested shaft for LVDT measurements in Simpson and Brown (2003). Shaft 5 was loaded differently than other tested shafts, because it was necessary to have a higher load to fail the defective shaft. Then the inclinometer test was performed on these shafts (Simpson and Brown 2003). Table 6 shows the loading for each tested shaft for inclinometer measurement. The applied loads present in Table 6 were different than those used with LVDT measurements, and the required testing time was also longer (Simpson and Brown 2003).

Table 5. Applied load for LVDT measurement of tested shafts (Simpson and Brown 2003).

Shaft Number	Load (kN)
1, 2, 3, 6	87, 174, 261, 348, 435, 522, 609, 695, 782
5	162, 334, 506, 589, 67, 757, 870, 924

Table 6. Applied load for inclinometer measurement of tested shafts (Simpson and Brown 2003).

Shaft Number	Load (kN)
1, 6	174, 348, 522, 695
2, 3	348, 435, 522, 609, 695, 782
5	162, 334, 506, 589, 670, 757, 870, 924

Data collection during the LVDT testing was taken to determine the pile head deflections when the pile came to a constant displacement.

The inclinometer tests measured the displacement in the shaft with depth. The data was collected every 0.5 meter below the ground surface. The strains in the shaft were also monitored to determine the depth at which the maximum bending moment occurred. The lateral deflection plots for each of the loading stages were presented in Simpson and Brown (2003). The results presented that the maximum bending moment occurs at the top 1/3 of the shaft, and the strain decreased as the depth increased (Simpson and Brown 2003). Figure 17 presents the one of the results of the inclinometer tests in Simpson and Brown (2003).

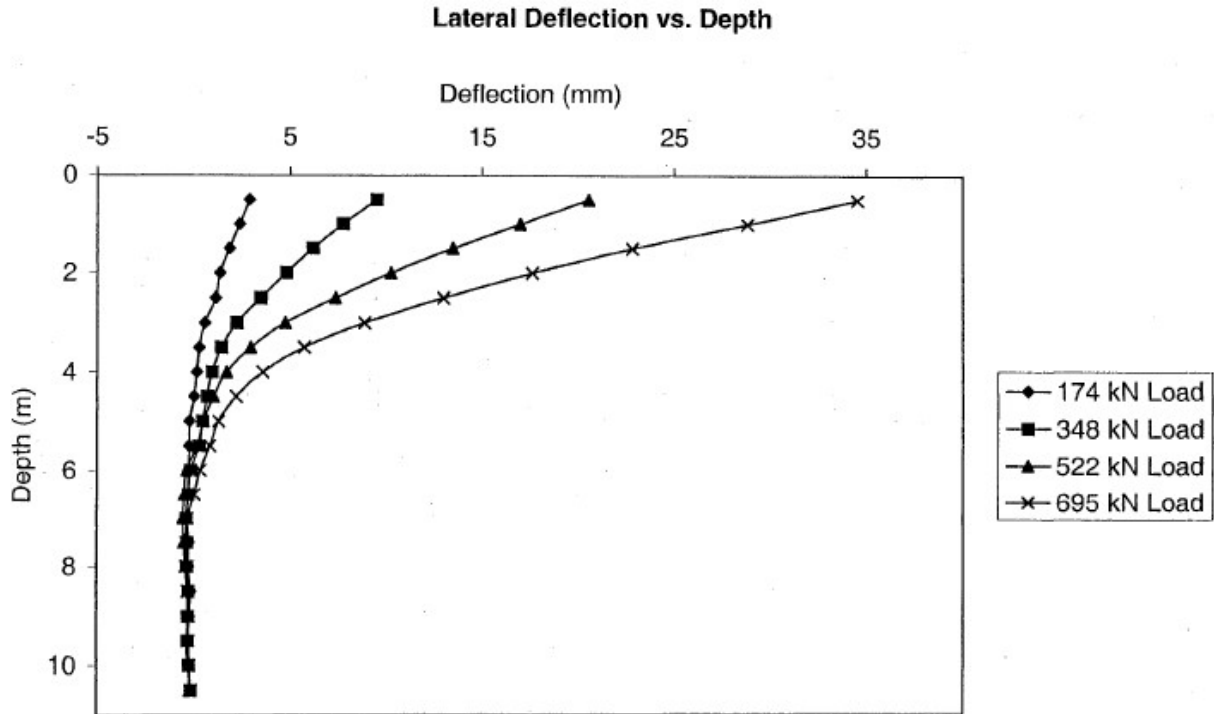


Figure 17. Lateral deflection vs Depth from inclinometer tests for shaft 1 (Simpson and Brown 2003).

2.4.3 H-Pile Bents

Marshall et al. (2017) described the installation and testing of two H-pile bents at the Spring Villa test site. Each bent consists of a reinforced concrete cap and four 35 feet long steel H-piles. The piles were installed using a vibratory hammer and each is embedded at least 20 feet in the ground. The north bent has four vertical piles; the south bent has two vertical piles, but the outer two piles were battered with a 1.5/12 slope. Two load tests were performed for each bent with both bents being laterally loaded using the 9-pile group as a reaction. The first lateral load test was used to ensure the hydraulic jacks and loading apparatus was functioning properly. The movement of the piles in the bents was monitored using inclinometers and the forces in each pile were computed using strain gauges. No measurements were taken of the response of the 9-pile group. The second

lateral test was performed until observable failure occurred on each bent.

Figure 18 shows the battered pile group and the piles were numbered Pile 1, Pile 2, Pile 3 and Pile 4 from east to west. At a lateral load of 100 kips, flexure cracking of the cap occurred above pile 2 and the crack grew in the direction of pile 1. The cracking widened when the load was increased. At 140 kips, the maximum cracks were observed (Marshall et al. 2017).



Figure 18. Battered bent, taken from north to south (Marshall et al. 2017).

The vertical pile bent was numbered Pile 5, Pile 6, Pile 7 and Pile 8 from south to north. Figure 19 shows the picture of vertical bent. Similar to the battered bent, the maximum applied load was 140 kips. The piles were yielding in the pile flanges at this load. The deflection of the bent cap increased nonlinearly when the yielding occurred. The cracking of the soil around the piles also occurred during this load test. The bending moments, axial forces and lateral deflections of the piles at different depths were calculated and are shown along with the load deflection behavior of each bent in Marshall et al. (2017).



Figure 19. Vertical bent, taken from south to north (Marshall et al. 2017).

CHAPTER 3: DESCRIPTION OF THE GIS DATABASE

3.1 Location Survey at Spring Villa Test Site

Development of the GIS database required obtaining the coordinates for each drilled shaft, pipe piles, H-piles, and pile groups at the Spring Villa test site. This was accomplished through surveys using the Topcon GR-3™ GPS receiver. The Topcon GR-3 GPS receiver was developed by Topcon Positioning Systems, Inc. (TPS). Figure 20 depicts the GP-3 GPS receiver, Topcon FC-200 and operator's manual.



Figure 20. GR-3™ GPS receiver, Topcon FC-200 and operator's manual for survey (Topcon Positioning Systems, Inc.).

After obtaining the coordinates of each of the foundations, the surveyed results were summarized into an Excel spreadsheet and compared with existing maps. Table 7 presents the surveyed coordinates for each foundation. The naming convention for the foundations is as follows: “DS” is used for drilled shafts; “MP” is used for single pipe piles; “PG” is used to designate the pile or CFA pile groups; “H” is used for single H-piles; and “HG” is used for the H-pile group.

Table 7. Surveyed coordinates from the Spring Villa test site

Description	Latitude (Degree)	Longitude (Degree)
Drilled Shaft 10	32.353833	-85.174976
Drilled Shaft 8	32.353828	-85.174993
Drilled Shaft 6	32.353823	-85.175009
Drilled Shaft 1	32.353845	-85.175018
Drilled Shaft 3	32.353840	-85.175002
Drilled Shaft 5	32.353856	-85.174983
Drilled Shaft 4	32.353878	-85.174991
Drilled Shaft 2	32.353874	-85.175010
Drilled Shaft 9	32.353899	-85.174999
Drilled Shaft 7	32.353897	-85.175010
Pipe Pile 1	32.353857	-85.174993
Pipe Pile 2	32.353877	-85.175001
Pipe Pile 3	32.353894	-85.175011
Pipe Pile 4	32.353922	-85.175027
Pipe Pile Group	32.353924	-85.175041
CFA Pile Group	32.353898	-85.175034
H Pile 1	32.353892	-85.175062
H Pile 2	32.353884	-85.175084
H-Pile Bent (Vertical)	32.353906	-85.175101
H-Pile Bent (Battered)	32.353940	-85.175103

3.2 Convert Coordinates into GIS Database

After verifying the locations of the foundations, a separate geospatial dataset was created for each of the different foundation types. For example, the drilled shafts were separated into one dataset, while the pipe piles were placed in another. The coordinate system of these input

coordinates was WGS 1984. The datasets were then converted in a geodatabase in order to allow attachment of raster data to the attribute table. This change allowed for important figures to be associated with each foundation.

3.3 Description of Attribute Table for Foundation Layers

The various geodatabase files were combined into a single GIS database using ArcMap (ESRI 2015) to provide a single resource for future researchers to find locations and information on each of the foundations and in-situ tests performed at the Spring Villa NGES. The following section provides descriptions of each of the foundation layers included in the database. This should serve as guide to future researchers attempting to navigate the data.

3.3.1 Drilled Shafts

Locations of foundations were stored in several layers in the database, and each layer has its unique attribute table. The drilled shaft layer has latitude, longitude and elevation columns that are surveyed from the Spring Villa test site. The elevations were taken from the GPS survey and so should be viewed with caution due to the potential inaccuracies when evaluating elevations using GPS. There are ten drilled shafts located at the test site. The “diameter_inch” and “length_ft” columns provide the design diameter of each, which are 36 inches and 36 ft, respectively, for the drilled shaft. The “TestResults” column presents the figure from Simpson and Brown (2003), which is one of the result of lateral load test load-deflection data. Because the attribute table can only have one raster data column, the other figures are not able to input in this attribute table. Figure 21 displays the information from above and Figure 22 presents the figure that is discussed in the “TestResult” column, which is the lateral load versus the deflection of the shafts.

OBJECTID *	SHAPE *	Latitude	Longitude	Elevation	Desc_	TestResults	Diameter_inch	Length_ft
1	Point	32.59402	-85.29728	625.122	1	<Raster>	36	36
2	Point	32.5941	-85.29726	627.05	2	<Raster>	36	36
3	Point	32.59403	-85.29723	627.046	3	<Raster>	36	36
4	Point	32.59411	-85.2972	631.726	4		36	36
5	Point	32.59405	-85.29718	626.106	5	<Raster>	36	36
6	Point	32.59396	-85.29726	622.498	6	<Raster>	36	36
7	Point	32.59417	-85.29726	650.798	7		36	36
8	Point	32.59398	-85.29721	623.556	8		36	36
9	Point	32.59417	-85.29723	634.356	9		36	36
10	Point	32.59399	-85.29716	623.928	10		36	36

Figure 21. The first segment of the attribute table for the drilled shaft layer.

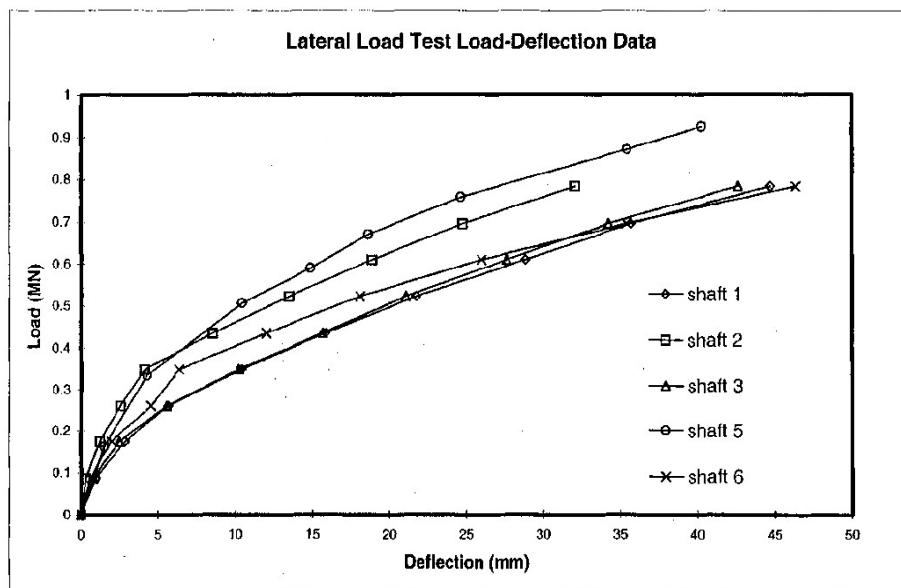


Figure 22. Load vs Deflection from LVDT data (Simpson and Brown 2003).

The “concrete modulus” and “concrete strength” columns provide the design concrete modulus, which is 4400 ksi and has a concrete strength, which is 4500 psi for the drilled shafts. The “loads applied for LVDT measurement” and “loads applied for inclinometer measurements” columns are provided by Simpson and Brown (2003), which provides the tested loads of the LVDT measurement and inclinometer measurement. The unit of these forces is kilonewton (KN). This

portion of the attribute table is shown in Figure 23.

The “Reference” column provides the reference name which matches the references provide in this thesis. The “Type of Shafts” column provides a description of the shaft construction including whether the shaft is defective or not. The “MixDesign” and “ConcreteBreaks” columns provide whether the information of concrete mix design is available or not and whether the concrete breaks information is available or not. These information could be found online with the database. The mix design described the concrete components and the percentage of each portion. The concrete breaks described the shaft strength and what type of failure it had. The “Construction technique” provides the construction technique also.

Concrete_modulus_ksi	Concrete_strength_psi	Loads Applied for LVDT Measurements	Loads Applied for Inclinometer Measurements
4400	4500	87,174,261,348,435,522,609,695,782	174,348,522,695
4400	4500	87,174,261,348,435,522,609,695,782	348,435,522,609,695,782
4400	4500	87,174,261,348,435,522,609,695,782	348,435,522,609,695,782
<Null>	<Null>	<Null>	<Null>
4400	4500	162,334,506,589,67,757,870,924	162,334,506,589,670,757,870,924
4400	4500	87,174,261,348,435,522,609,695,782	174,348,522,695
<Null>	<Null>	<Null>	<Null>
<Null>	<Null>	<Null>	<Null>
<Null>	<Null>	<Null>	<Null>
<Null>	<Null>	<Null>	<Null>

Figure 23. The second segment of the attribute table for the drilled shaft layer.

Loads Applied for Inclinometer Measurements	Reference	Type of Shafts	MixDesign	ConcreteBreaks	Construction Technique
174,348,522,695	Development_of_P-Y_Curves_for_Piedmont_Residual_Soils_Simpson_and_Brown_2003	24_Liquid_Polymer	Yes	Yes	1_Polymer Slurry
348,435,522,609,695,782	Development_of_P-Y_Curves_for_Piedmont_Residual_Soils_Simpson_and_Brown_2003	24_Cased	Yes	Yes	2_Casing
348,435,522,609,695,782	Development_of_P-Y_Curves_for_Piedmont_Residual_Soils_Simpson_and_Brown_2003	24_Bentonite	Yes	Yes	3_Bentonite Slurry
<Null>	<Null>	1_Cased_with_Soil_Inclusion_Defect	Yes	Yes	4_Casing
162,334,506,589,670,757,870,924	Development_of_P-Y_Curves_for_Piedmont_Residual_Soils_Simpson_and_Brown_2003	1_Liquid_Polymer	Yes	Yes	5_Polymer Slurry
174,348,522,695	Development_of_P-Y_Curves_for_Piedmont_Residual_Soils_Simpson_and_Brown_2003	24_Dry_Polymer	Yes	Yes	6_Polymer Slurry
<Null>	<Null>	1_Cased	Yes	Yes	7_Casing
<Null>	<Null>	1_Dry_Polymer	Yes	Yes	8_Polymer Slurry
<Null>	<Null>	24_Cased_with_Soil_Inclusion_Defec	Yes	Yes	9_Casing
<Null>	<Null>	1_Bentonite	Yes	Yes	10_Bentonite Slurry

Figure 24. The third and final segment of the attribute table for the drilled shaft layer.

3.3.2 Pile Groups

The “PileGroup” layer presents the information of two pile groups that are currently in place at the Spring Villa test site. The attribute table contains the “elevation”, “longitude” and “latitude” columns that were surveyed at the Spring Villa test site. These points were taken on the four corners of the pile cap and do not relate to individual piles. The “GroupType” column indicates whether the group was constructed using continuous flight auger (CFA) piles or the NCHRP pipe piles. The “Reference” column shows the reference of two pile groups — Brown et al. (2001) and Brown and Drew (2000). The “Pile_No” column links to a raster image that shows the configuration of the pile group. Information on the capacity and load test results were difficult to summarize into a single value and so can be found in the respective references.

OBJECTID *	SHAPE *	Pile_No	GroupType	Latitude	Longitude	Elevation_m	Reference
1	Point	<Raster	Pipe Pile Group	32.594241	-85.297341	628.318	Axial Capacity of Augered Displacement Piles at Auburn University
2	Point	<Raster	Pipe Pile Group	32.594208	-85.297329	631.632	Axial Capacity of Augered Displacement Piles at Auburn University
3	Point	<Raster	Pipe Pile Group	32.594207	-85.297365	624.091	Axial Capacity of Augered Displacement Piles at Auburn University
4	Point	<Raster	Pipe Pile Group	32.594225	-85.297369	629.446	Axial Capacity of Augered Displacement Piles at Auburn University
5	Point	<Raster	CFA Pile Group	32.594168	-85.297324	625.276	Static and Dynamic Lateral Loading of Pile Groups
6	Point	<Raster	CFA Pile Group	32.594142	-85.297312	621.162	Static and Dynamic Lateral Loading of Pile Groups
7	Point	<Raster	CFA Pile Group	32.594136	-85.297935	628.374	Static and Dynamic Lateral Loading of Pile Groups
8	Point	<Raster	CFA Pile Group	32.594162	-85.297349	624.081	Static and Dynamic Lateral Loading of Pile Groups

Figure 25. The attribute table of the pile group layer.

3.3.3 H-Pile Groups

The “Twobents” layer contains information on the two H-pile bents located at the Spring Villa test site. Each bent has two points which represent the two edges of the bent along the longest direction. These points do not represent individual piles. In the attribute table, the “PileType” column presents the pile information of these two bents, and there are four HP 12 x 53 piles, being 35 feet long for each bent (Marshall et al. 2017). The “EmbedmentLength” column represents the embedment length of these piles, which is at least 20 ft. The “LengthAboveGround” column

presents the clear pile length above the ground of each bent. The battered bent has 9 ft clear pile length and the vertical bent has 10 ft clear pile length. The “BatteredSlope” column shows the battered slope of the battered bent, which is 1.5/12. The caps for each bent are the same, which is 3’ x 3’ by 28’ long. The “CapDimension” column presents this information. Figure 26 shows this part of the table.

SHAPE *	ExampleResult	PileType	EmbedmentLength	LengthAboveGround	Battered Slope	CapDimension
Point	<Raster>	4 HP12x53 piles 35 feet long	at least 20 ft	9 ft clear pile length	1.5/12	3'x3' by 28' long
Point	<Raster>	4 HP12x53 piles 35 feet long	at least 20 ft	9 ft clear pile length	1.5/12	3'x3' by 28' long
Point	<Raster>	4 HP12x53 piles 35 feet long	at least 20 ft	10 ft clear pile length	<Null>	3'x3' by 28' long
Point	<Raster>	4 HP12x53 piles 35 feet long	at least 20 ft	10 ft clear pile length	<Null>	3'x3' by 28' long

Figure 26. The first segment of the attribute table for the two bents layer.

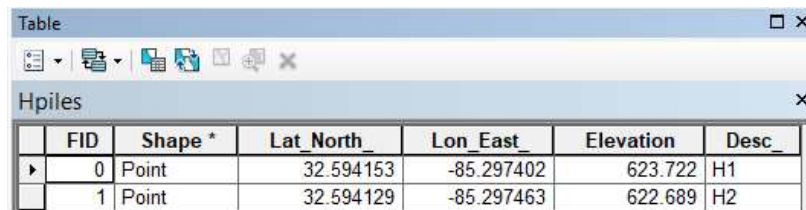
The “ConcreteMixDesign” column presents the design strength in the bent caps, which was a 3000 psi mix design. The “PileNumber” column displays the pile number that presents in the paper— the pile numbers of the battered bent are 1, 2, 3 and 4. The pile numbers of the vertical bent are 5, 6, 7 and 8. All the tested bents failed and the pile yield stress was 58 ksi, This information presents in the “Failure” and “PileYieldStress_ksi” columns. The other columns are “Latitude”, “Longitude”, “Elevation” and “Desc”, which present the surveyed information and the description of these bents. Figure 27 shows the rest of the attribute table of the two bents layer.

ConcreteMixDesign	PileNumber	Failure	PileYieldStress_ksi	Latitude	Longitude	Elevation	Desc_
3000	Pile 1,2,3,4	Yes	58	32.594191	-85.297508	620.265	HG1,Battered
3000	Pile 1,2,3,4	Yes	58	32.594214	-85.297423	613.89	HG2,Battered
3000	Pile 5,6,7,8	Yes	58	32.594285	-85.297514	631.235	HG3,Vertical
3000	Pile 5,6,7,8	Yes	58	32.59426	-85.297422	620.16	HG4,Vertical

Figure 27. The final segment of the attribute table for the two bents layer.

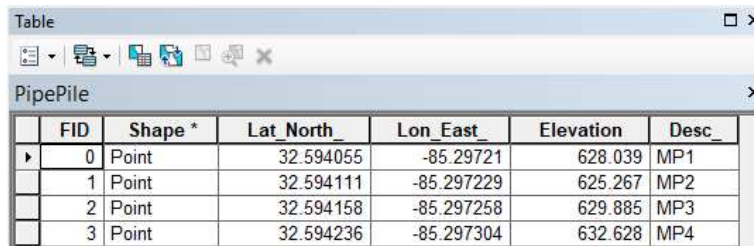
3.3.4 Other Foundations

In addition to those foundations discussed above, two individual H-piles and 3 individual pipe piles are currently installed at the site. These foundations do not appear to have been load tested and the author is not aware of any driving records or publications which describe the installation of these foundations. The pipe piles were left over after the removal of the first 12-pile group installed by Brown et al. (2001). The origin of the H-piles is currently unknown. Figure 28 and Figure 29 present the attribute table for H piles and pipe piles respectively. They only have the survey data in the attribute table as no other information is available.



FID	Shape *	Lat_North_	Lon_East_	Elevation	Desc_
0	Point	32.594153	-85.297402	623.722	H1
1	Point	32.594129	-85.297463	622.689	H2

Figure 28. The attribute table of H pile layer.



FID	Shape *	Lat_North_	Lon_East_	Elevation	Desc_
0	Point	32.594055	-85.29721	628.039	MP1
1	Point	32.594111	-85.297229	625.267	MP2
2	Point	32.594158	-85.297258	629.885	MP3
3	Point	32.594236	-85.297304	632.628	MP4

Figure 29. The attribute table of pipe pile layer.

3.4 In-Situ Test Layers and their Attribute Tables in the GIS Database

Locations for the in-situ tests were either digitized from maps provided in the original references such as Vinson and Brown (1997), or were provided as latitude and longitude by the original study authors. One of the challenges was finding maps which included common reference points such as CPT soundings or drilled shafts. The primary maps used for the current database

were shown in Figure 5 and Figure 14 in Chapter 2. Data points which could not be accurately located using one of these methods were excluded from the database.

The in-situ tests were also grouped by type and input as separate layers in the database to allow for different types of information to be stored about each. Other types of data such as shear wave velocity profiles were attached to the points using images stored as raster data files. Links to the original reports and raw data (where available) were included for each point, so future researchers can quickly locate information not included explicitly in the database.

For the crosshole seismic testing layer, the “Test Results” column provides a picture of the shear wave velocity. The apparent shear wave velocity for array 1 and array 2 and apparent compression wave velocity for array 1 and array 2 are presented in that picture. The “description” column is used to describe the borehole number that were used for the test, which was from B-1 to B-6. The “average shear wave velocity” represents a range of shear wave velocity for each borehole, the average shear wave velocity was between 200 m/s and 250 m/s. The “reference” column gives the full name of the reference paper and the “link” column displays the link to the paper. Because these points were located by the maps that presented in the reference paper, the coordinates and elevation were blank. Figure 30 and Figure 31 present the attribute table of this layer.

OBJECTID *	SHAPE *	TestResults	Latitude	Longitude	Elevation	Error	Category
1	Point	<Raster>	<Null>	<Null>	<Null>	<Null>	Crosshole_Seismic_Testing
2	Point	<Raster>	<Null>	<Null>	<Null>	<Null>	Crosshole_Seismic_Testing
3	Point	<Raster>	<Null>	<Null>	<Null>	<Null>	Crosshole_Seismic_Testing
4	Point	<Raster>	<Null>	<Null>	<Null>	<Null>	Crosshole_Seismic_Testing
5	Point	<Raster>	<Null>	<Null>	<Null>	<Null>	Crosshole_Seismic_Testing
6	Point	<Raster>	<Null>	<Null>	<Null>	<Null>	Crosshole_Seismic_Testing

Figure 30. The first segment of the attribute table for the crosshole seismic testing layer.

Desc	ArrayNo	Average Shear Wave Velocity	Reference	Link
B-1	1	Between 200 and 250 m/s	Site Characterization of the Spring	http://eng.auburn.edu/files/cen
B-2	1	Between 200 and 250 m/s	Site Characterization of the Spring	http://eng.auburn.edu/files/cen
B-3	1	Between 200 and 250 m/s	Site Characterization of the Spring	http://eng.auburn.edu/files/cen
B-4	2	Between 200 and 250 m/s	Site Characterization of the Spring	http://eng.auburn.edu/files/cen
B-5	2	Between 200 and 250 m/s	Site Characterization of the Spring	http://eng.auburn.edu/files/cen
B-6	2	Between 200 and 250 m/s	Site Characterization of the Spring	http://eng.auburn.edu/files/cen

Figure 31. The second segment of the attribute table for the crosshole seismic testing layer.

The coordinates of the Georgia Tech CPTs were provided by the original authors (Georgia Tech 2000). Several of these tests were seismic CPTs. Georgia Tech researchers performed additional CPTs at the Spring Villa NGES in 2016 which will be added to the database when they are published. The “longitude” and “latitude” columns display the location of the borings. The “results” column shows the CPT test results using a raster file. These results are shown in Figures 32 through 35 (Georgia Tech 2000).

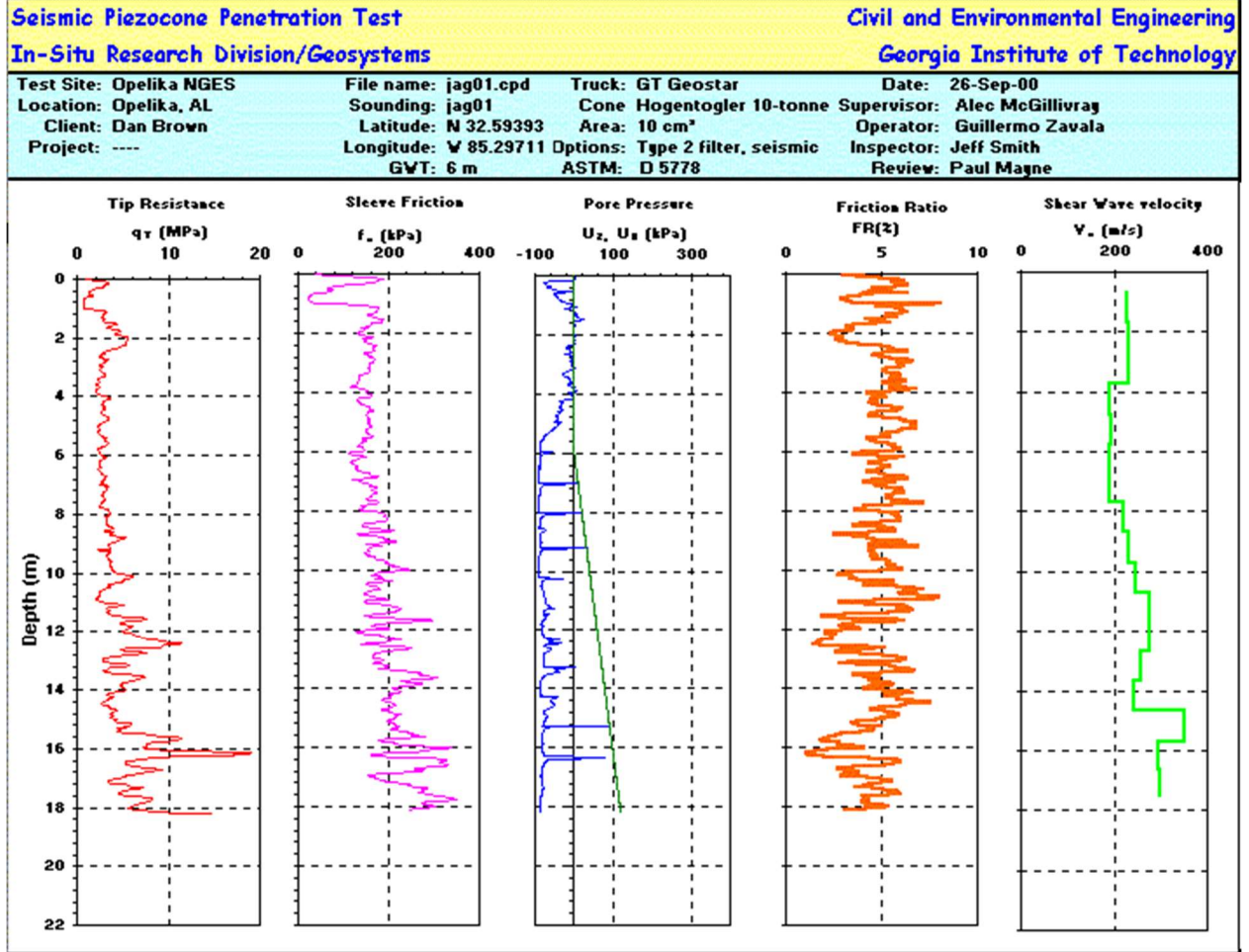


Figure 32. The result of sounding jag01 (Georgia Tech 2000).

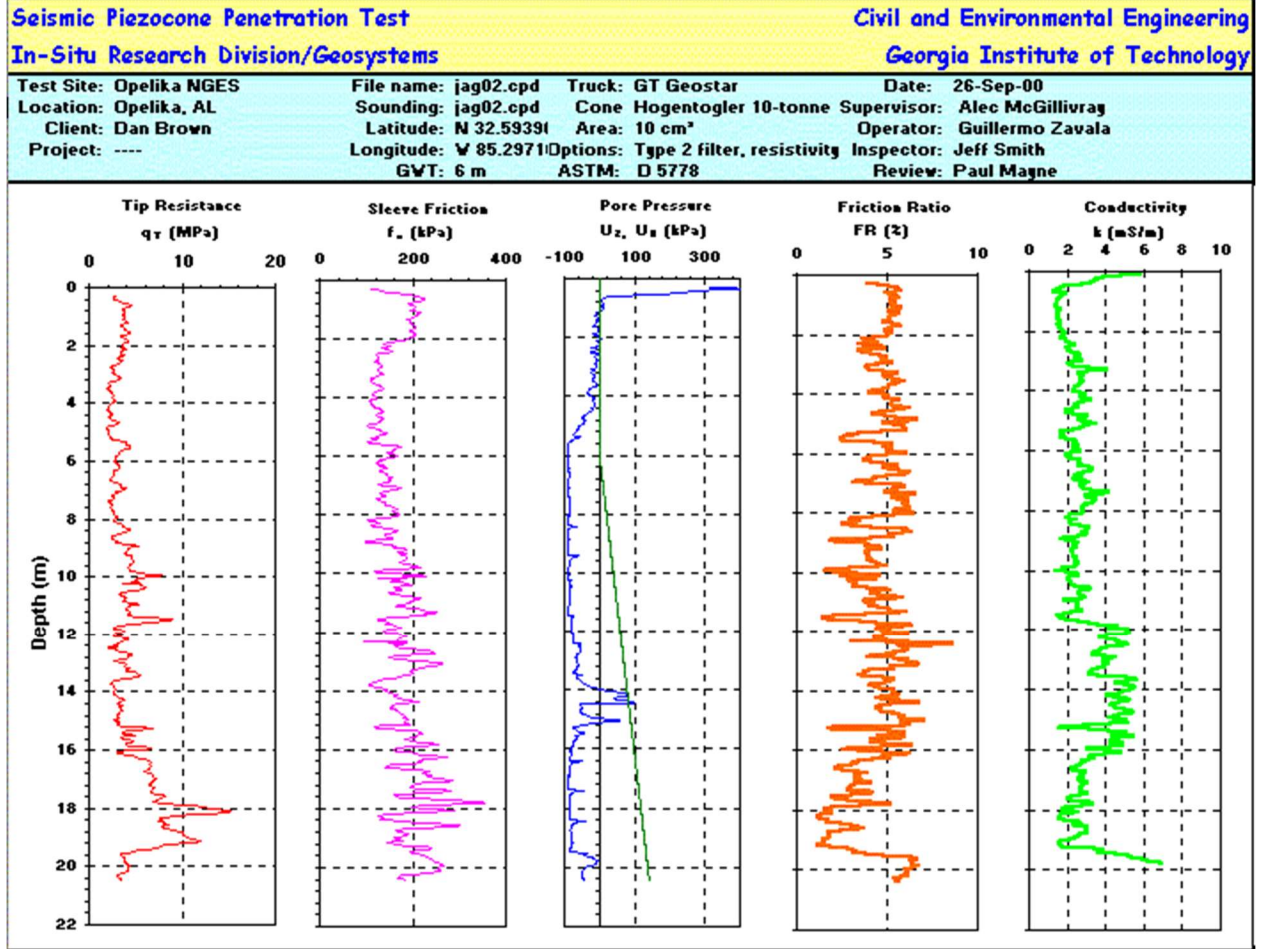


Figure 33. The result of sounding jag02 (Georgia Tech 2000).

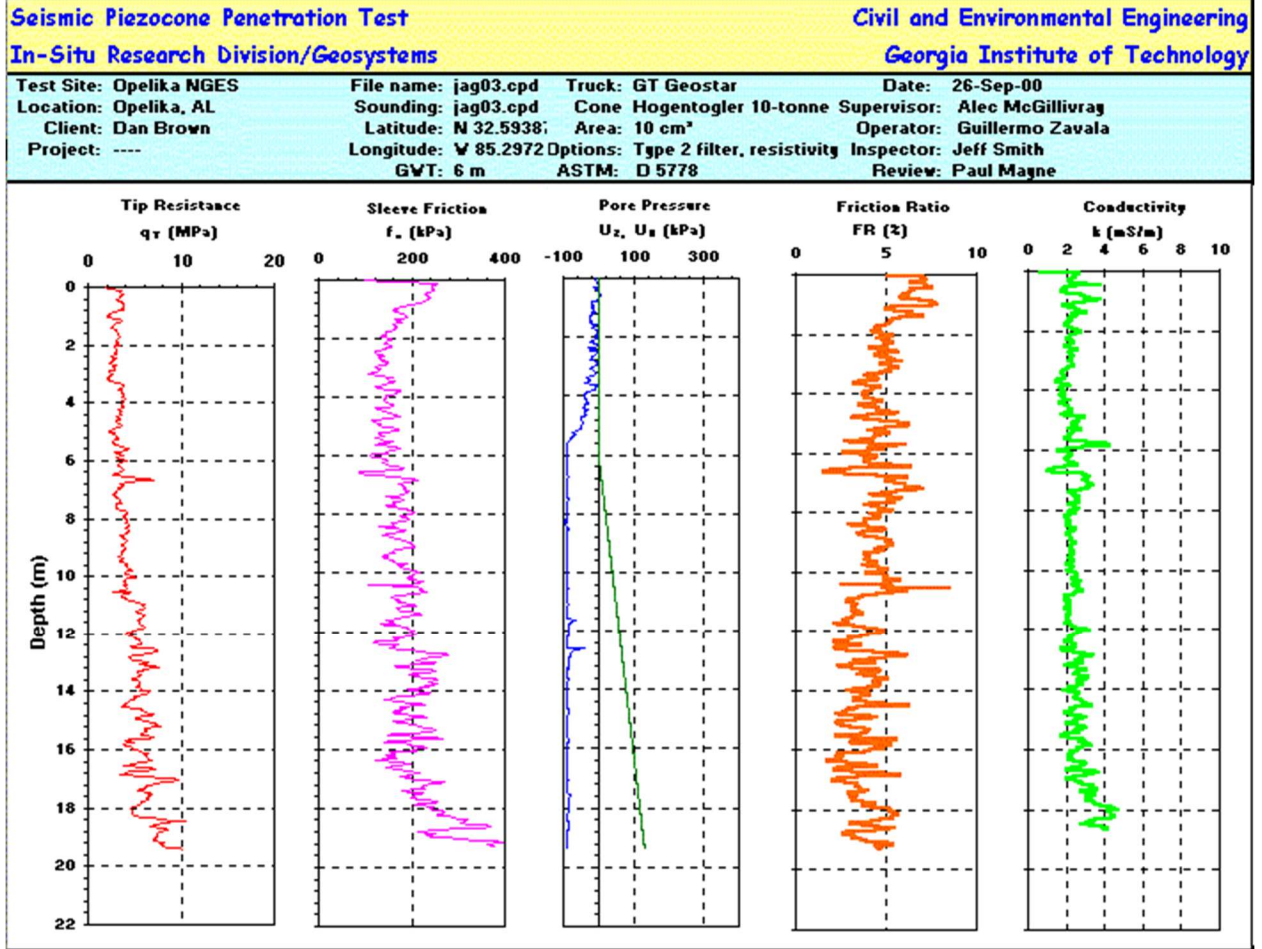


Figure 34. The result of sounding jag03 (Georgia Tech 2000).

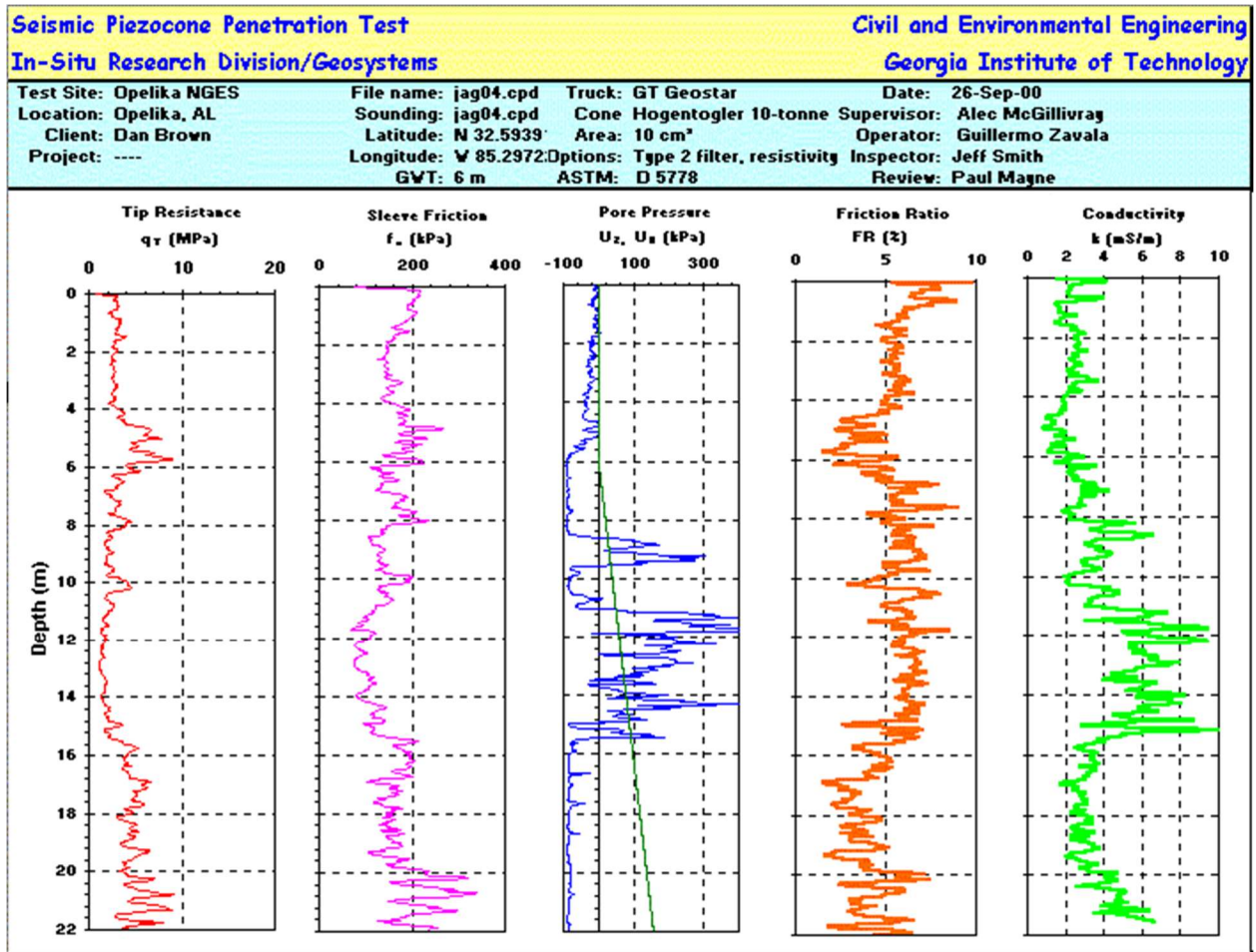


Figure 35. The result of sounding jag04 (Georgia Tech 2000).

The “description” column reveals the number of each different sounding. The “GWT” column presents the ground water table of each soundings, which is 6 meters below the ground surface. The “truck”, “cone”, “Area”, “options”, “date” and “ASTM” columns briefly describe the test method and the equipment used. The attribute table is shown in Figure 36 and 37.

OBJECTID *	SHAPE *	Latitude	Longitude	Results	Desc_	GWT_meter	Truck	Cone
1	Point	32.59393	-85.29711	<Raster> >	jag01	6	GT_Geostar	Hogentogler_10-tonne
2	Point	32.5939	-85.29716	<Raster>	jag02	6	GT_Geostar	Hogentogler_10-tonne
3	Point	32.59387	-85.29721	<Raster>	jag03	6	GT_Geostar	Hogentogler_10-tonne
4	Point	32.59391	-85.29722	<Raster>	jag04	6	GT_Geostar	Hogentogler_10-tonne

Figure 36. The first segment of the attribute table for the Georgia Tech CPTs.

Desc_	GWT_meter	Truck	Cone	Area_cm2	Options	ASTM	Date
jag01	6	GT_Geostar	Hogentogler_10-tonne	10	Type_2_filter_seismic	D5778	26_Sep_00
jag02	6	GT_Geostar	Hogentogler_10-tonne	10	Type_2_filter_resistivity	D5778	26_Sep_00
jag03	6	GT_Geostar	Hogentogler_10-tonne	10	Type_2_filter_resistivity	D5778	26_Sep_00
jag04	6	GT_Geostar	Hogentogler_10-tonne	10	Type_2_filter_resistivity	D5778	26_Sep_00

Figure 37. The final segment of the attribute table for the Georgia Tech CPTs.

Two types of PMT tests were performed at the site, Cone PMT and Menard PMT, which are both include in the PMT layer. The “test results” column contains a raster image of the test results. The “Description” and “Category” columns display the borehole number of the tests and the pressuremeter test category for each borehole. Figure 38 presents the portion of the attribute table containing this information.

OBJECTID *	SHAPE *	TestResults	Latitude	Longitude	Elevation	Error	Category	Desc_
1	Point	<Raster>	<Null>	<Null>	<Null>	<Null>	Menard_PMT	B-2
2	Point	<Raster>	<Null>	<Null>	<Null>	<Null>	Menard_PMT	B-5
3	Point	<Raster>	<Null>	<Null>	<Null>	<Null>	Cone PMT	C-41
4	Point	<Raster>	<Null>	<Null>	<Null>	<Null>	Cone PMT	C-42
5	Point	<Raster>	<Null>	<Null>	<Null>	<Null>	Cone PMT	C-43
6	Point	<Raster>	<Null>	<Null>	<Null>	<Null>	Cone PMT	C-44

Figure 38. The first segment of the attribute table for the PMT layer.

The columns labeled, “E kPa depth 1 m”, “E kPa depth 2 m”, “E kPa depth 4 m”, “E kPa depth 6 m”, “E kPa depth 8 m”, “E kPa depth 10 m”, “E kPa depth 12 m” and “E kPa depth 15 m” columns display the Young’s Modulus at each different depth for Menard PMT. The “reference” and “link” columns show the paper name and the link of this paper. Figure 39 and Figure 40 present the rest attribute table of this layer.

PMT						
E_kPa_Depth1m	E_kPa_Depth2m	E_kPa_Depth4m	E_kPa_Depth6m	E_kPa_Depth8m	E_kPa_Depth10m	E_kPa_Depth12m
6400	7700	2600	5500	5400	4900	6800
11100	9000	6100	6700	5000	7400	3500
<Null>	<Null>	<Null>	<Null>	<Null>	<Null>	<Null>
<Null>	<Null>	<Null>	<Null>	<Null>	<Null>	<Null>
<Null>	<Null>	<Null>	<Null>	<Null>	<Null>	<Null>
<Null>	<Null>	<Null>	<Null>	<Null>	<Null>	<Null>

Figure 39. The second segment of the attribute table of PMT layer.

PMT			
E_kPa_Depth15m	Maximum_Depth_m	Link	Reference
4600	15	http://eng.auburn.edu/files/centers/hrc	Site_Characterization_of_the_Spring_Villa_Geotechnical_Tes
7200	15	http://eng.auburn.edu/files/centers/hrc	Site_Characterization_of_the_Spring_Villa_Geotechnical_Tes
<Null>	<Null>	<Null>	<Null>
<Null>	<Null>	<Null>	<Null>
<Null>	<Null>	<Null>	<Null>
<Null>	<Null>	<Null>	<Null>

Figure 40. The third and final segment of the attribute table of PMT layer.

For the SPT layer, the “SPT results” column presents the uncorrected N values versus the depth in a raster image. The “description” and “category” columns display the borehole number and the category of the in-situ test. The “depth ft” column represents the maximum depth of these SPT tests, which is 50 feet. The “reference” and “link” column reveals the paper name and author name and the link of this paper. Figure 41 and Figure 42 present the attribute table for the SPT layer.

SPT_Results										
OBJECTID *	SHAPE *	SPTResults	Latitude	Longitude	Elevation	Error	Category	Desc_	Depth_ft	
1	Point	<Raster>	<Null>	<Null>	<Null>	<Null>	SPT	B-1	50	
2	Point	<Raster>	<Null>	<Null>	<Null>	<Null>	SPT	B-3	50	
3	Point	<Raster>	<Null>	<Null>	<Null>	<Null>	SPT	B-4	50	
4	Point	<Raster>	<Null>	<Null>	<Null>	<Null>	SPT	B-6	50	

Figure 41. The first segment of the attribute table for the SPT layer.

Depth_ft	Reference	Link
50	Site Characterization of the Spring Villa Geotechnical Test Site And A Co	http://eng.auburn.edu/files/centers/hrc/930-425-2.pdf
50	Site Characterization of the Spring Villa Geotechnical Test Site And A Co	http://eng.auburn.edu/files/centers/hrc/930-425-2.pdf
50	Site Characterization of the Spring Villa Geotechnical Test Site And A Co	http://eng.auburn.edu/files/centers/hrc/930-425-2.pdf
50	Site Characterization of the Spring Villa Geotechnical Test Site And A Co	http://eng.auburn.edu/files/centers/hrc/930-425-2.pdf

Figure 42. The final segment of the attribute table for the SPT layer.

The CPT layer has a similar attribute table to the SPT layer. The “test results” column presents the CPT results for these soundings as a raster file. The “description” column shows the CPT sounding number at the Spring Villa test site. Figure 43 displays the attribute table of the CPT layer and presents the information that discussed above.

OBJECTID *	SHAPE *	TestResults	Latitude	Longitude	Elevation	Error	Category	Desc_
1	Point	<Raster>	<Null>	<Null>	<Null>	<Null>	CPT	C-21
2	Point	<Raster>	<Null>	<Null>	<Null>	<Null>	CPT	C-25
3	Point	<Raster>	<Null>	<Null>	<Null>	<Null>	CPT	C-27
4	Point	<Raster>	<Null>	<Null>	<Null>	<Null>	CPT	C-41
5	Point	<Raster>	<Null>	<Null>	<Null>	<Null>	CPT	C-42
6	Point	<Raster>	<Null>	<Null>	<Null>	<Null>	CPT	C-43
7	Point		<Null>	<Null>	<Null>	<Null>	CPT	C-22
8	Point	<Raster>	<Null>	<Null>	<Null>	<Null>	CPT	C-28
9	Point		<Null>	<Null>	<Null>	<Null>	CPT	C-24
10	Point		<Null>	<Null>	<Null>	<Null>	CPT	C-18
11	Point	<Raster>	<Null>	<Null>	<Null>	<Null>	CPT	C-11
12	Point	<Raster>	<Null>	<Null>	<Null>	<Null>	CPT	C-44
13	Point	<Raster>	<Null>	<Null>	<Null>	<Null>	CPT	C-32
14	Point		<Null>	<Null>	<Null>	<Null>	CPT	C-26
15	Point	<Raster>	<Null>	<Null>	<Null>	<Null>	CPT	C-23
16	Point	<Raster>	<Null>	<Null>	<Null>	<Null>	CPT	C-17
17	Point		<Null>	<Null>	<Null>	<Null>	CPT	C-12
18	Point	<Raster>	<Null>	<Null>	<Null>	<Null>	CPT	C-14
19	Point		<Null>	<Null>	<Null>	<Null>	CPT	C-15
20	Point	<Raster>	<Null>	<Null>	<Null>	<Null>	CPT	C-13
21	Point		<Null>	<Null>	<Null>	<Null>	CPT	C-16

Figure 43. The first segment of the attribute table for the CPT layer.

The “max depth meter” column presents the maximum depth of the tests, which is 15 meters for C-13, C-21, C-25, C-27, C-28, C-32, C-41, C-42 and C-43 and varied for the other

CPTs. The “average q_c kPa”, “average f_s kPa” and “ R_f range” columns provide a qualitative description of the CPT results for some of the soundings. For some of the CPTs, no results were available in the papers reviewed for this thesis and so these columns are marked as “Null”. The “reference” and “link” column shows the paper name and the author name and the link to the website. The “Plot Results” column indicates whether a plot of the results of the soundings is available in the reference. Figure 44 and Figure 45 present the rest of the attribute table for the CPT layer.

Max_Depth_meters	Average_qc_kPa	Average_fs_kPa	Rf_Range
15	from_2000_to_4000	Fairly_constant_near_or_above_150	Decrease_from_8%_to_4%_between_1_and_15_meters
15	from_2000_to_4000	Fairly_constant_near_or_above_150	Decrease_from_8%_to_4%_between_1_and_15_meters
15	from_2000_to_4000	Fairly_constant_near_or_above_150	Decrease_from_8%_to_4%_between_1_and_15_meters
15	from_2000_to_4000	Fairly_constant_near_or_above_150	Decrease_from_8%_to_4%_between_1_and_15_meters
15	from_2000_to_4000	Fairly_constant_near_or_above_150	Decrease_from_8%_to_4%_between_1_and_15_meters
15	from_2000_to_4000	Fairly_constant_near_or_above_150	Decrease_from_8%_to_4%_between_1_and_15_meters
<Null>	<Null>	<Null>	<Null>
15	<Null>	<Null>	<Null>
<Null>	<Null>	<Null>	<Null>
<Null>	<Null>	<Null>	<Null>
16	<Null>	<Null>	<Null>
24	<Null>	<Null>	<Null>
15	<Null>	<Null>	<Null>
<Null>	<Null>	<Null>	<Null>
18	<Null>	<Null>	<Null>
11	<Null>	<Null>	<Null>
<Null>	<Null>	<Null>	<Null>
20	<Null>	<Null>	<Null>
<Null>	<Null>	<Null>	<Null>
15	<Null>	<Null>	<Null>
<Null>	<Null>	<Null>	<Null>

Figure 44. The second segment of the attribute table for the CPT layer.

	Reference	Link	PlotResults
	Site_Characterization_of_the_Spring_Villa_Geotechnical_Test_Site_An	http://eng.auburn.edu/files/centers/hrc/930-425-2.pdf	Yes
	Site_Characterization_of_the_Spring_Villa_Geotechnical_Test_Site_An	http://eng.auburn.edu/files/centers/hrc/930-425-2.pdf	Yes
	Site_Characterization_of_the_Spring_Villa_Geotechnical_Test_Site_An	http://eng.auburn.edu/files/centers/hrc/930-425-2.pdf	Yes
	Site_Characterization_of_the_Spring_Villa_Geotechnical_Test_Site_An	http://eng.auburn.edu/files/centers/hrc/930-425-2.pdf	No
	Site_Characterization_of_the_Spring_Villa_Geotechnical_Test_Site_An	http://eng.auburn.edu/files/centers/hrc/930-425-2.pdf	No
	Site_Characterization_of_the_Spring_Villa_Geotechnical_Test_Site_An	http://eng.auburn.edu/files/centers/hrc/930-425-2.pdf	Yes
	<Null>	<Null>	No
	<Null>	<Null>	Yes
	<Null>	<Null>	No
	<Null>	<Null>	No
	<Null>	<Null>	Yes
	<Null>	<Null>	Yes
	<Null>	<Null>	Yes
	<Null>	<Null>	Yes
	<Null>	<Null>	Yes
	<Null>	<Null>	No
	<Null>	<Null>	Yes
	<Null>	<Null>	Yes
	<Null>	<Null>	No
	<Null>	<Null>	Yes
	<Null>	<Null>	No

Figure 45. The third and final segment of the attribute table for the CPT layer.

For the seismic CPT layer, the attribute table presents the results of the seismic CPT tests in “Result” column as a raster file and the “description” column presents the surrounding numbers. These reference for these results is Vinson and Brown (1997). Figure 46 presents the attribute table for this layer.

	OBJECTID *	SHAPE *	Result	Latitude	Longitude	Desc_
	1	Point	<Raster	<Null>	<Null>	C41
	2	Point	<Raster	<Null>	<Null>	C42

Figure 46. The attribute table of seismic CPT layer.

For the borehole shear results layer (Figure 47), the “test results” column of the attribute table presents the results summary from Vinson and Brown (1997) as a raster file (Figure 48). The raster file includes the water table, number of points on envelope, the regression coefficient,

cohesion and friction angle. The “description” column briefly describe the boring number where the borehole shear test was performed.

OBJECTID *	SHAPE *	TestResults	Latitude	Longitude	Elevation	Error	Category	Desc_
1	Point	<Raster>	<Null>	<Null>	<Null>	<Null>	Borhole_Shear	B-7
2	Point	<Raster>	<Null>	<Null>	<Null>	<Null>	Borhole_Shear	B-8

Figure 47. The first segment of the attribute table for the borehole shear test layer.

Boring	Depth (m)	Water Table Depth (m)	No. of Points On Envelope	Regression Coefficient	Cohesion (kPa)	Friction Angle (deg)
B-8	2	3.7	5	0.9912	4	38
B-8	3	3.7	5	0.9991	0	22
B-8	4	3.7	4	0.9902	4	13
B-7	6	3.7	4	0.9988	3	27
B-8	7	3.7	5	0.9996	4	20
B-8	9	3.7	4	0.9542	7	14

Figure 48. Borehole shear test results from Vinson and Brown (1997).

The columns “cohesion kPa 2 m”, “cohesion kPa 3 m”, “cohesion kPa 4 m”, “cohesion kPa 6 m”, “cohesion kPa 7 m”, “cohesion kPa 9 m”, “friction angle 2m”, “friction angle 3m”, “friction angle 4m”, “friction angle 6m”, “friction angle 7m” and “friction angle 9m” present the cohesion and friction angle at specific depth for that borehole. The number under these columns are from Figure 48 (Vinson and Brown 1997). The “reference” and “link” columns present the author and paper name and the link to the paper. The rest of the attribute table is presented in Figures 49, 50 and 51.

Reference	Link	cohesion_KPa2m	cohesion_KPa3m	cohesion_KPa4m
Site_Characterization_of_the_Spring_Villa_Geote	http://eng.auburn.edu/files/ce	<Null>	<Null>	<Null>
Site_Characterization_of_the_Spring_Villa_Geote	http://eng.auburn.edu/files/ce	4	0	4

Figure 49. The second segment of the attribute table for the borehole shear test layer.

cohesion_KPa6m	cohesion_KPa7m	cohesion_KPa9m	frictionangle2m	frictionangle3m	frictionangle4m
3	<Null>	<Null>	<Null>	<Null>	<Null>
<Null>	4	7	38	22	13

Figure 50. The third segment of the attribute table for the borehole shear test layer.

frictionangle3m	frictionangle4m	frictionangle6m	frictionangle7m	frictionangle9m
<Null>	<Null>	27	<Null>	<Null>
22	13	<Null>	20	14

Figure 51. The fourth and final segment of the attribute table for the borehole shear test layer.

For the dilatometer test layer, the attribute table is simpler compared to other layers. The columns it has are “result” and “description” column. The “result” column presents the Young’s modulus that derived from DMT, shear modulus from DMT, correlations of K_o with DMT and effective friction angle calculated by DMT (Figure 52). The “description” column gives the locations name at the site. Figure 53 shows the attribute table of DMT layer.

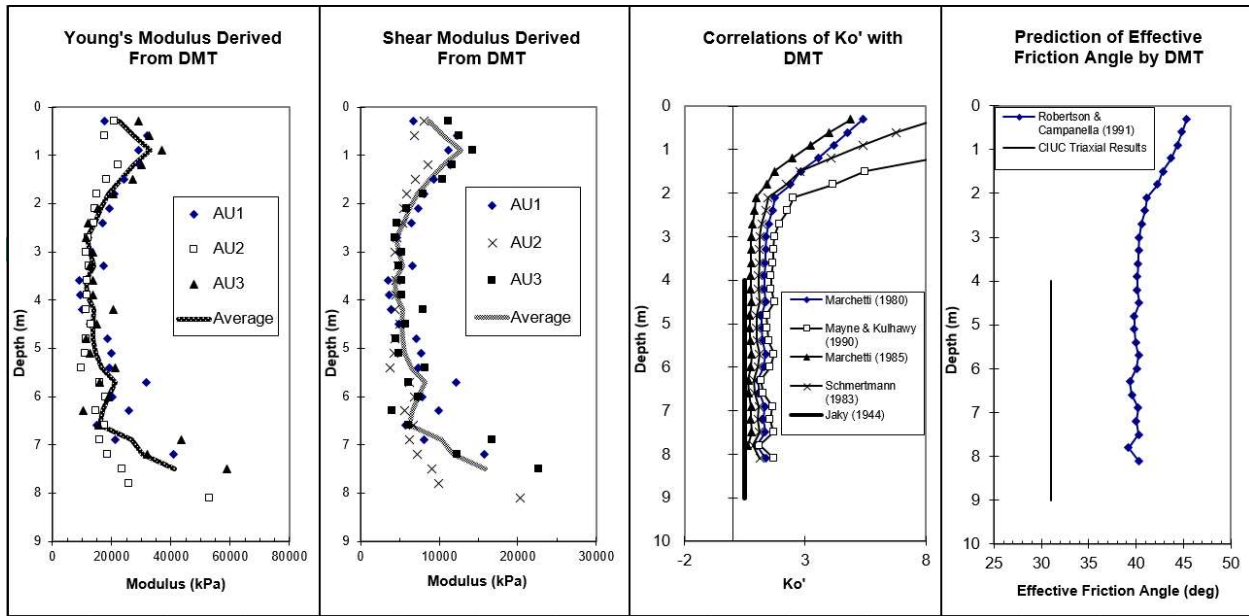


Figure 52. The result summary of DMT from Vinson and Brown (1997).

OBJECTID *	SHAPE *	Result	Latitude	Longitude	Desc_
1	Point	<Raster	<Null>	<Null>	AU1
2	Point	<Raster	<Null>	<Null>	AU2
3	Point	<Raster	<Null>	<Null>	AU3

Figure 53. The attribute table of DMT layer.

The seismic DMT layer is similar to the DMT layer. The “result” column presents the figures of the seismic DMT from Vinson and Brown (1997). This figure shows the depth vs. arrival time, depth vs. shear wave velocity and depth vs. G_{max} (Figure 54). The “description” column shows the locations of seismic DMT test. Figure 55 shows the attribute table for the seismic DMT layer.

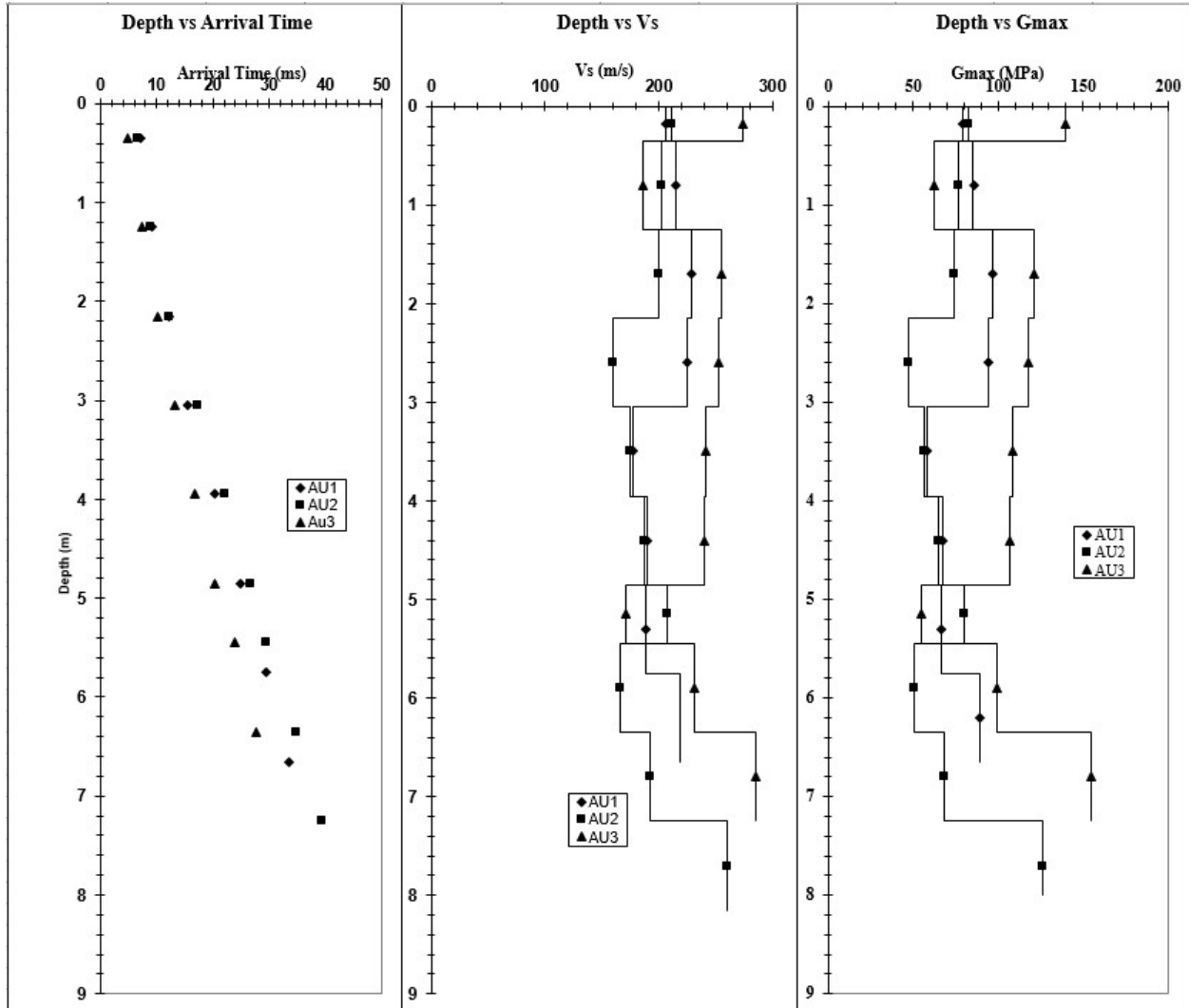


Figure 54. The result summary of seismic DMT from Vinson and Brown (1997).

Table						
SDMT_VsGmaxResult						
OBJECTID *	SHAPE *	Result	Latitude	Longitude	Description	
1	Point	<Raster >	<Null>	<Null>	AU1	
2	Point	<Raster	<Null>	<Null>	AU2	
3	Point	<Raster	<Null>	<Null>	AU3	

Figure 55. The attribute table of seismic DMT layer.

3.5 Limitation of this database

The data that discussed above has been input into a GIS database using ArcMap (SERI 2015) to provide future researchers with the locations and information on the foundations and in-situ tests that have been performed at the Spring Villa test site. The coordinates were surveyed using GPS equipment (Figure 20) and are subject to the normal uncertainties associated with this test method. The in-situ tests locations were either digitized from the previous research maps or were based on latitude and longitude that provided by the original author. One of the major challenges was finding maps which could provide accurate locations for the various explorations and foundations at the site. Most maps did not present coordinates for the foundations and in-situ tests and some did not include common features such as the drilled shafts. Some locations could not be accurately located using one of these previous maps. This additional uncertainty on locations must be considered by future researches when they use the database.

The foundations and in-situ tests were grouped by type and separate into different layers in the database. The information for each different type of foundation and in-situ test are stored separately based on each layer. The data such as pile length, pile type and construction method were input into the database as attributes for each point. The test curves such as SPT profile and load test curve were stored in images as raster data files. The links to the original reports and raw data (if available) also provided, so future researchers can locate information that not presented in the database.

CHAPTER 4: NUMERICAL MODELLING OF THE DRILLED SHAFT

4.1 Introduction

Several types of non-destructive test (NDT) methods have been developed to evaluate unknown or partially characterized deep foundations. These NDT methods can provide information about the type and length of the deep foundation and potentially about defects in the materials. Surface-based NDT methods for deep foundations often involve applying either an impulse or a controlled dynamic load to the foundation and measuring the response in terms of acceleration, velocity or displacement. While methods using impact loads are commonly used to evaluate unknown foundations, these methods can only provide reliable information about the length of the foundation. Dynamic response methods have the potential to provide additional information about the stiffness of the foundation and possible defects, but these methods often require expensive vibration testing equipment. Recent work at the Spring Villa NGES has attempted to use low cost tactile transducers to apply dynamic loads to the foundations, but the magnitude of the applied load is very small compared with the stiffness of the foundation and interpretation of the results was inconclusive.

This chapter presents results from numerical analyses of drilled shafts being subject to low amplitude dynamic loading similar to the loads that might be applied by tactile transducers. A 3D finite difference model was created using FLAC3D (Itasca 2011) to simulate the response of the drilled shaft when subjected to a sinusoidal force applied to the side of the shaft on the portion that site above the ground surface. The parameters of the drilled shaft and soil are obtained from Vinson and Brown (1997) and Brown (2002) to approximate the properties at the Spring Villa site. Limited sensitivity studies are performed to examine the effects of the shaft length and material properties

on the results. Preliminary findings from the models and suggestions for further sensitivity studies are discussed.

4.2 Background

Previous researchers have also used numerical simulations to help analyze the results from different NDT methods. A focus is placed in this chapter on surface-based method which can be performed relatively quickly and in a non-invasive manner. In this section, two of the most common surface-based NDT methods for deep foundations will be discussed.

4.2.1 Overview of Non-Destructive Test Method

The impulse response and impact echo methods are two common methods for NDT to analyze the length of deep foundations due to the easy set-up and inexpensive cost of performing the test (Jin and Chang 2009). These tests use an instrumented hammer to apply an impact force which generates a stress wave within the pile. The reflected response from pile tip or large defects are measured by one or several geophones or accelerometers on the top of the pile. The force and velocity signals that are received by the geophones or accelerometers are then used to estimate the length of the pile. This can be done by looking at the travel time or by using Fourier transforms to examine the response in the frequency domain. When analyzing the results in the frequency domain it is common to divide the velocity spectrum by the force spectrum to calculate the mobility. Base on the mobility plot, the depth of the reflection can be determined by measuring the frequency change between peaks, Δf (Finno and Chao 2000). Equation 1 shows how the length, L can be calculated based on Δf and V_c which is the wave propagation velocity in the deep foundation.

$$L = \frac{V_c}{2\Delta f} \quad (1)$$

The ultra-seismic tests operate on the same main principles, but the analyses are based on

joint time-history and spectrum calculations (Wang et al. 2017). The limitation for both of these methods is that the results are often influenced by the operation judgment and experience. This is because the tests rely on the impact force to generate stress waves at a variety of frequencies. Lack of experience may make it hard to obtain meaningful results and difficult to process the recorded signal.

4.2.2 Numerical Simulation of Non-Destructive Test

Finno et al. (1997) performed an impulse response test on drilled shafts at Northwestern University NGES. The field test results not always present a clear mobility curve, so numerical analyses were used to interpret the field-obtained signals. Finno et al. (1997) found the shafts length and diameter, and the density and wave propagation velocity of the concrete, along with soil parameters collected from field and laboratory tests. Initial comparisons of the field test results and the numerical models did not show perfect agreement as the quality of the concrete and cross-sectional area of the shafts changed during the construction. To solve this situation, Finno et al. (1997) changed the shaft and soil parameters in the numerical model to more accurately match the impulse response curves. The propagation velocity of the concrete was changed to match the peaks, the cross-section area was changed locally to match the mobility, and the soil properties were decreased to match the resolution and low-strain stiffness. The authors concluded that the construction procedures for installing drilled shafts can lead to variation in the dimensions of the drilled shafts. This coupled with the surrounding soil conditions could have a significant effect on the NDT results (Finno et al. 1997).

4.3 Numerical Simulation

Numerical simulations were performed in order to estimate the effects of the shaft and soil

properties on the dynamic response of the shaft to a low amplitude dynamic load. The work performed by Finno et al. (1997) demonstrated that the surrounding soil conditions will influence the results of NDTs, so the simulations for the current study need to include both the drilled shaft and the surrounding soil.

4.3.1 FLAC 3D

The software selected for these simulations was FLAC 3D Version 5 (Itasca 2011). The software was selected because it is commonly used in geotechnical practice to model dynamic problems and it has the ability to simulate both the drilled shaft and the surrounding soil. FLAC 3D is an explicit finite-difference software for geotechnical analyses (Itasca Consulting Group Inc 2011). Three-dimensional models of the site and drilled shaft were generated using FLAC's built-in programming language, FISH. Dynamic calculations were used to simulate the application of the external load and response of the shaft.

4.3.2 Shaft and Soil Properties

The initial geometry of the simulated drilled shafts was the same as the drilled shafts at the Spring Villa test site discussed Chapter 2, which is 0.9 m (2.95 feet) in diameter and 11 m (36 feet) deep with an additional 0.3 m (1 foot) of shaft located above the ground surface. This brings the total shaft length to 11.3 m (37 feet). Sensitivity studies were also performed using shafts with the same diameter and above ground length, the with different lengths of shaft below the ground. This included an 8 m (26.25 feet) shaft and a 6 m (19.7 feet) shaft.

The groundwater surface at the Spring Villa test site is seasonally changing, so for these simulations, the groundwater level is assumed to be at a depth of 4.5 m (14.8 feet) below the ground surface (Mayne and Brown 2003). The material properties of the drilled shaft and the soil properties of the piedmont residual soil were calculated based on the results in Vinson and Brown

(1997) and are listed in Table 8 below. These properties were used for all three shaft lengths.

Table 8. Baseline material properties for the drilled shaft simulations.

Properties	Drilled Shaft	Soil
Dry unit weight	2,402 kg/m ³	1,360 kg/m ³
Wet unit weight	-	1,860 kg/m ³
Elastic properties:		
Poisson's ratio	0.15	0.3
Bulk modulus	12.6 GPa	161,230 kPa
Shear modulus	11.48 GPa	74,414 kPa
Strength Properties:		
Cohesion	-	17 kPa
Friction angle	-	32 °

A set of sensitivity simulations was also performed to examine the effect of changing the elastic moduli of the soil and concrete on the results. The sensitivity study used the 8 m shaft and all of the baseline properties with the exception of the changes in the moduli of the soil and/or concrete. A total of six cases were examined. For case 1 and 2, the shear modulus and bulk modulus of the concrete and soil are all increased by 30% and decreased by 30%, respectively. For case 3, only the shear modulus and bulk modulus of the concrete are increased by 30%. For case 4, only the shear modulus and bulk modulus of the concrete are decreased by 30%. For case 5 and case 6, the shear modulus and bulk modulus of just the soil are increased by 30% and decreased by 30%, respectively. The specific stiffness for each case are listed in Table 9 below.

Table 9. Stiffness for the concrete and the soil from case 1 to case 7.

		Case 1	Case 2	Case 3	Case 4	Case 5	Case 6
Property	Material	All Soft	All Stiff	Soft Concrete	Stiff Concrete	Soft Soil	Stiff Soil
Shear Modulus (MPa)	Soil	52.1	96.7	74.4	74.4	52.1	96.7
	Concrete	8040	14900	8040	14900	11500	11500
Bulk Modulus (MPa)	Soil	113	210	161	161	113	210
	Concrete	8820	16400	8820	16400	12600	12600
Poisson's Ratio	Soil	0.3	0.3	0.3	0.3	0.3	0.3
	Concrete	0.15	0.15	0.15	0.15	0.15	0.15

4.3.3 Geometry of the Simulations

FLAC 3D uses hexahedral zones to create the simulation mesh. The current model was generated using three grid shapes: brick, cylinder and radial cylinder. These grid shapes allow for quick mesh generation by automatically creating hexahedral zones to fit the desired shape and dimensions. The radial cylinder mesh was used to represent the upper soil layers that surround the drilled shaft while the block mesh was used to represent the soil below the drilled shaft. The drilled shaft was formed using a cylindrical mesh. During mesh generation, the soil grid is created first. The drilled shaft grid is created separately and then moved into the soil grid. Figure 56 shows a cut through the center of the mesh including the drilled shaft grid and the soil grid before the drilled shaft grid is moved into place.

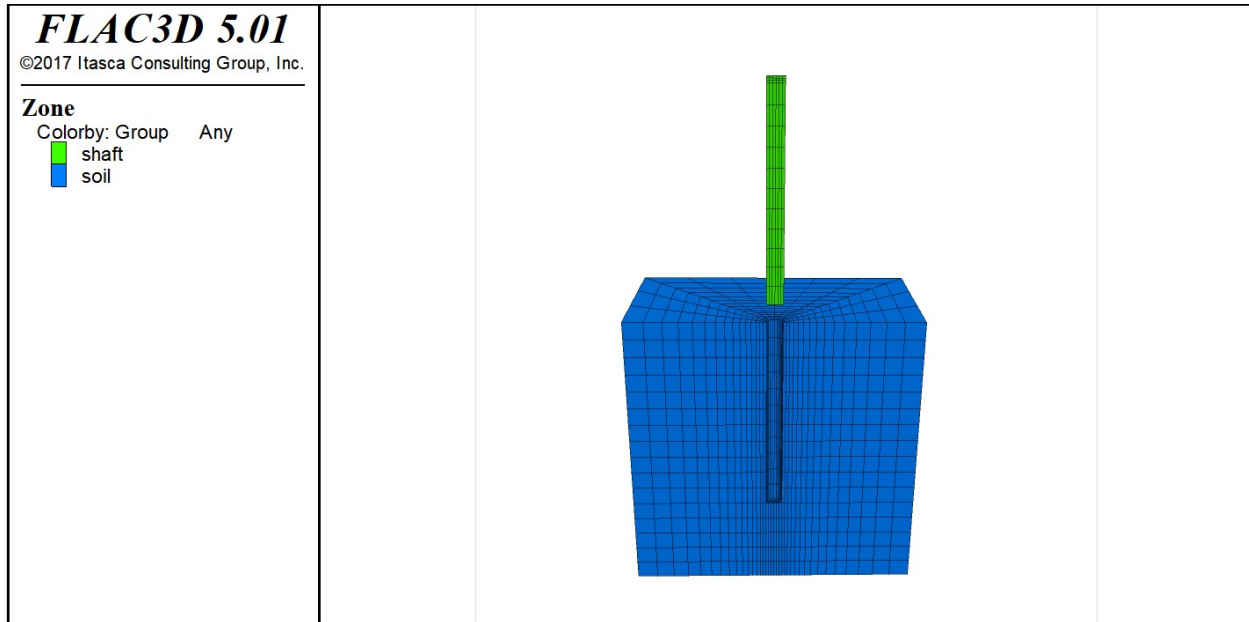


Figure 56. Model of drilled shaft grid and the soil grid for 11-meter shaft length simulation.

A vertical plane through the drilled shaft axis is a plane of symmetry for this analysis, but to capture any three-dimensional effects, the full mesh was generated. The coordinate axes for the model are located with the origin at the top of the drilled shaft, and the z-axis oriented along the drilled shaft axis and upward. The model grid for 11-meter (m) simulation is shown in Figure 57. The top of the model, at $z = 0$, is a free surface. The base of the model, at $z = -16$ m, is fixed in the z-direction, and roller boundaries are imposed on the sides of the model ($x = -8$ m, $x = 8$ m, $y = 8$ m and $y = -8$ m). The axial-bearing capacity of a drilled shaft is a function of the skin friction resistance along the drilled shaft and the end-bearing capacity at the drilled shaft tip. The skin friction resistance is modeled by placing an interface between the drilled shaft walls and the soil. The friction and cohesion properties of the interface represent the same properties as the soil. For this simulation, a friction angle of 32° and a cohesion of 17 kPa are assumed for the interface properties just same as the soil layer properties. A second interface is placed between the drilled shaft tip and the residual soil. The shaft length in Figure 57 includes 11 m depth and 0.3 m head

of the shaft which is located above the ground surface.

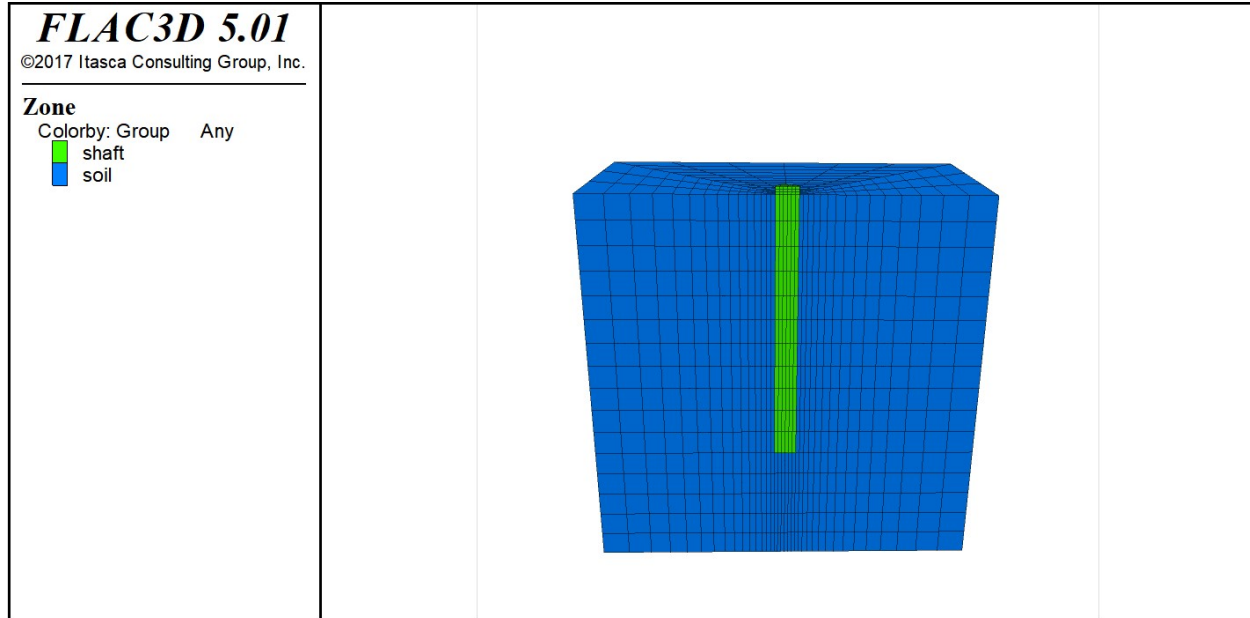


Figure 57. Model of the drilled shaft in soil for 11-meter shaft length simulation.

The 8-meter length shaft and 6-meter length shaft simulation are created in an identical manner to the 11-meter simulation. The shaft length are 8 meters and 6 meters from the free surface into the soil grid. Both shafts have the same 0.3 m head located above the ground surface. Figure 58 and 59 present the simulation mesh for 8-meter shaft and 6-meter shaft, respectively.

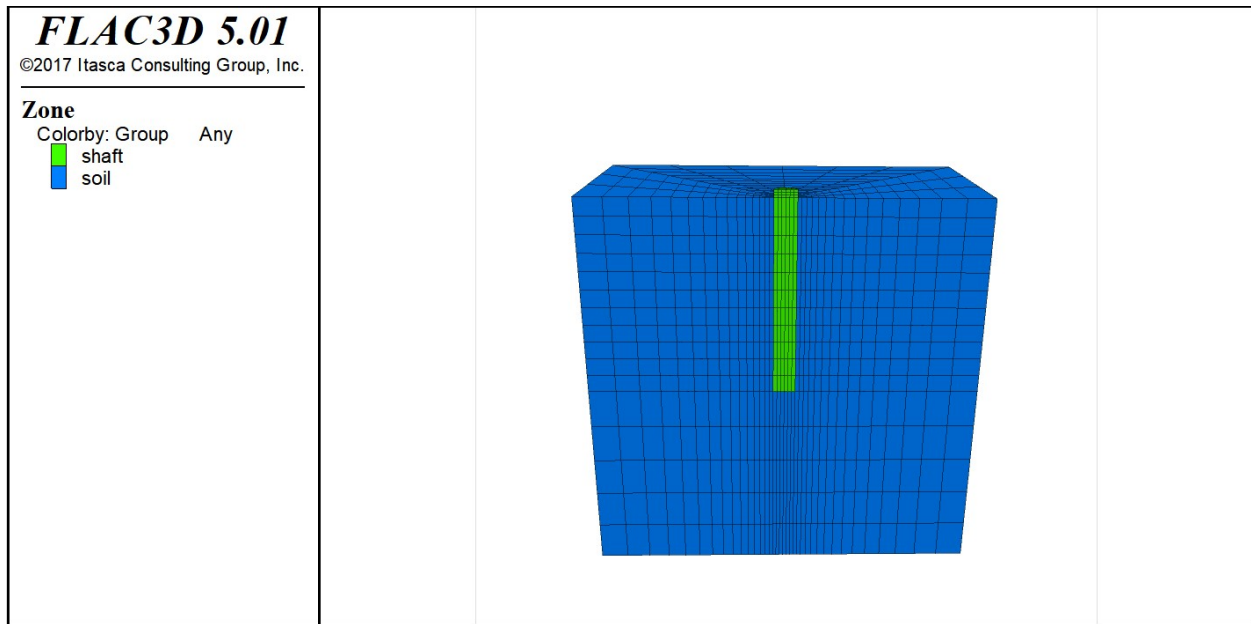


Figure 58. Model of the drilled shaft in soil for 8-meter shaft length simulation.

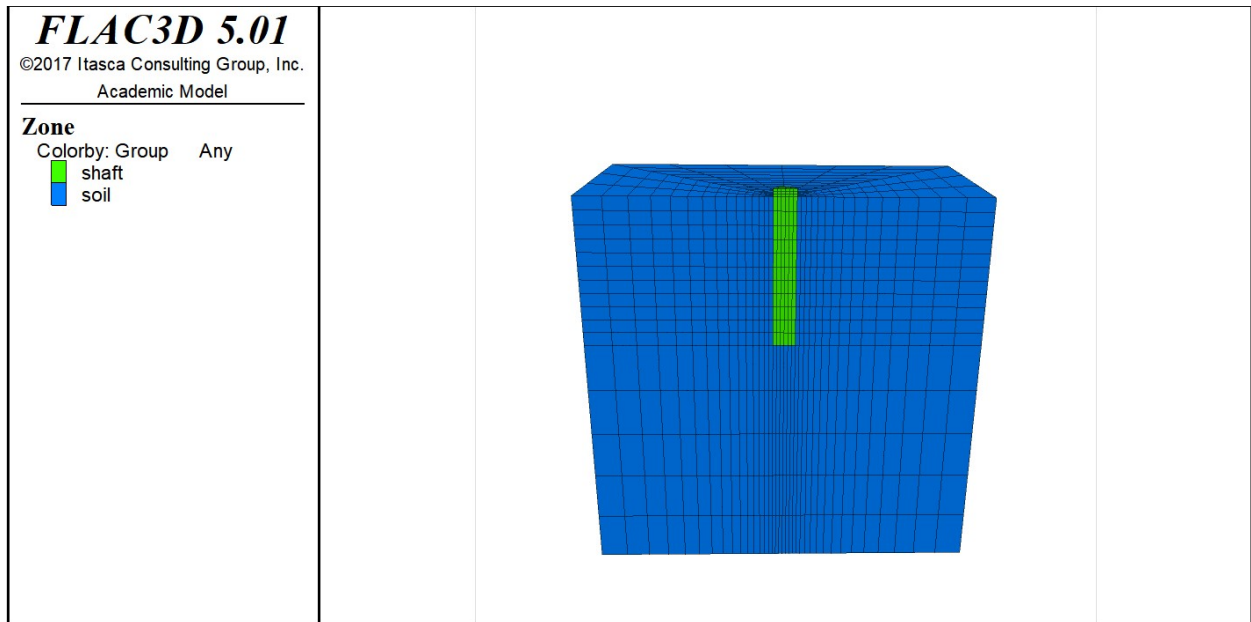


Figure 59. Model of the drilled shaft in soil for 6-meter shaft length simulation.

4.3.4 Equilibrium Stress-State of the Simulations

Obtaining accurate results for the dynamic loading requires obtaining a reasonable initial stress state. This was accomplished by solving for equilibrium in two stages. In the first stage, the

model is brought to an equilibrium stress-state under gravitational loading without the drilled shaft (i.e., the drilled shaft zones are modeled as soil). A horizontal water table is created at $z = -4.5$ m, and the wet density of the Piedmont residual soil is assigned to the zones below the water table. The boundary conditions are selected to represent 1-D consolidation which means, the bottom of mesh is fixed in the z-direction, two sides of model are fixed in the x-direction and two sides are fixed in the y-direction. Stresses are initialized assuming 1-D loading and the model is brought to equilibrium.

In the next stage of analysis, the drilled shaft is installed. The “installation” is modeled by changing the properties of the shaft zones from the properties representing the residual soil material to those representing the drilled shaft material. The stresses within and beneath the shaft are recalculated due to the change in unit weight and the model is brought to equilibrium under gravity loading. The vertical stress-distribution at the equilibrium state for 11-meter shaft length, 8-meter shaft length, and 6-meter shaft length are shown in Figure 60, 61 and 62, respectively.

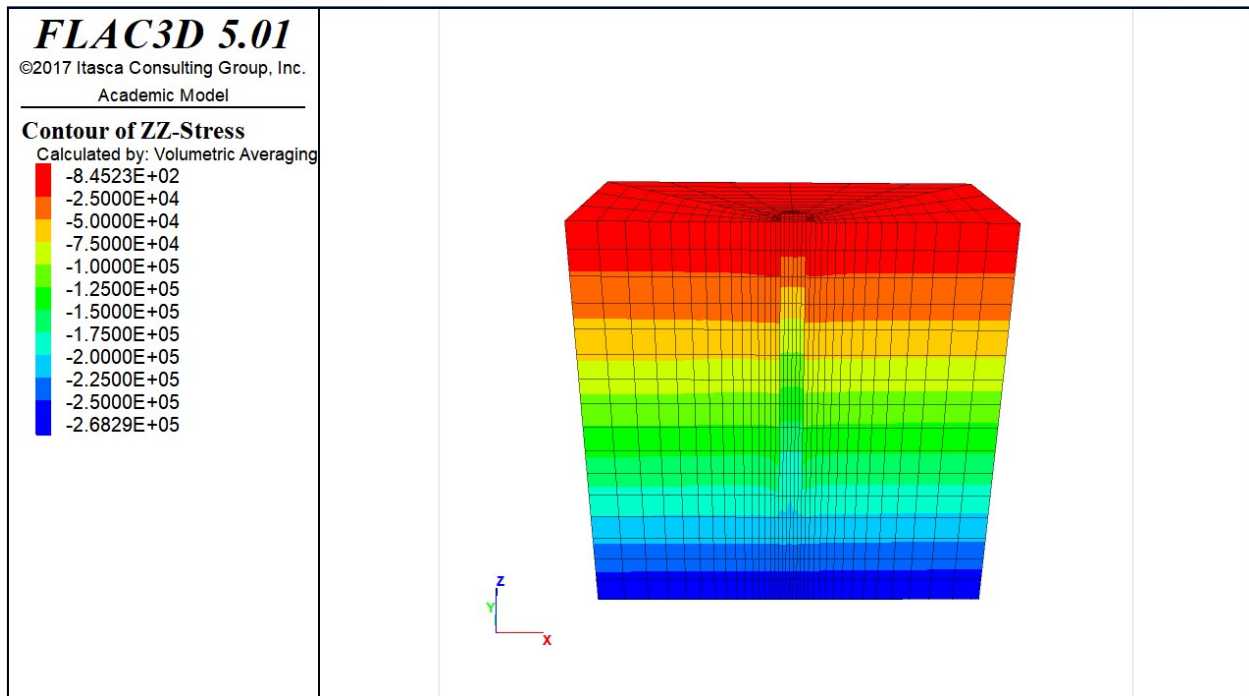


Figure 60. Contours of the initial equilibrium stress-state for 11-meter shaft length simulation.

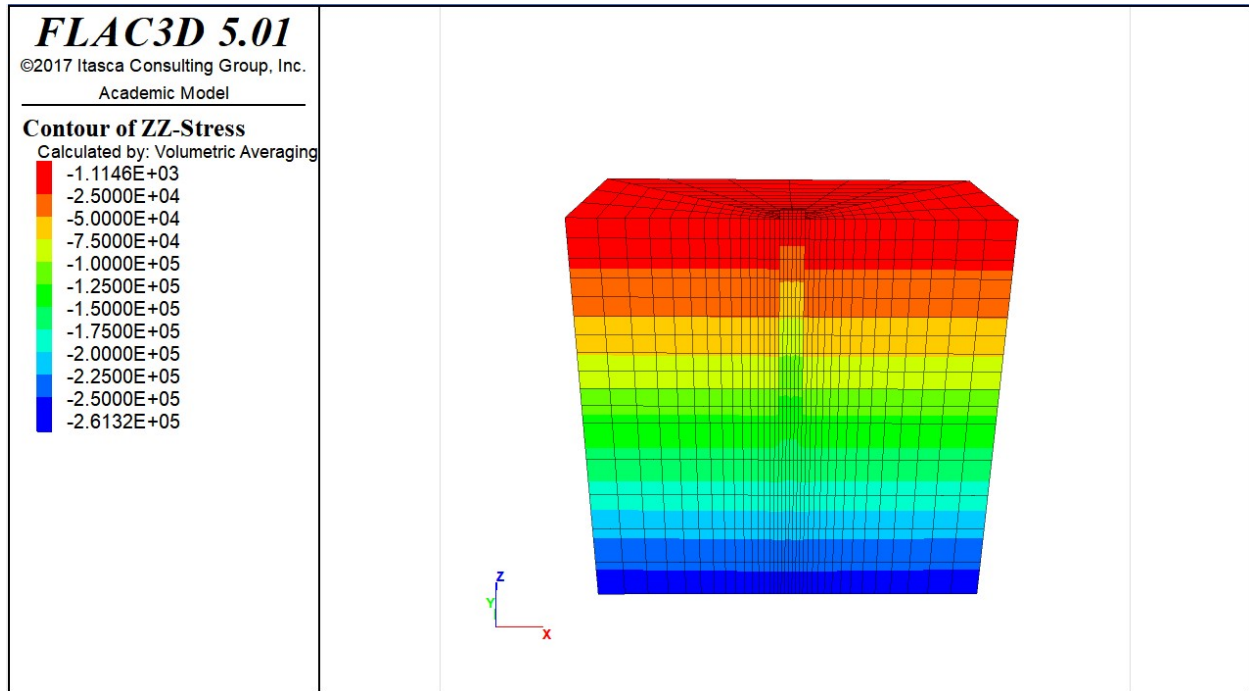


Figure 61. Contours of the initial equilibrium stress-state for 8-meter shaft length simulation.

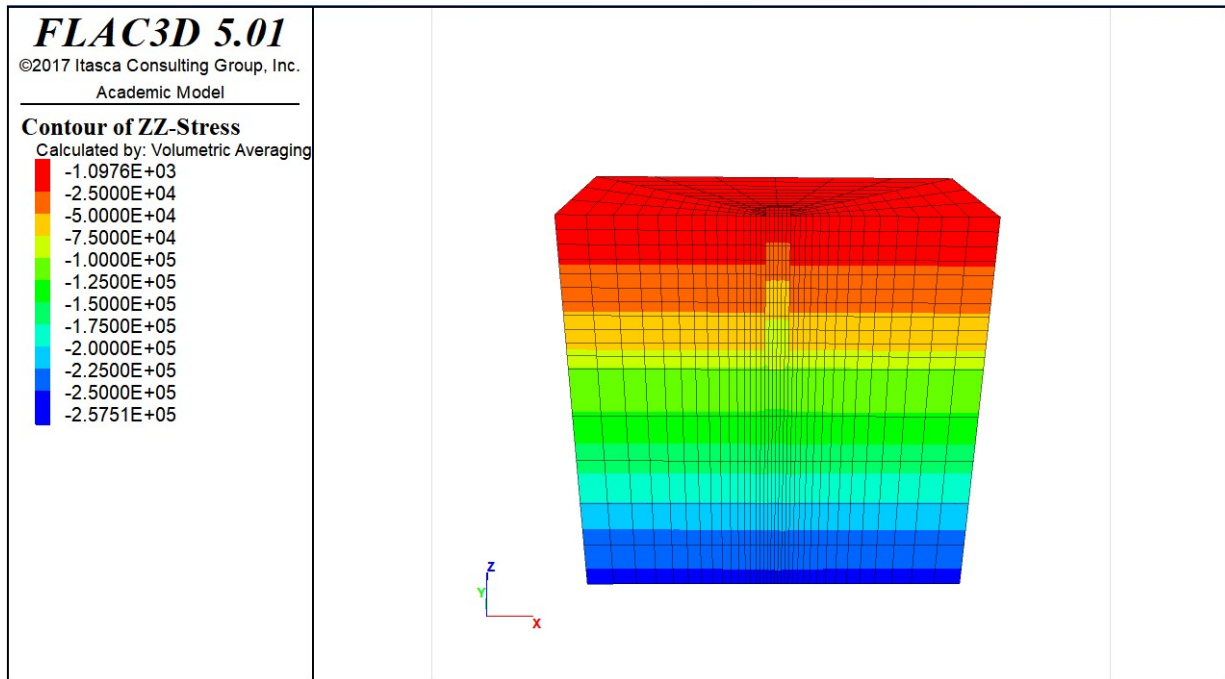


Figure 62. Contours of the initial equilibrium stress-state for 6-meter shaft length simulation.

4.3.5 Dynamic Analysis of the Simulations

In order to simulate the dynamic loading, the boundary conditions must be changed. In the

current simulation, quiet boundaries were used to along all external boundaries. These boundaries help minimize wave reflections by acting as a viscous boundary and absorbing the energy of the wave (Itasca 2011). The quiet boundary is added on the side of the model, the bottom of the z-direction, at left hand $x = -8$ m, right hand $x = 8$, at $y = 8$ m and $y = -8$ m. After applying the quiet boundary, the model was resolved to ensure it was still in equilibrium.

The loading from the transducer was simulated by applying a sinusoidal force with an amplitude of 30 N to a single grid point. The grid point is located 0.1 m from the top of the shaft on the portion of the shaft which is above the ground surface. The force was applied at a 45-degree from the ground surface in order to generate multiple types of waves within the shaft. The frequency of the applied load was either 20 Hz, 60 Hz, 120 Hz, 250 Hz or 500Hz. The simulations were performed using either the baseline properties or the variations described above. The different combinations of simulations are summarized in Table 10.

Table 10. Summary of frequency and property combinations for all simulations.

Simulation	Loading Frequencies (Hz)
Baseline properties, lengths of 6 m, 8 m or 11 m	20, 60, 120, 250, 500
Properties from Case 1 to Case 6, 8 m length	20, 60, 120, 250, 500

The response of the drilled shaft was recorded at four points located on the head of the drilled shaft. At each point the acceleration time histories from x, y, and z directions were recorded. Figure 63 and 64 provides a cross-section and plan view of the shaft head indicating where the four points are located. Point 1, 2, and 3 are located at the edge of the shaft, point 4 is at the top center of the shaft.

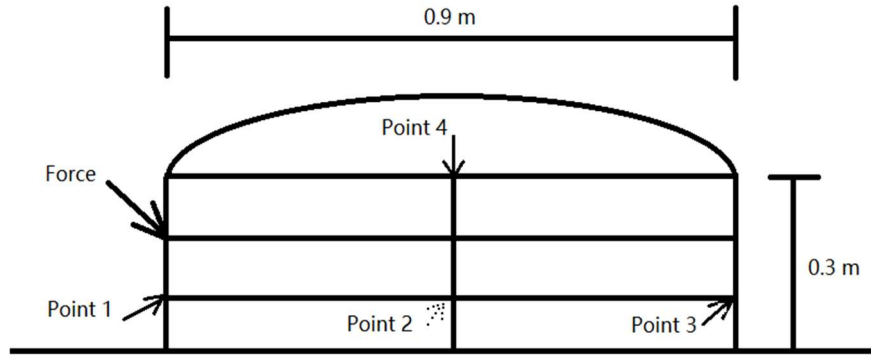


Figure 63. Cross-section through the center of the shaft showing the location of recording points.

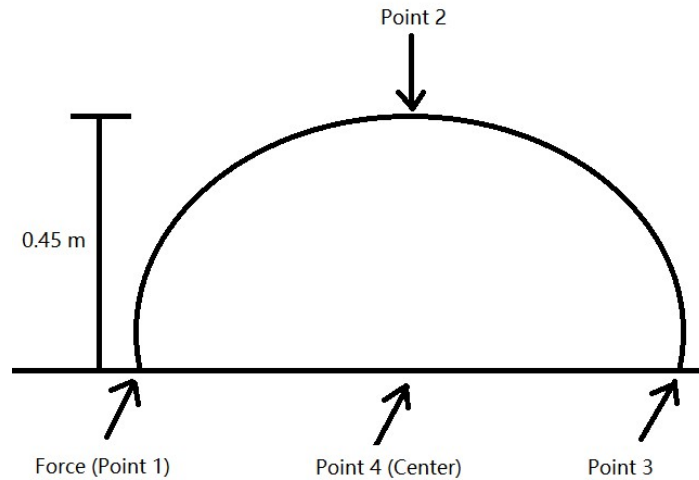


Figure 64. Plan view of half of the shaft showing the locations of the recording points.

4.4 Simulation Results

The simulations were conducted by applying the force to the top of the pile for three seconds and the data is recorded in every 100 steps in all the simulations. The initial application of the dynamic load introduces some large accelerations into the system and so the results presented here are shown for the final two second. This allows the large accelerations from the initial application to damp out and for the model to reach an approximately steady-state response.

The baseline simulations were performed first for the drilled shaft length of 11 m. This case

most closely represents the actual conditions at the Spring Villa site. As were previously discussed accelerations are recorded in all three directions and for four separate points along the top of the shaft. This leads to a total of 12 time-histories per simulation. An example of the response at point 1 for a loading frequency of 60 Hz is shown in Figure 65. The response is seemingly periodic with the largest accelerations in the z-direction and smallest in the y-direction. This is expected as the force being applied in both the x- and z-directions. Time histories for other points and other frequencies show similar responses and are presented in Appendix A.

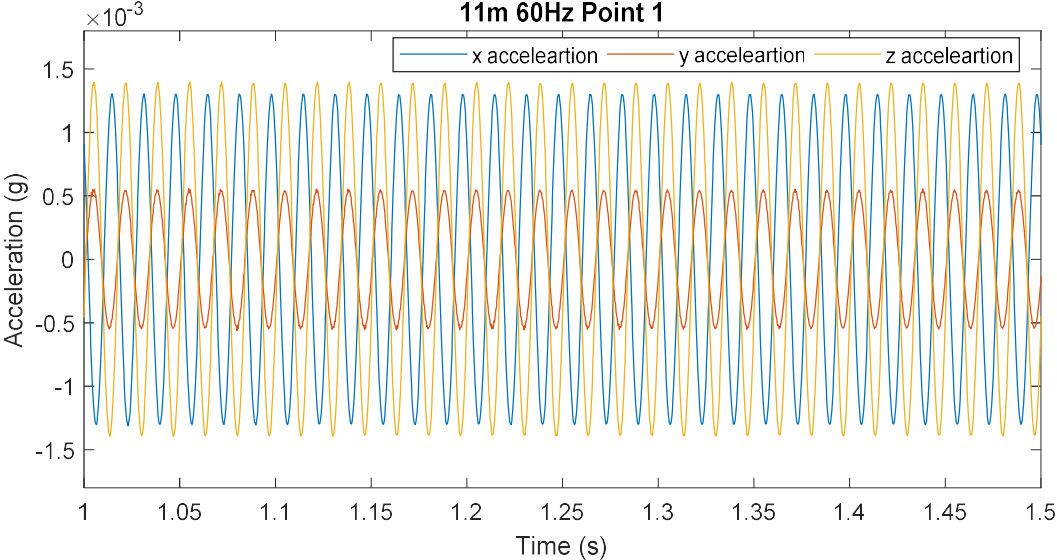


Figure 65. Acceleration time histories for three directional components and a loading frequency of 60 Hz. Simulation results for an 11 m shaft length with the baseline properties.

It is difficult to determine much about the response of the shaft from the time history response as the overall acceleration is dominated by the applied load. In order to examine the response at other frequencies, the time histories were used to compute power spectral density (PSD) functions. A PSD is used to show how the power of a signal is distributed over various frequencies. While Fourier transforms are commonly used to examine periodic signals, PSD functions can be used to examine the response of more random signals. The motivation behind using this for the

current study is that the shaft may oscillate at frequencies closer to its natural frequency as the applied load interacts with the boundaries of the shaft and surrounding soil. These interactions may not be periodic, but are expected to be relatively evenly distributed in time and so may show up in a PSD plot. The PSDs were computed using the build-in function in MATLAB (Warwick 2003). A Kaiser window with $\beta = 38$ was used as this is the default configuration when computing periodogram using the Signal Processing Toolbox. The sensitivity of the findings to this may be examined in the future studies.

The PSD for the baseline analysis of the 11-m shaft is shown in Figure 66a for x-acceleration at point 1. The PSD is computed independently for each loading frequency. The results show that most of the power in each signal is located at the frequency of the applied load. The response at the other (non-loading) frequencies might be characterized as noise, but there is a region near 100 Hz where each of the curves has approximately the same amplitude. This can be seen more clearly by focusing on just region of the PSD curve (Figure 66b). The PSD curves for all five loading frequencies overlap in the region between approximately 80 and 120 Hz with a peak at approximately 90 Hz. The reason for this behavior is not clear, but it is believed that this may correspond to one of the natural frequencies of the soil-shaft system. This point can be further illustrated by examining the PSD functions of both the y- and z-accelerations (Figure 67). These PSD functions show a similar pattern with clear peaks near 95 Hz although the response at other frequencies varies significantly between the different directions and different loading frequencies. The response in the z-direction shows the clearest peak (Figure 67b). The results discussed above are only for a single point on the shaft. Individual component responses for other points showed similar responses and these PSD plots are shown in Appendix B.

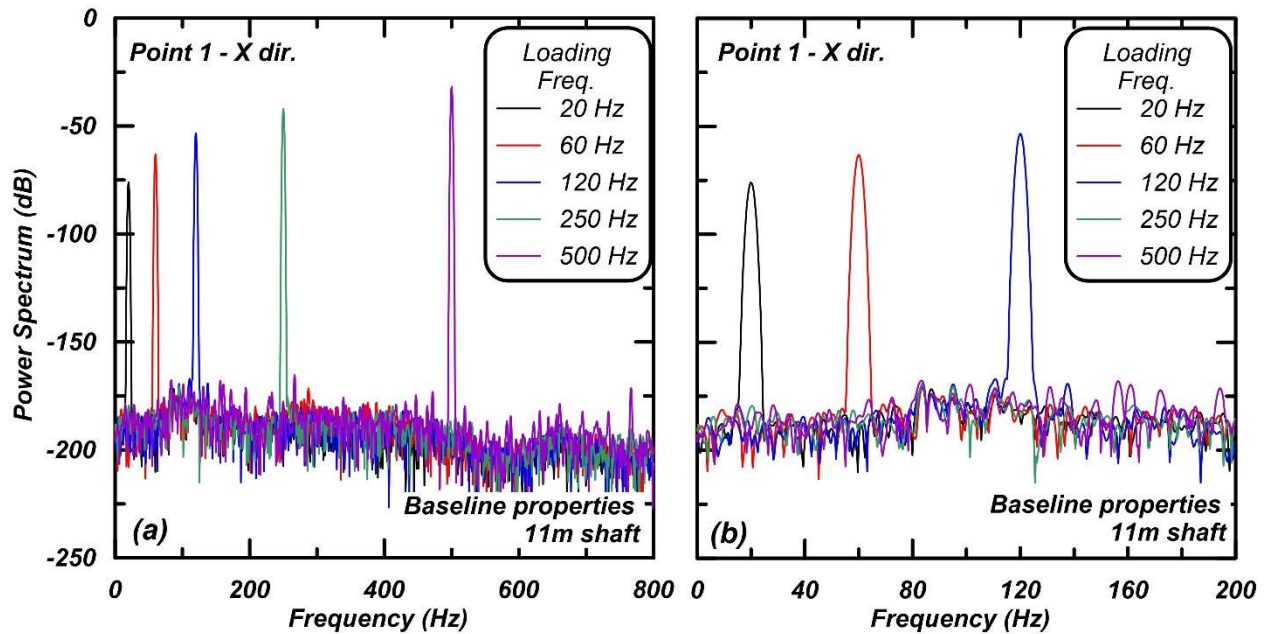


Figure 66. Power spectral densities for x acceleration at point 1 on the 11 m shaft over a wider range (a) and a narrower range (b) of frequencies.

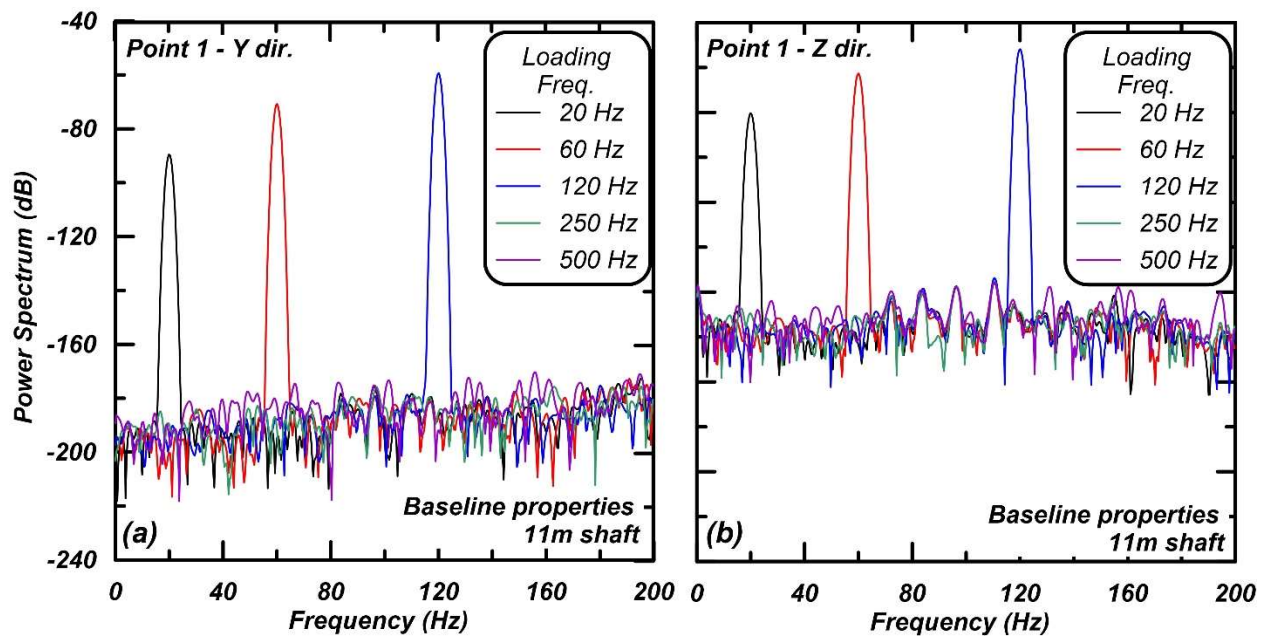


Figure 67. Power spectral densities for point 1 on the 11 m shaft using the y-acceleration (a) and z-acceleration (b) time histories.

The results discussed above showed that the acceleration recordings from different loading frequencies tended to have a similar power over a narrow range of frequencies near 90 Hz. The response at the other frequencies varied significantly depending on the frequency of the applied

load. More quantitative estimates of this range of similar response were obtained by computing the median power at each frequency from each of the loading curves (Figure 68). The idea behind this was that at frequencies where all of the loading curves had a similarly high value, the median power would clearly reflect that high value. At frequencies where the loading curves had more random responses, the median would likely take on a lower value due to the peaks of the various curves not exactly aligning. With the exception of point 2, the median PSD functions show similar patterns to those discussed above with peaks occurring near 85-100 Hz. These peak is most clearly defined in the z-direction at point 3, so future discussions in this chapter will focus on examining how the frequency of this peak value shifts with changes in shaft length and material properties.

The first simulation property that was changed was the length of the concrete shaft. Simulations were performed using the baseline properties and shaft lengths of 8 and 6m, respectively. The overall thickness of the soil stayed constant in these simulations. PSD functions for the individual loading frequencies for these simulations are also shown in Appendix B. The median PSD function were computed using an identical procedure to the one used for the 11 m shaft. These results are compared with the 11 m shaft for the z-acceleration at point 3 in Figure 69. The frequency corresponding the peak power is highlighted using a colored rectangle. This figure clearly shows that the frequency corresponding to the peak power becomes higher as the shaft length decreases. This is expected because the natural frequency of the shaft is inversely related to the length.

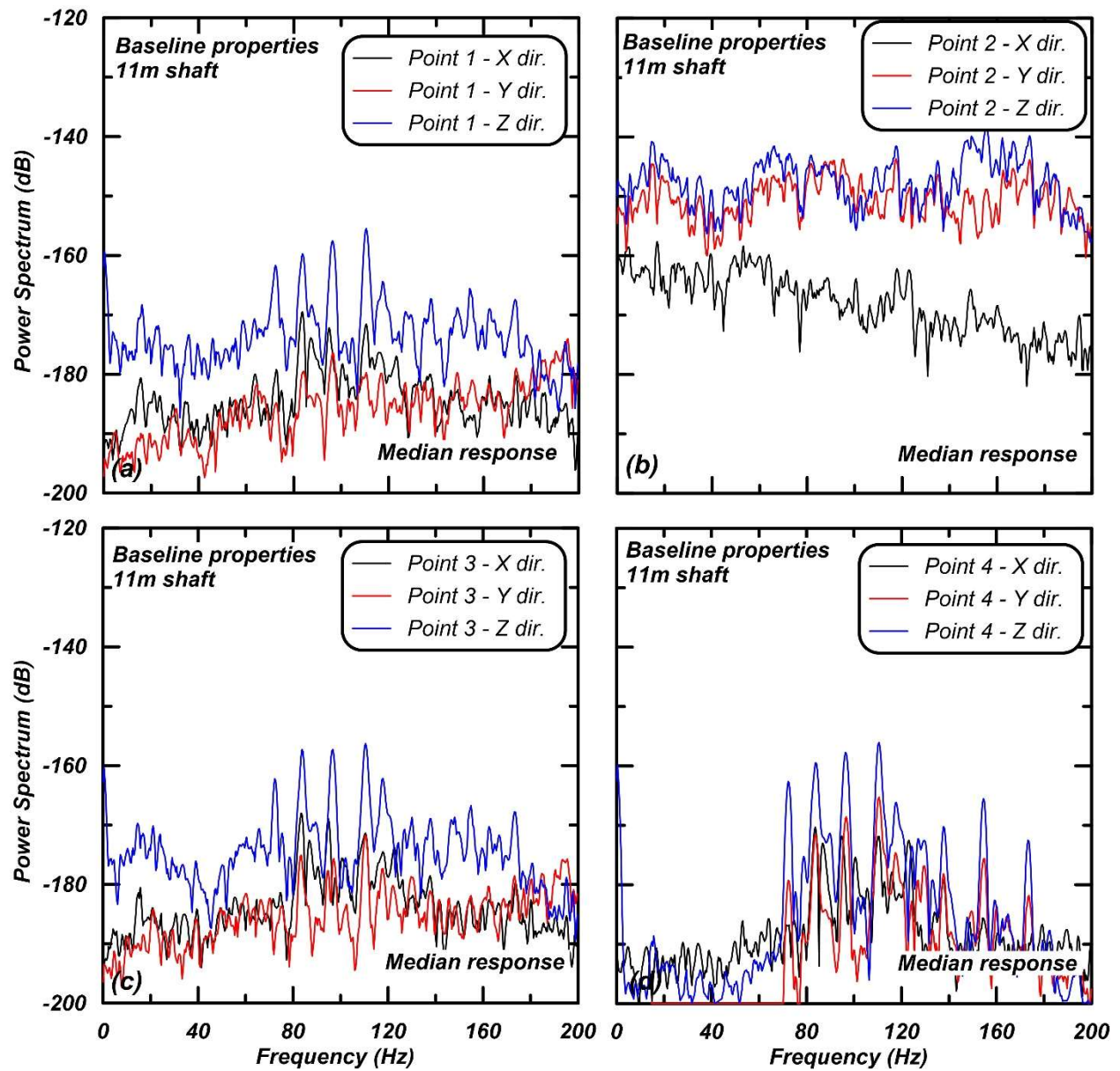


Figure 68. Median power spectral densities for the 11 m shaft using each of the acceleration components for points 1 (a), 2 (b), 3 (c) and 4 (d).

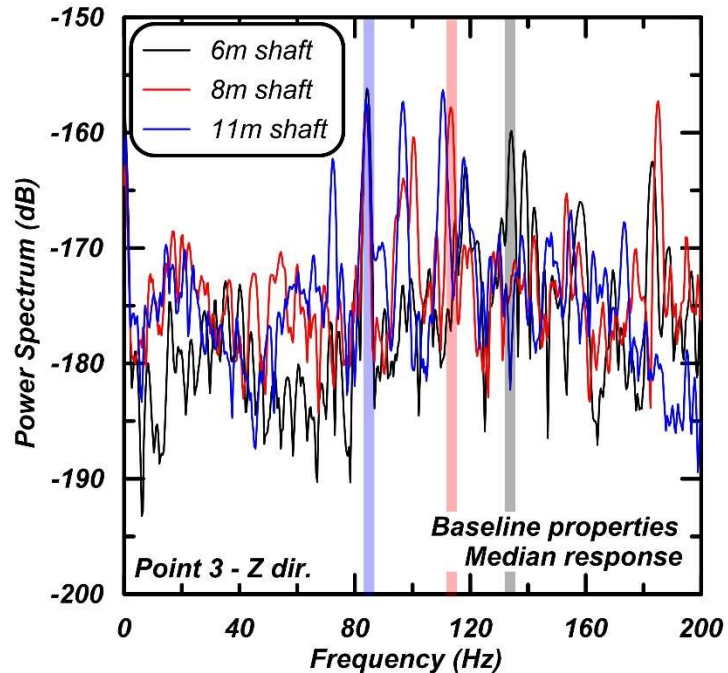


Figure 69. Median power spectral densities are shown for acceleration in the z-direction at point 3 using the baseline properties and three shaft lengths.

Further sensitivity analyses were performed to examine how the peak frequency changed with changes in the material properties. These simulations used the 8 m shaft and either increased or decreased the elastic moduli of the soil and/or concrete, as previously discussed (Table 9). The goal of this sensitivity study was to determine whether the stiffness of the soil or concrete was the primary influence on the magnitude of the peak frequency. The first cases either increased or decreased the elastic moduli of both the soil and concrete by approximately 30% (Case 1 and 2). The PSD functions for these cases are compared with the baseline properties in Figure 70. The peak frequency decreases when the stiffness is reduced and increases when the stiffness is increased, as expected. In the second set of cases, the stiffness was either decreased or increased in the concrete (Case 3 and 4) and the soil (Case 5 and 6) individually. This was done to isolate the effects of changes in each material. The PSD function for these four cases are compared with the baseline analyses in Figure 71. The peaks for case 2 and 3 nearly exactly align with the baseline

case indicating that changes in the stiffness of the concrete did not change the frequency at which the peak response occurred. The response does not align at other frequencies indicating that the change in concrete properties did change the response, but not the peak. The peak frequency for case 5, where the stiffness of the soil was decreased was lower and matched the frequency for case 1 where the stiffness of both the soil and concrete were decreased. The same observations can be made for case 6 and case 2.

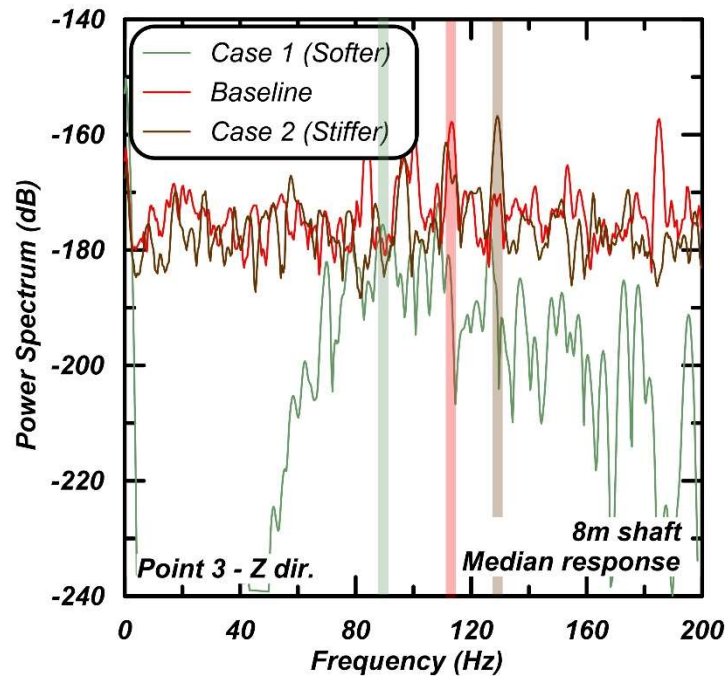


Figure 70. Median power spectral densities are shown for acceleration in the z-direction at point 3 using the 8 m shaft and three sets of properties.

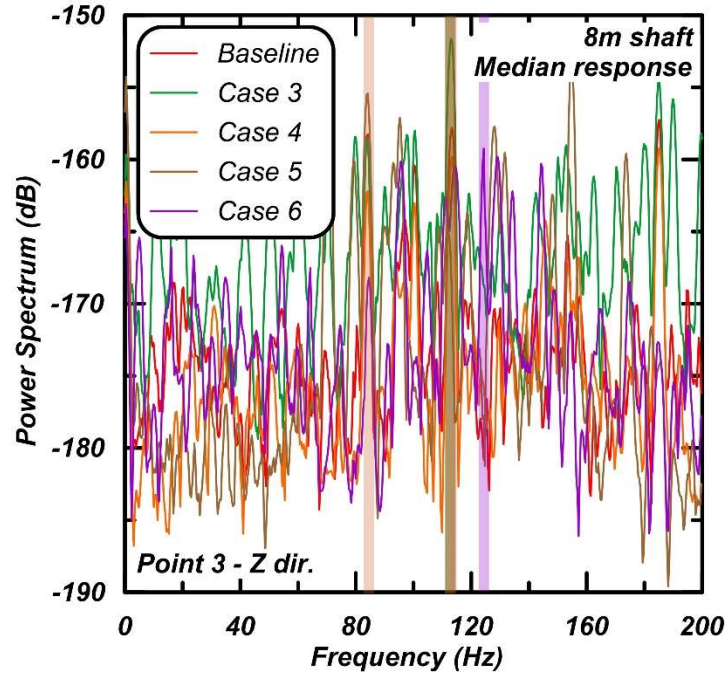


Figure 71. Median power spectral densities are shown for acceleration in the z-direction at point 3 using the 8 m shaft and five sets of properties.

4.5 Discussion

The simulation results presented in the previous section demonstrate that the PSD functions computed for different loading frequencies tended to have a similar power over a narrow range of frequencies. The values of this power are above the level of seemingly random accelerations seen at other frequencies. Median PSD functions were computed by taking the median power at each frequency using accelerations from the five different loading frequencies. From these median PSD functions the peak frequency, the frequency corresponding to the peak power value, were selected. This peak frequency increased as the shaft length decreased and as the stiffness of the soil increased. These results both make sense as the natural frequency of the soil-shaft system would be expected to be higher for shorter, stiffer zones. The peak frequency was not sensitive to the stiffness of the concrete, which was an unexpected result and needs to be confirmed with further studies. Further studies are also needed to develop equations to predict the magnitude of the peak frequency.

The results presented above represent a first attempt at modeling a NDT using low amplitude dynamic loading. While some promising patterns have been found, it is important to note that there are multiple spikes in the median PSD functions and selecting a single peak may be difficult and potentially misleading. It is not known whether these other peaks correspond to other natural frequencies in the soil-shaft system or some other numerical artifact. Further sensitivity studies are needed to determine this. The selection of a peak frequency may also be sensitive to the method used to compute the PSD function and this should also be explored in future studies. Additional studies are also needed to examine the effects of boundary conditions, a wider range of material properties, magnitude of the loading force and different soil depths. These studies will need to be conducted before any firm conclusions can be drawn about the feasibility of this type of NDT method, but the simulation results presented in this chapter demonstrate the potential of this method to investigate the natural frequency of the soil-shaft system.

CHAPTER 5: CONCLUSIONS AND FUTURE DIRECTION

5.1 GIS Database Summary

There have been many previous studies performed at the Spring Villa test site which have collected a significant amount of data on both the soil and foundation properties. These studies represent a major investment of time and money by the researchers and the respective funding agencies, including ALDOT, the Highway Research Center and NCHRP. Despite this large body of research, no previous database existed that tied together the information from these studies. The primary objective of this thesis was to develop a GIS database which includes the results of in-situ tests and foundation tests from previous research papers and can be easily updated by future researchers who use the Spring Villa test site for their project.

5.2 GIS Database Conclusion

The primary goal was to develop a GIS database that summarize all the information of in-situ tests and foundations. The author has concluded the following:

- The GIS database presented in this thesis fills this gap by providing a publicly available database that has locations of both in-situ tests and foundations, along with relevant information about each.
- The database focused on foundations which currently exist at the site and does not include information on the foundations that were previously removed.
- The database still has limitations. One major challenges for creating this database was collecting the locations for the in-situ tests and foundations at the test site. Most studies provided a map to show their individual investigations, but these maps did

not provide coordinates or show existing structures which would have allowed their coordinates to be identified. The most accurate coordinates in the database are those for the foundations which were surveyed as part of this study.

- The locations of the in-situ tests are located and digitized based on these maps and the surveyed coordinates. This causes some additional uncertainty which future users must be aware of.
- The database can be updated as the new research paper and theses are made available allowing future researchers to better utilize the site for evaluation foundations and in-situ tests in residual soils.

5.3 Numerical Simulations Summary

Several simulations for evaluating the response of a drilled shaft to low amplitude dynamic loading. The properties for the drilled shaft and soil were based on the properties found for the Spring Villa site in previous studies (Vinson and Brown 1997 and Brown 2002). The simulations were conducted by first ensuring reasonable static stresses within the shaft and then applying a low amplitude sinusoidal load to the upper exposed portion of the drilled shaft. The acceleration response was recorded at four different points along the shaft and these records were used to interpret the dynamic response of the shaft. Limited sensitivity studies were performed including examination of 8-meter and 6-meter shaft lengths and different combinations of soil and concrete stiffness. Power spectral densities were calculated for each of the acceleration components and all four recording points.

5.4 Numerical Simulations Conclusion

The primary objective of the numerical simulations in this thesis was to examine the response of a drilled shaft to low amplitude sinusoidal loading using numerical simulations. Based on the results from FLAC 3D, the author has concluded the following:

- The results showed that each of the records for all of the tested loading frequencies had a small, but significant power component over the same narrow range of frequencies. A median power spectral density function was calculated using the results from the individual loading frequencies and showed a reasonably defined peak value. This peak frequency followed some expected trends for the natural frequency of a structural system, including increasing with decreasing length of the shaft and with increasing stiffness.
- Surprisingly the peak frequency was not significantly affected by changes in the stiffness of the concrete, but was affected by changes in stiffness of the soil. These trends need to be confirmed through further sensitivity analyses and field testing.
- This simulation offers a promising path forward for using low amplitude, dynamic loads coupled with triaxial acceleration measurements to perform NDT of deep foundations. Previous testing used single axis accelerometers which may have partially contributed to the inconclusive result.

5.5 Recommendations for future research

Several opportunities exist to further the work completed as part of this thesis. These include:

- The database should continue to be updated as new studies are completed. This will ensure that the database stays relevant and includes the latest information about the site.

- Auburn researchers have begun the process of establishing a benchmark at the site which can be used for future surveys. This work should be completed.
- The test site is relatively homogenous, but previous researchers have pointed out some variation in load test data to site variability (e.g. Brown 2002). Future researchers should be aware of this and perform more explorations to quantify the variability and get more accurate correlations between the in-situ and foundation load tests.
- The numerical simulations presented as part of this thesis represent a first attempt at interpreting the results of low amplitude dynamic tests on drilled shafts. This work should be expanded with further sensitivity tests to confirm some of the correlations observed in this thesis.
- Future researchers can also apply the interpretation methods used for the numerical simulations to field tests using tactile transducers and triaxial accelerometers. This information could be very useful to determine whether the results of the numerical simulations agree with the results of field tests.

REFERENCES

- ASTM (2013). "D1143 Standard test methods for deep foundations under static axial compressive load." ASTM International, West Conshohocken, PA.
- Brown, D. A. (2002). *The Effect of Construction Technique on Axial Capacity of Drilled Foundations*. Auburn University Highway Research Center, Auburn, Alabama.
- Brown, D. A., O'Neill, M. W., Hoit, M., McVay, M., El Nagger, M. H., and Chakraborty, S. (2001). *Static and Dynamic Lateral Loading of Pile Groups*. Auburn University Highway Research Center, Auburn, Alabama
- Burrage, R. J. (2016). *Full Scale Testing of Two Excavations in an Unsaturated Piedmont Residual Soil*. Ph.D. Dissertation, Auburn University, Auburn, Alabama.
- Brown, D. A., and Drew, C. (2000). "Axial capacity of augered displacement piles at Auburn University." *Proc., Geo-Denver 2000*, ASCE, Reston, VA, 397-403.
- Chakraborty, S. (2000). *Dynamic lateral load testing of deep foundation groups*. Ph.D. Dissertation, Auburn University, Auburn, Alabama.
- ESRI (2015). *ArcGIS Desktop: Version 10.3*. Environmental Systems Research Institute.
- Finno, R. J., and Chao, H. C. (2000). "Nondestructive evaluation of selected drilled shafts at the Central Artery/Tunnel Project." Structural Materials Technology IV-An NDT Conference, New York State Department of Transportation, New Jersey Department of Transportation, and Federal Highway Administration, Atlantic City, New Jersey, 81-86.
- Finno, R. J., Gassman, S. L., and Osborn, P. W. (1997). *Non-destructive evaluation of a deep foundation test section at the Northwestern University national geotechnical experimentation site*. A Report Submitted to the Federal Highway Administration Office, Northwestern University, Evanston, Illinois.
- Georgia Tech (2000). "Seismic Cone Testing at Spring Villa NGES." Georgia Institute of Technology, <<http://geosystems.ce.gatech.edu/Faculty/Mayne/Research/summer2000/opelika/opelika.htm>> (August 13, 2017).
- Itasca Consulting Group, Inc. (2011). *FLAC (Fast Lagrangian Analysis of Continua)*, Version 7. Minneapolis, U.S.A.
- Jin, H. W. B. T. C., and Chang, J. W. T. P. (2009). "Identification of resonant frequency on concrete piles using guided wave theory." The 13th Conference on Current Researches in Geotechnical Engineering, Taiwan, China.
- Marshall, J. D., Anderson, J.B., Campbell, J., Skinner, Z., and Hammett, S.T. (2017). *Experimental validation of analysis methods and design procedures for steel pile bridge bents*. Auburn

University Highway Research Center, Auburn, Alabama.

- Mayne, P. W., Brown, D., Vinson, J., Schneider, J. A., and Finke, K. A. (2000). "Site characterization of Piedmont residual soils at the National Geotechnical Experimentation Site, Opelika, Alabama." *Geotechnical Special Publication No. 93 - National Geotechnical Experimentation Sites*, ASCE, Reston, VA, 160-185.
- Mayne, P.W. and Brown, D.A. (2003). "Site characterization of Piedmont residuum of North America". *Characterization and Engineering Properties of Natural Soils*, Vol. 2, Swets & Zeitlinger, Lisse, 1323-1339.
- McGillivray, A. V. (2007). *Enhanced integration of shear wave velocity profiling in direct-push site characterization systems*. Ph.D. Dissertation, Georgia Institute of Technology, Atlanta, GA.
- Montgomery, J., Shi, C., and Anderson, J. B. (2018). "An updated database for the Spring Villa National Geotechnical Experimentation Site." *International Foundations Congress and Equipment Expo*, ASCE, Orlando, FL.
- Mullins, G. and Ashmawy, A., (2005). *Factors affecting anomaly formation in drilled shafts - Final Report*. University of South Florida, Tampa, FL.
- NCAT (2009). "Index of images: Track Aerials." National Center for Asphalt Technology at Auburn University.
<<http://www.pavetrack.com/images/photo%20album/2009/Track%20Aerials/>> (March 9, 2018)
- Simpson, M., and Brown, D. A. (2003). *Development of P-Y curves for Piedmont residual soils*. Auburn University Highway Research Center, Auburn, Alabama.
- Sowers, G. F., and Richardson, T. L. (1983). "Residual soils of piedmont and Blue Ridge." *Transportation Research Record*, Transportation Research Board, 919, 10-16.
- Vinson, J. L., and Brown, D. A. (1997). *Site characterization of the Spring Villa geotechnical test site and a comparison of strength and stiffness parameters for a Piedmont residual soil*. Auburn University Highway Research Center, Auburn, Alabama.
- Warwick, C. (2003). *SystemC calls MATLAB*. MATLAB Central, March.
- Wang, H., Wang, C. Y., Wu, H. J., and Vinh, N. T. (2017). "Ultra-Seismic Depth Evaluation on Model Piles-A Pilot Experiment." 15th Asia Pacific Conference for Non-Destructive Testing (APCND 2017), Singapore.

APPENDIX A: ACCELERATION TIME HISTRIES FOR THE NUMERICAL SIMULATIONS

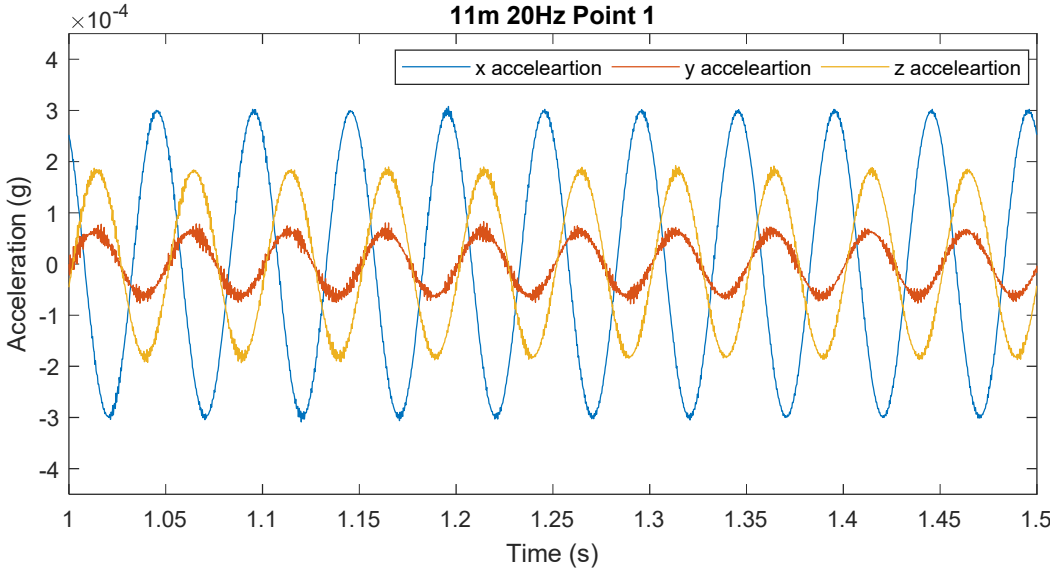


Figure A-1: Time history for 20 Hz at Point 1 of 11-meter shaft length simulation

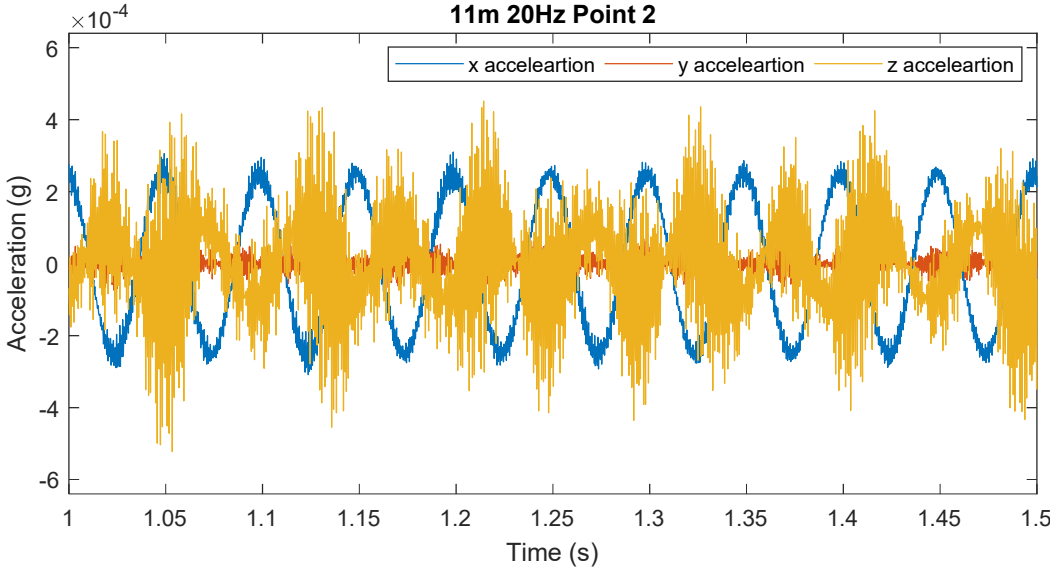


Figure A-2: Time history for 20 Hz at Point 2 of 11-meter shaft length simulation

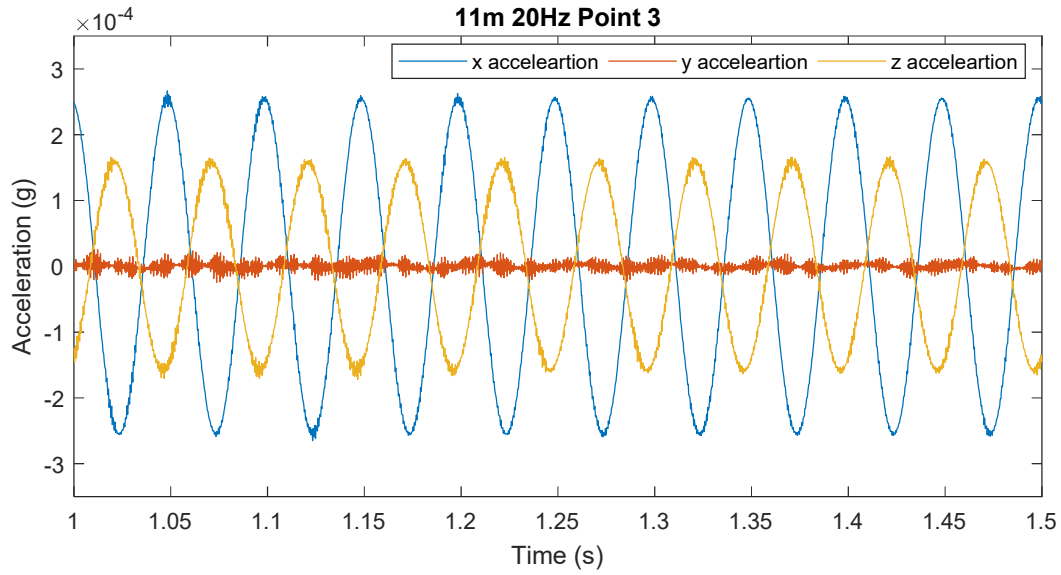


Figure A-3: Time history for 20 Hz at Point 3 of 11-meter shaft length simulation

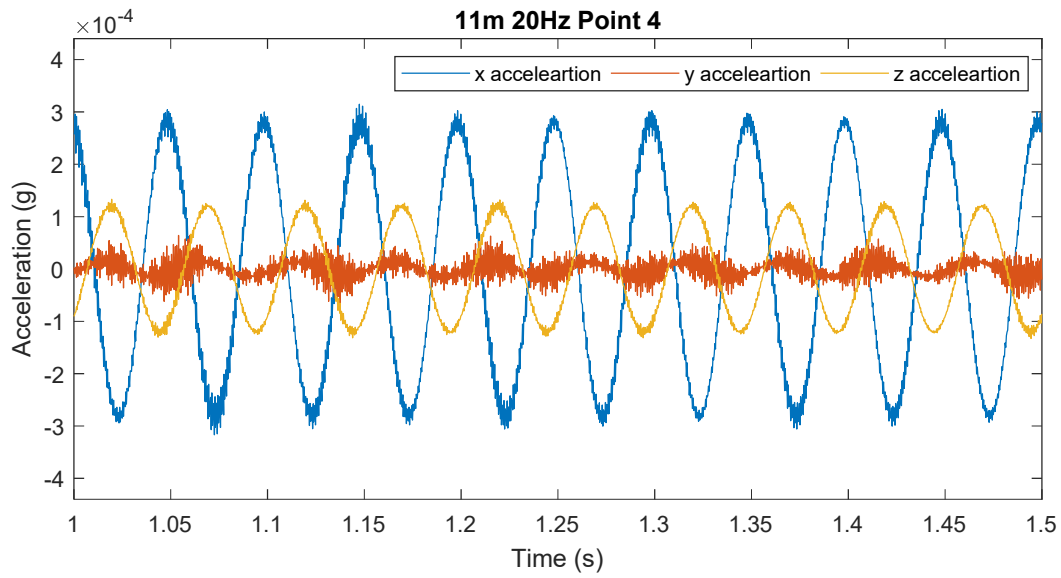


Figure A-4: Time history for 20 Hz at Point 4 of 11-meter shaft length simulation

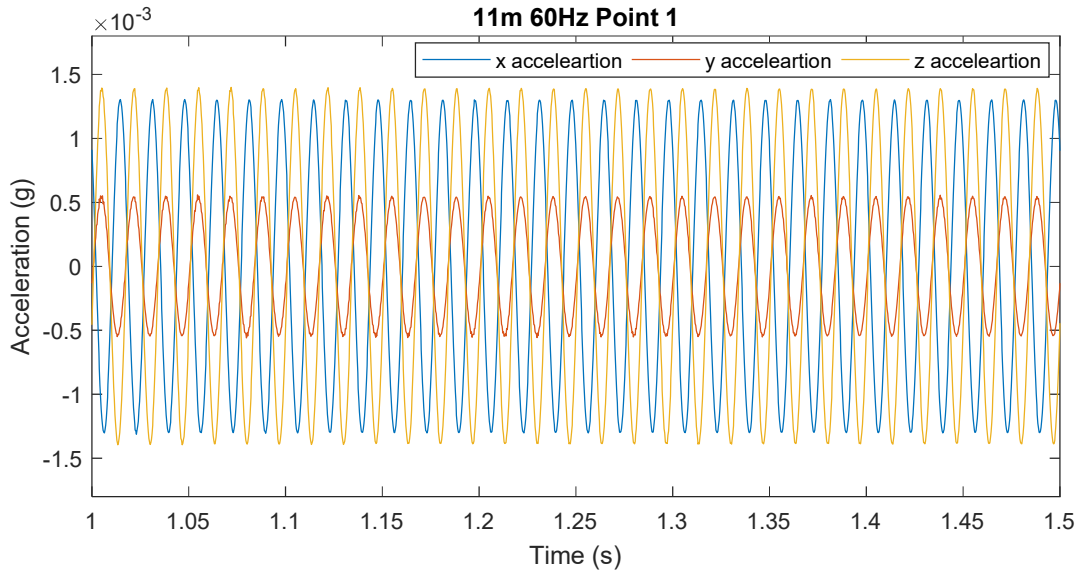


Figure A-5: Time history for 60 Hz at Point 1 of 11-meter shaft length simulation

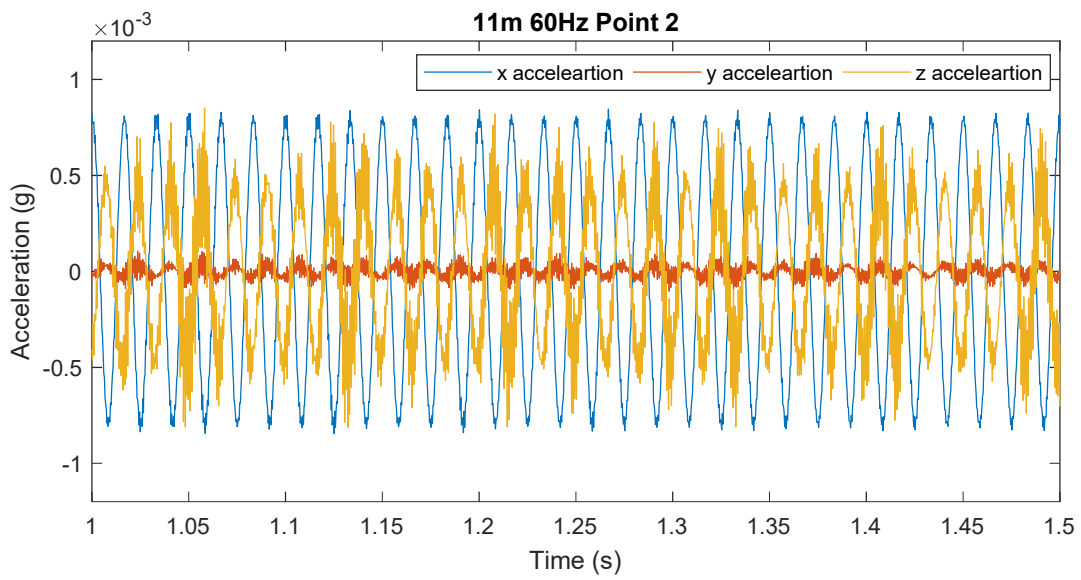


Figure A-6: Time history for 60 Hz at Point 2 of 11-meter shaft length simulation

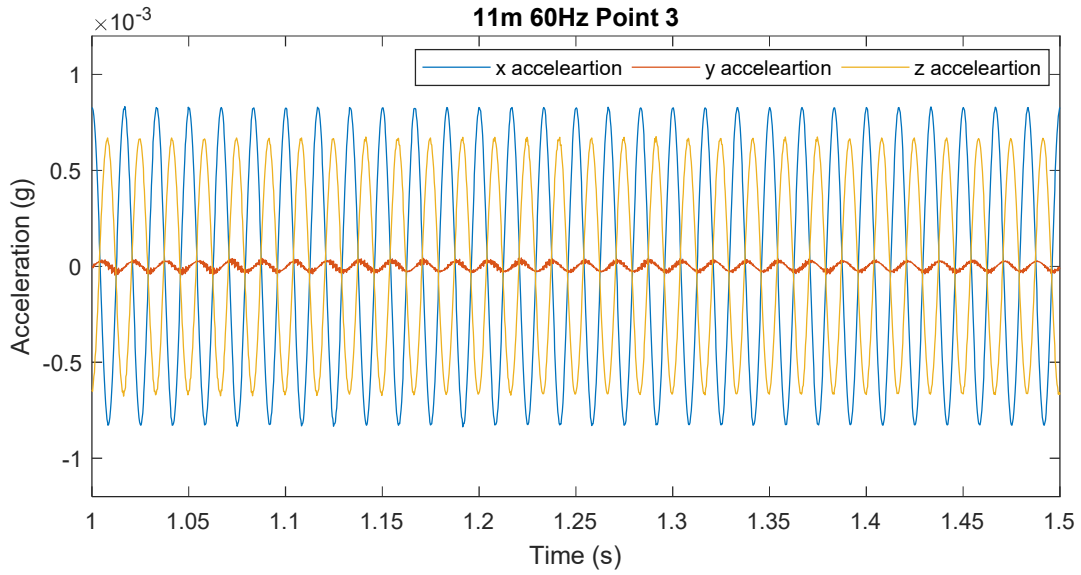


Figure A-7: Time history for 60 Hz at Point 3 of 11-meter shaft length simulation

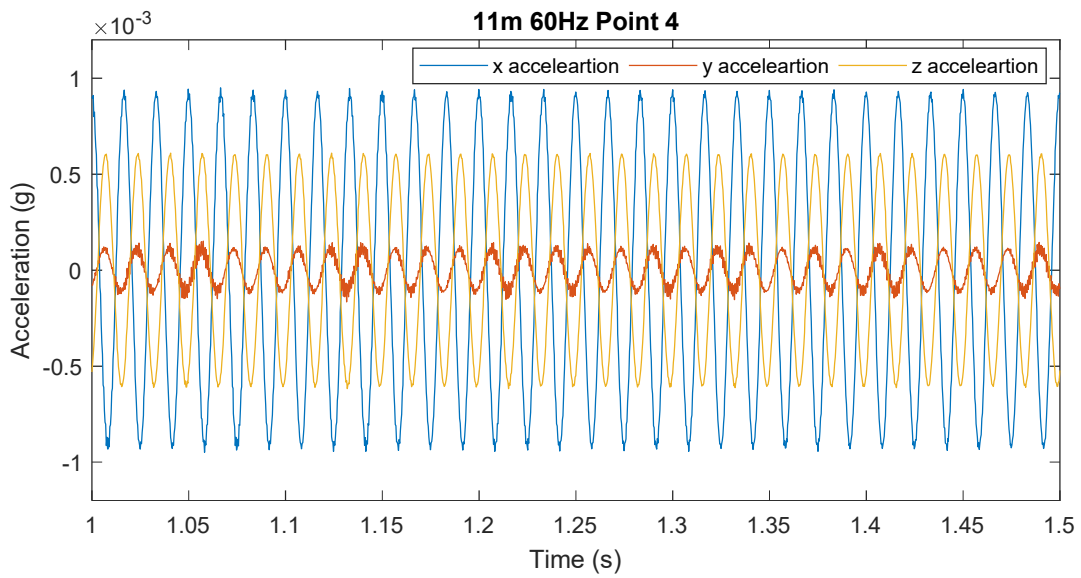


Figure A-8: Time history for 60 Hz at Point 4 of 11-meter shaft length simulation

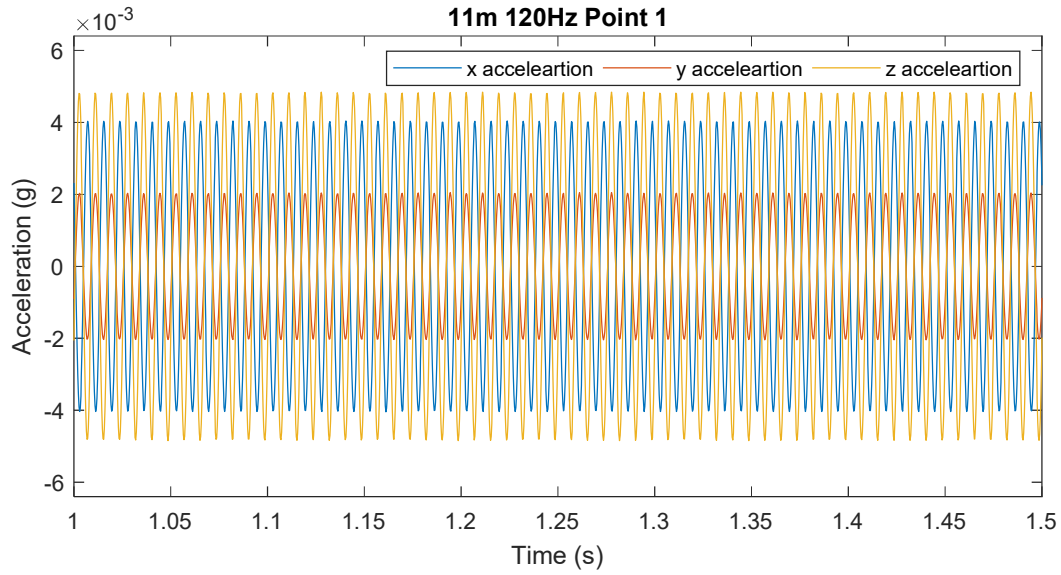


Figure A-9: Time history for 120 Hz at Point 1 of 11-meter shaft length simulation

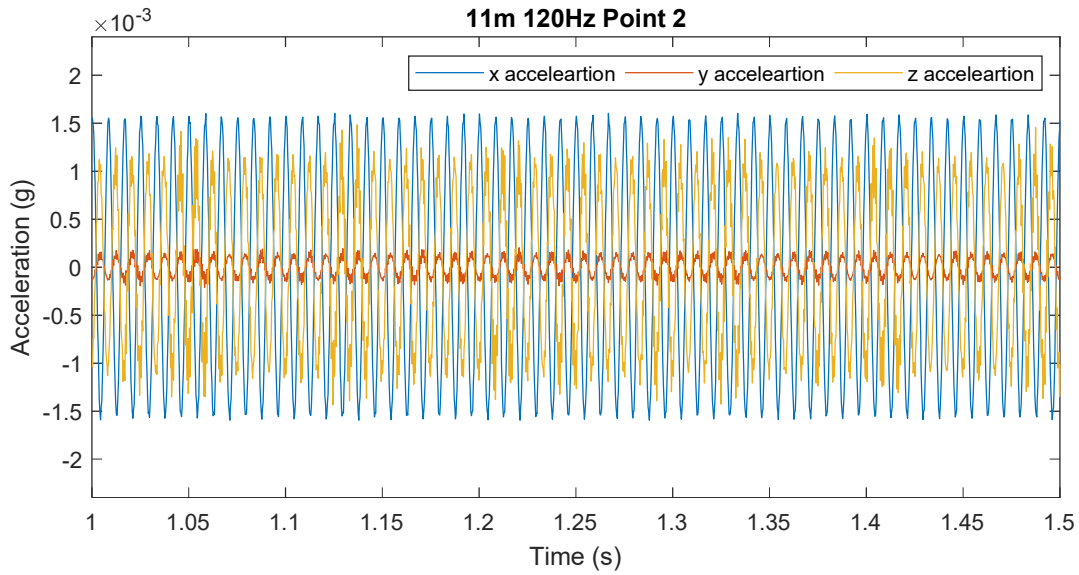


Figure A-10: Time history for 120 Hz at Point 2 of 11-meter shaft length simulation

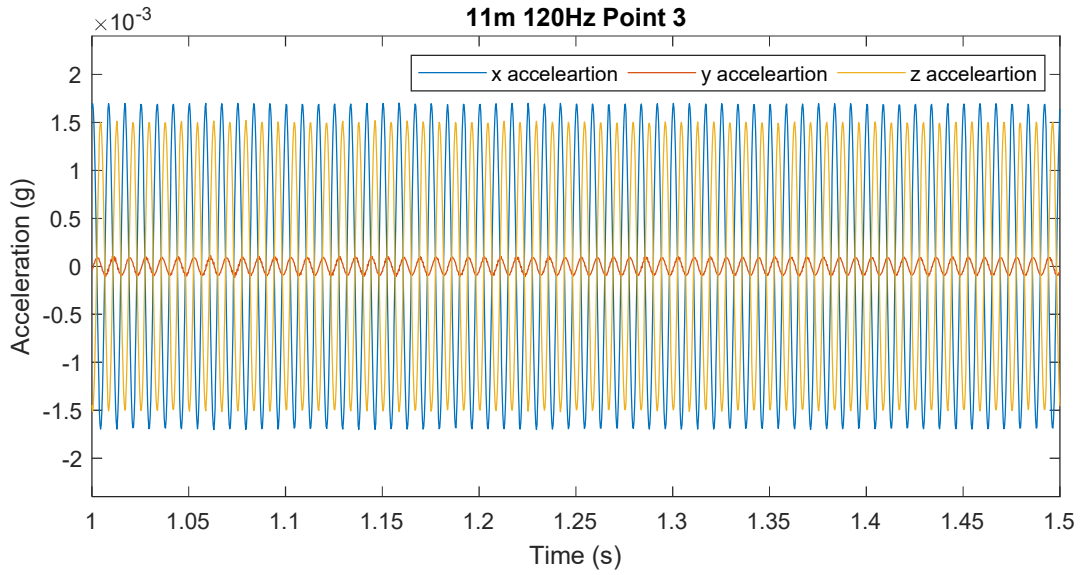


Figure A-11: Time history for 120 Hz at Point 3 of 11-meter shaft length simulation

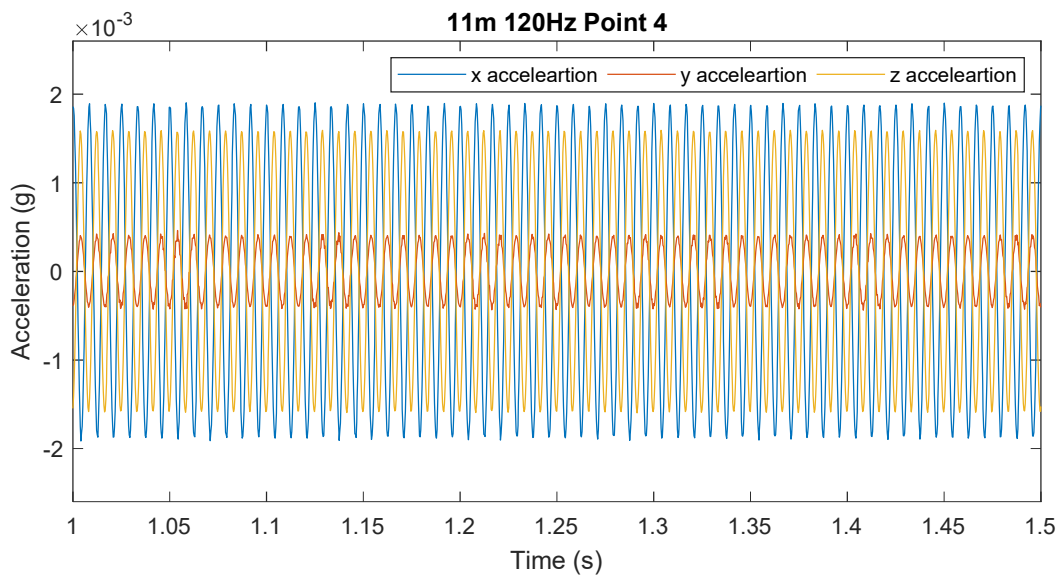


Figure A-12: Time history for 120 Hz at Point 4 of 11-meter shaft length simulation

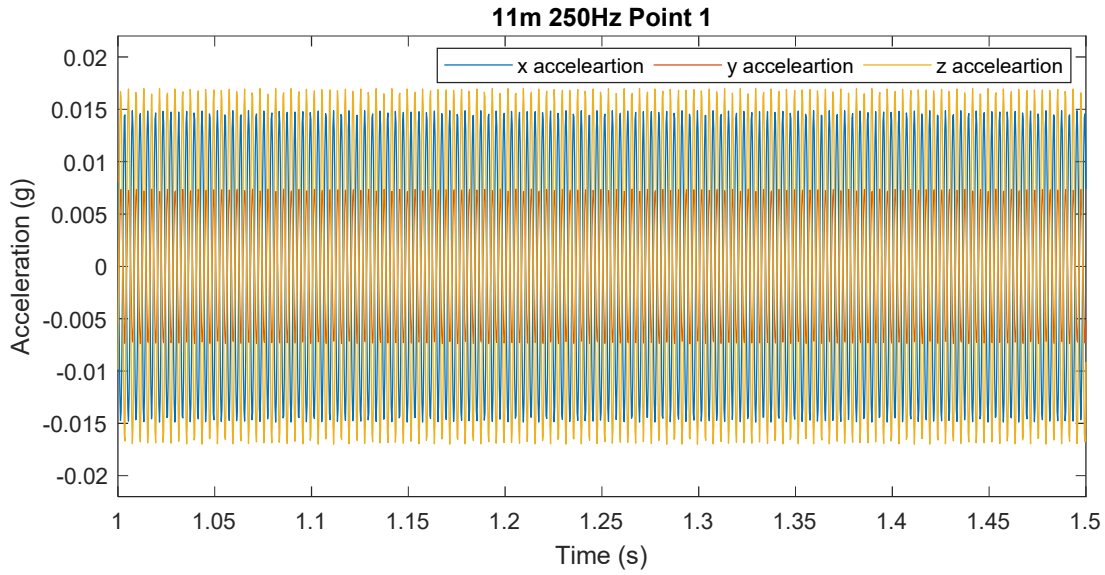


Figure A-13: Time history for 250 Hz at Point 1 of 11-meter shaft length simulation

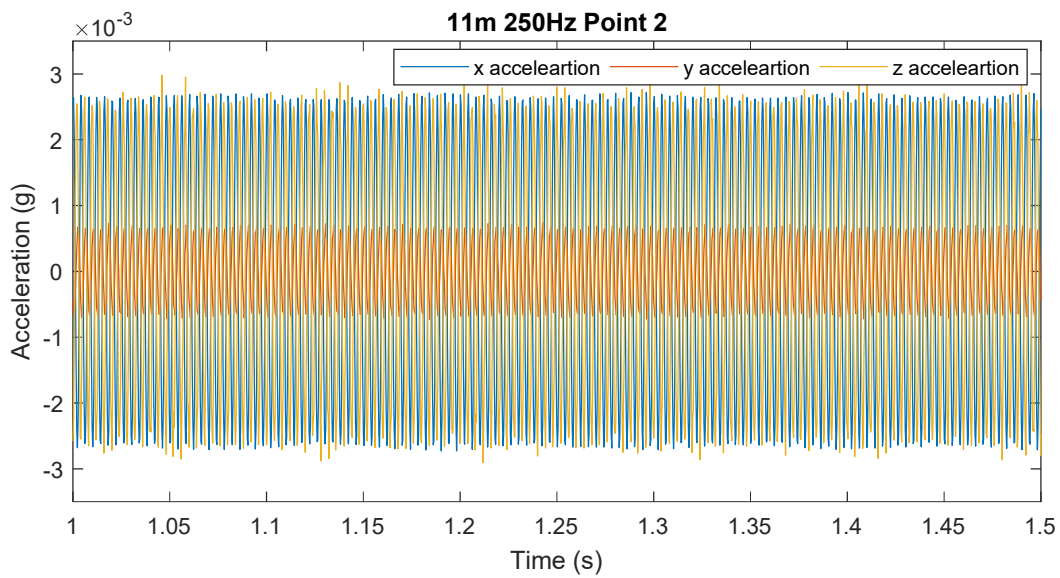


Figure A-14: Time history for 250 Hz at Point 2 of 11-meter shaft length simulation

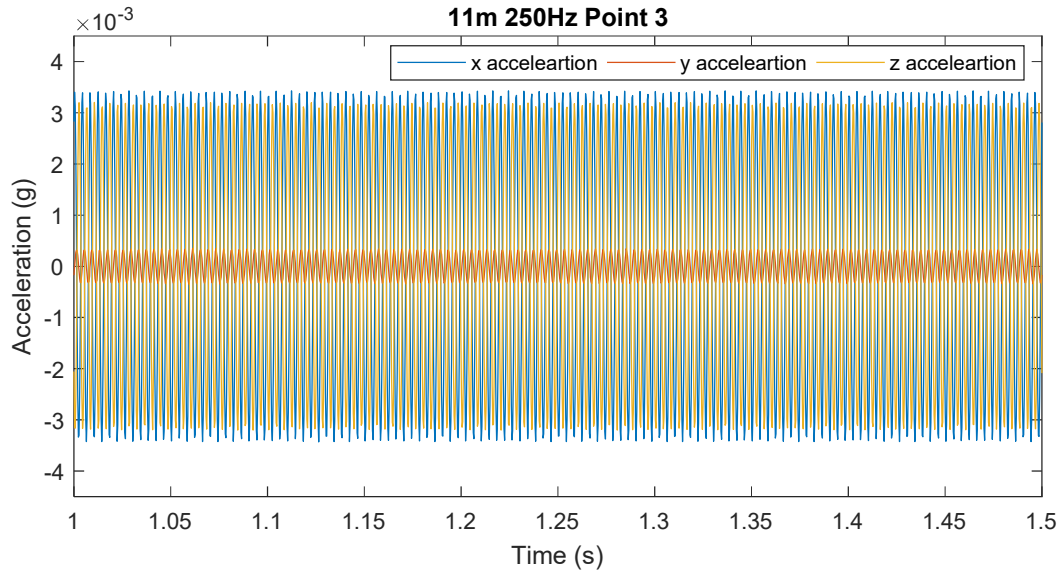


Figure A-15: Time history for 250 Hz at Point 3 of 11-meter shaft length simulation

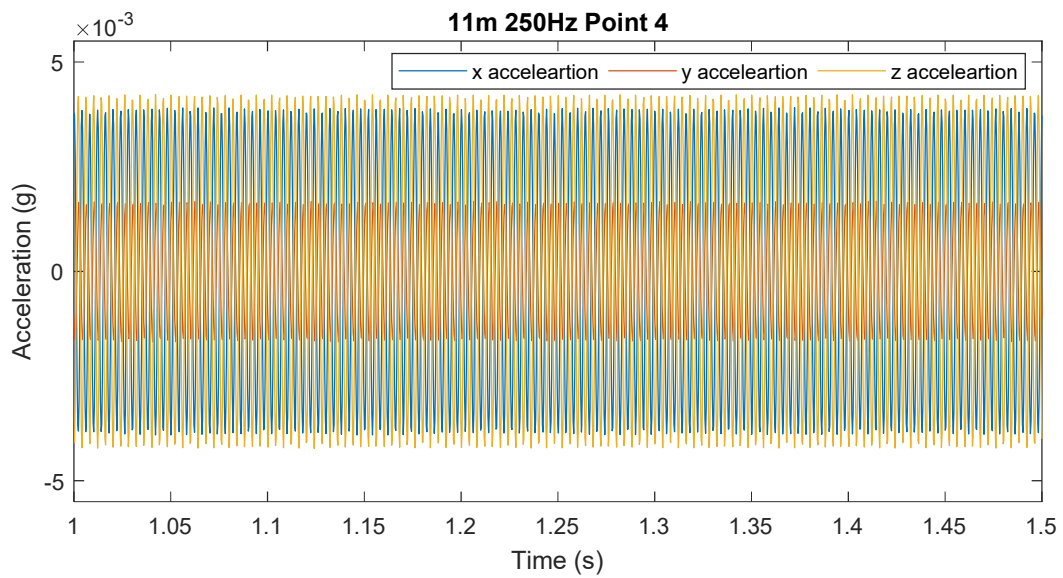


Figure A-16: Time history for 250 Hz at Point 4 of 11-meter shaft length simulation

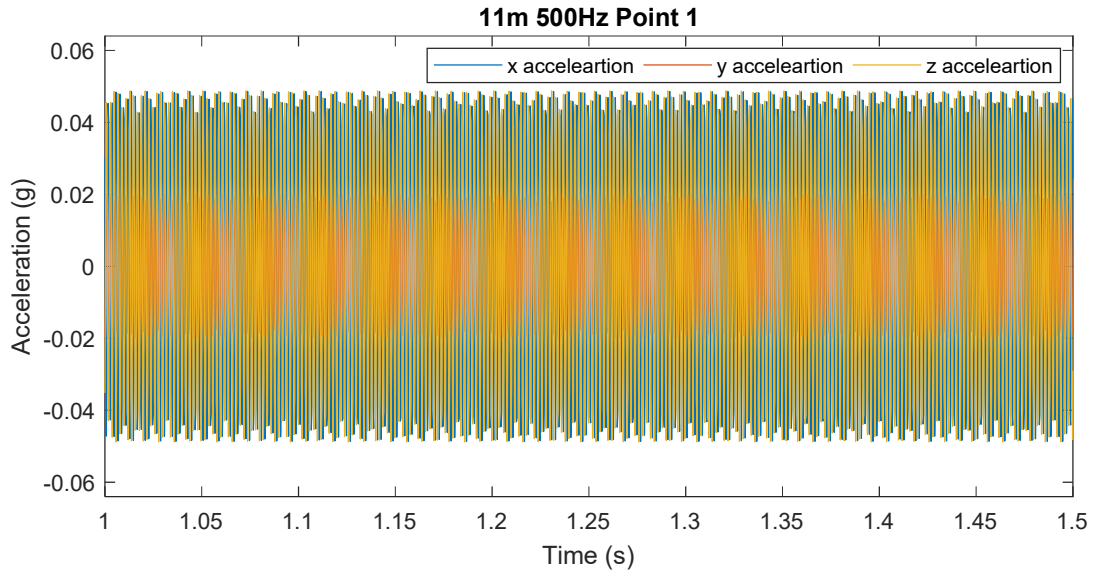


Figure A-17: Time history for 500 Hz at Point 1 of 11-meter shaft length simulation

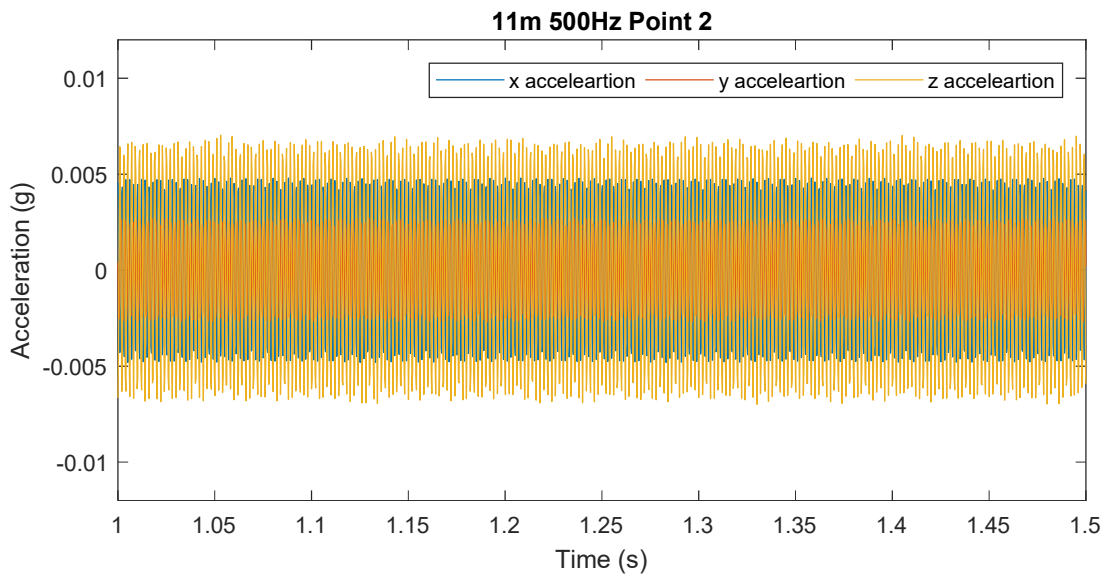


Figure A-18: Time history for 500 Hz at Point 2 of 11-meter shaft length simulation

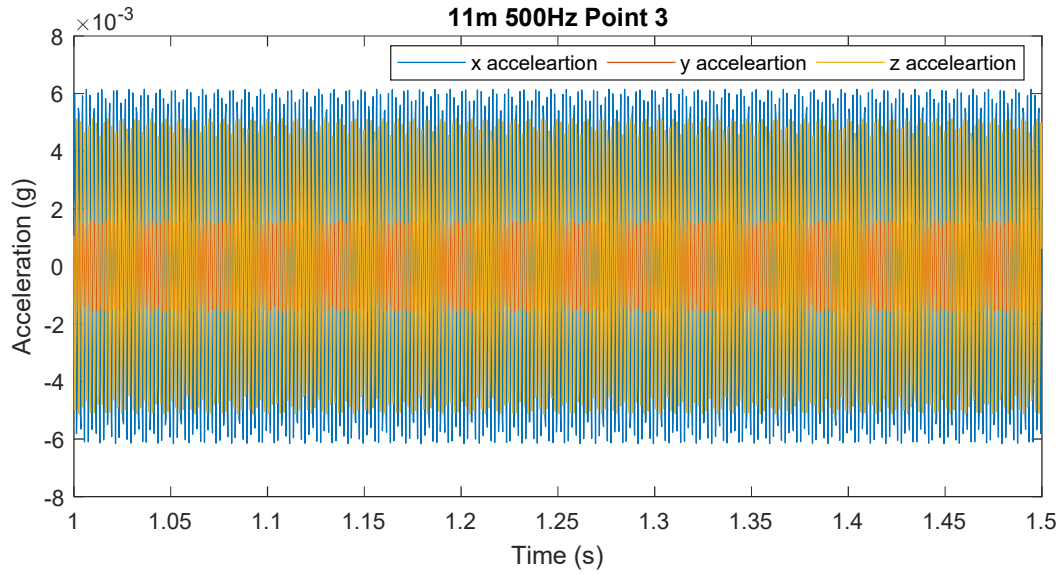


Figure A-19: Time history for 500 Hz at Point 3 of 11-meter shaft length simulation

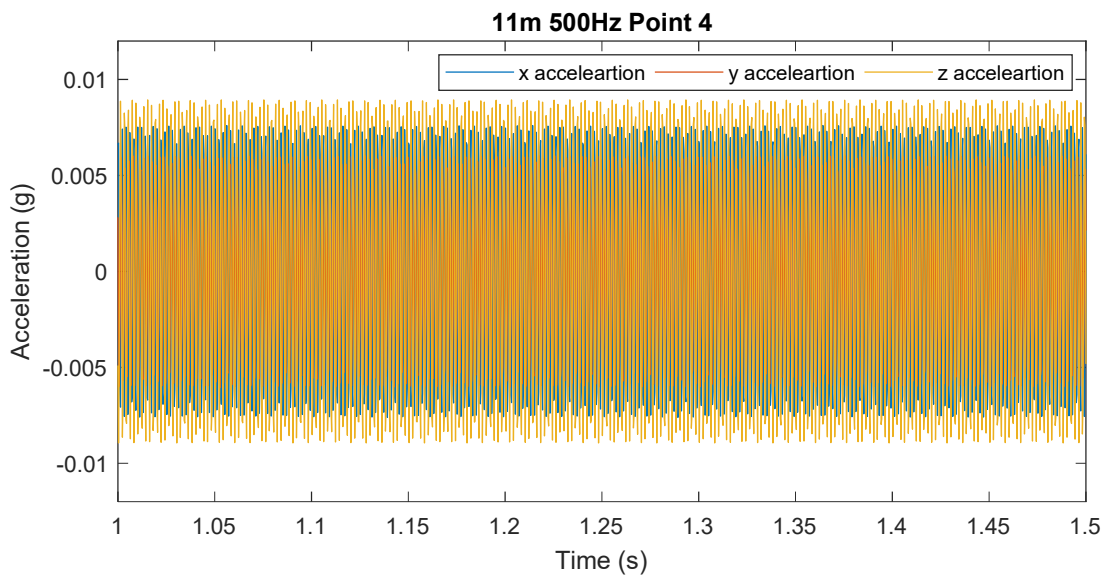


Figure A-20: Time history for 500 Hz at Point 4 of 11-meter shaft length simulation

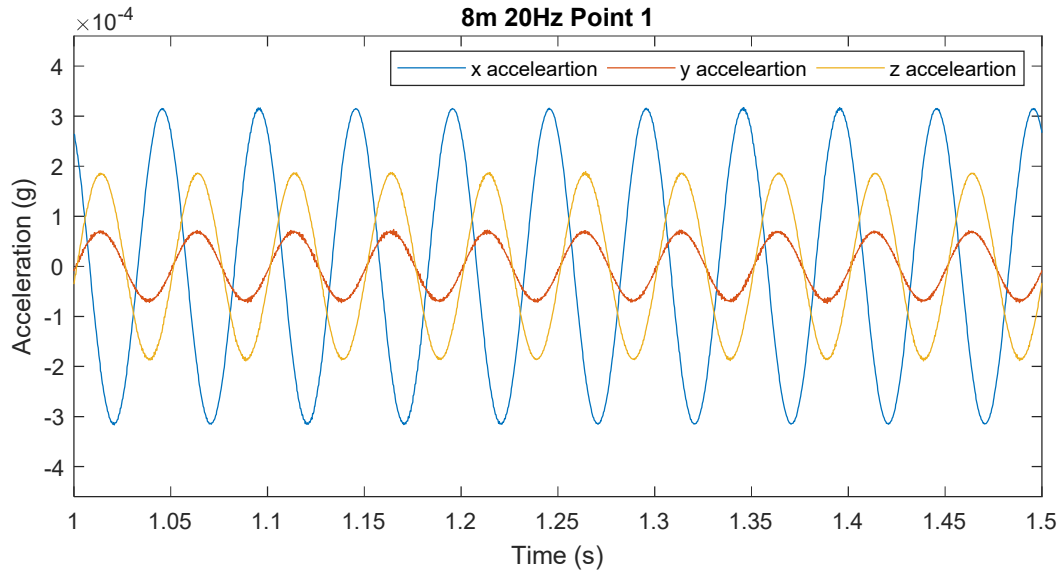


Figure A-21: Time history for 20 Hz at Point 1 of 8-meter shaft length simulation

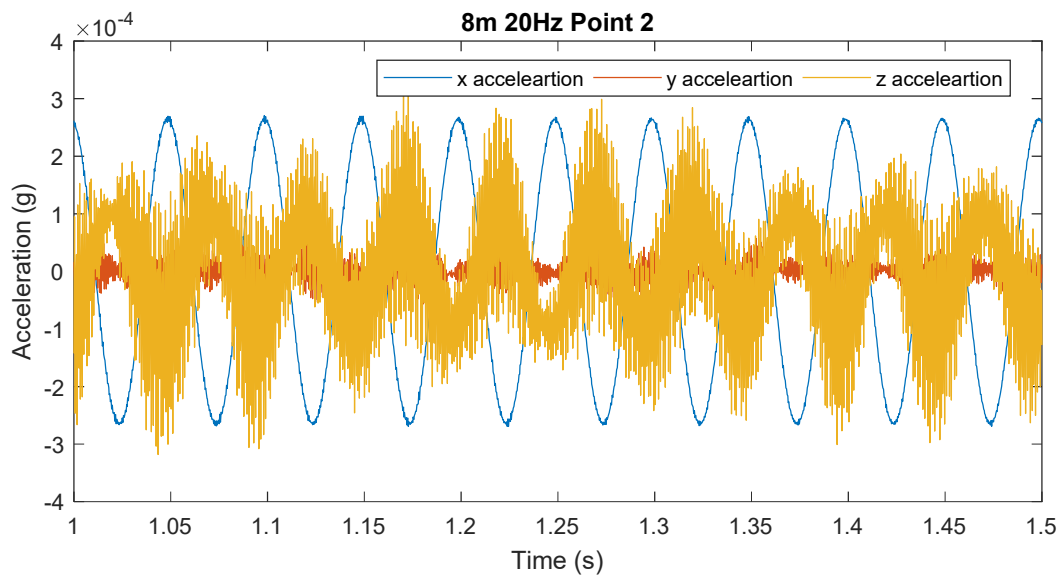


Figure A-22: Time history for 20 Hz at Point 2 of 8-meter shaft length simulation

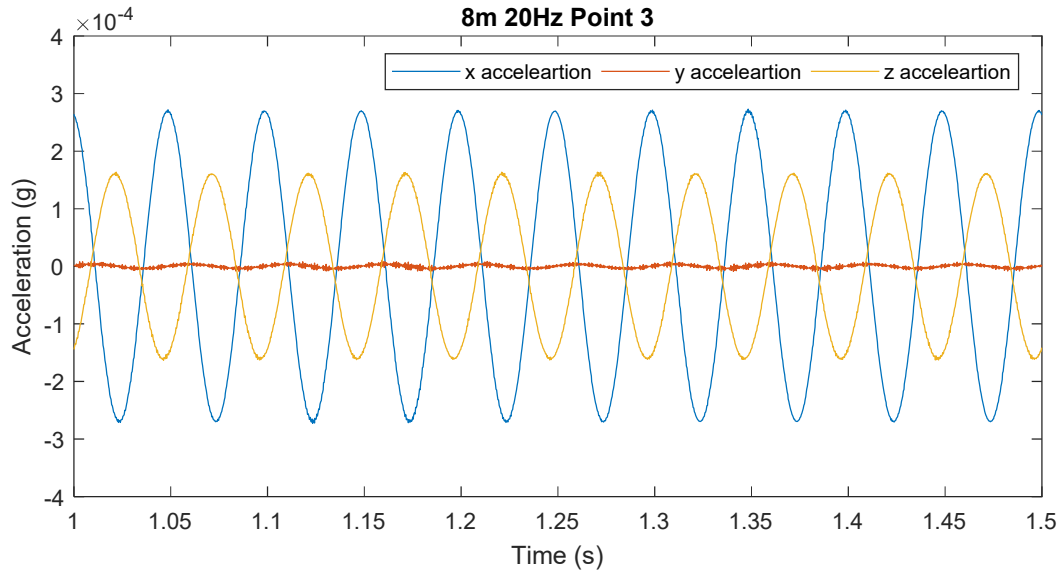


Figure A-23: Time history for 20 Hz at Point 3 of 8-meter shaft length simulation

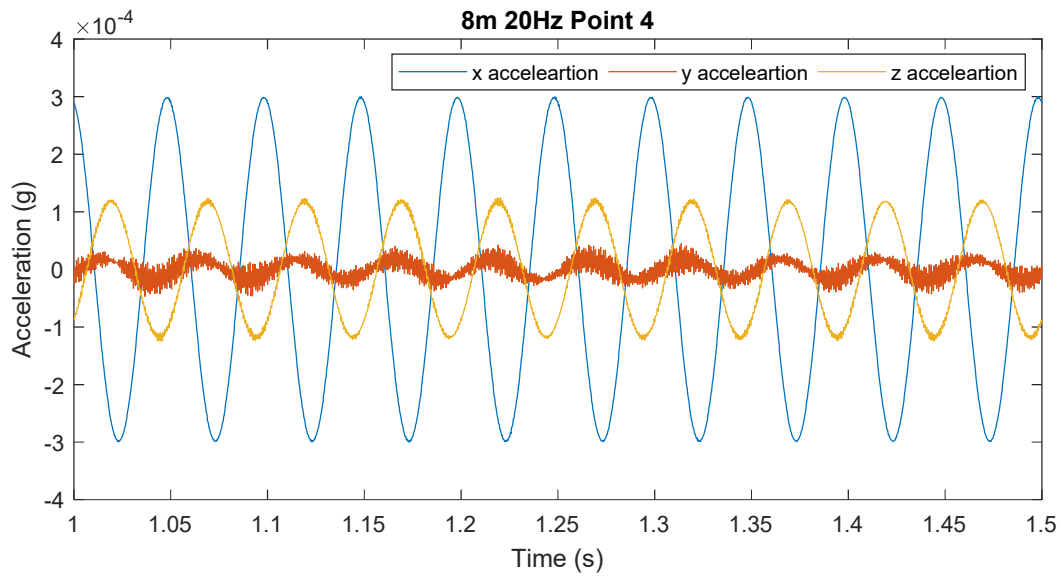


Figure A-24: Time history for 20 Hz at Point 4 of 8-meter shaft length simulation

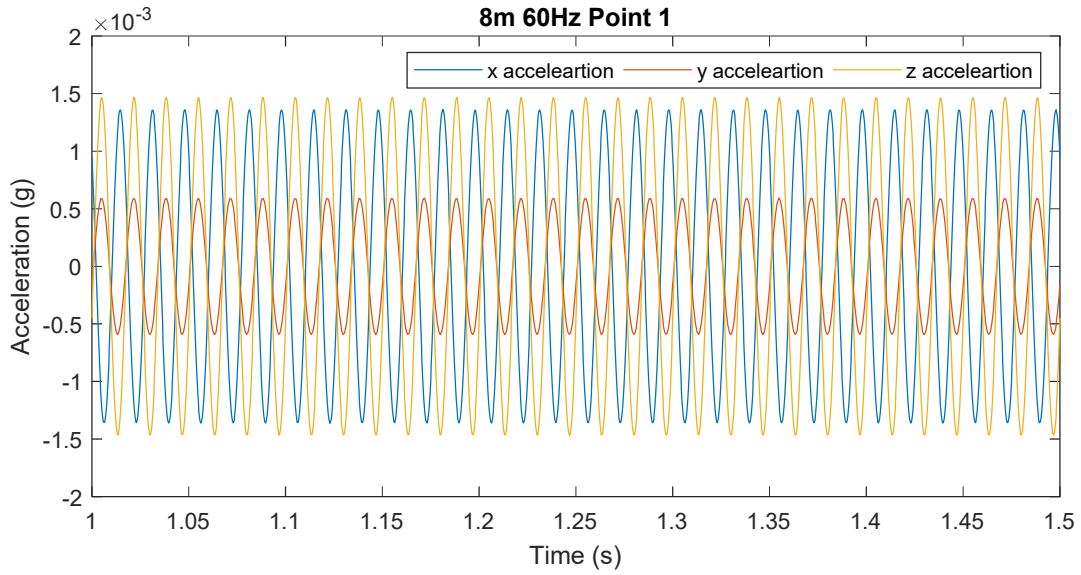


Figure A-25: Time history for 60 Hz at Point 1 of 8-meter shaft length simulation

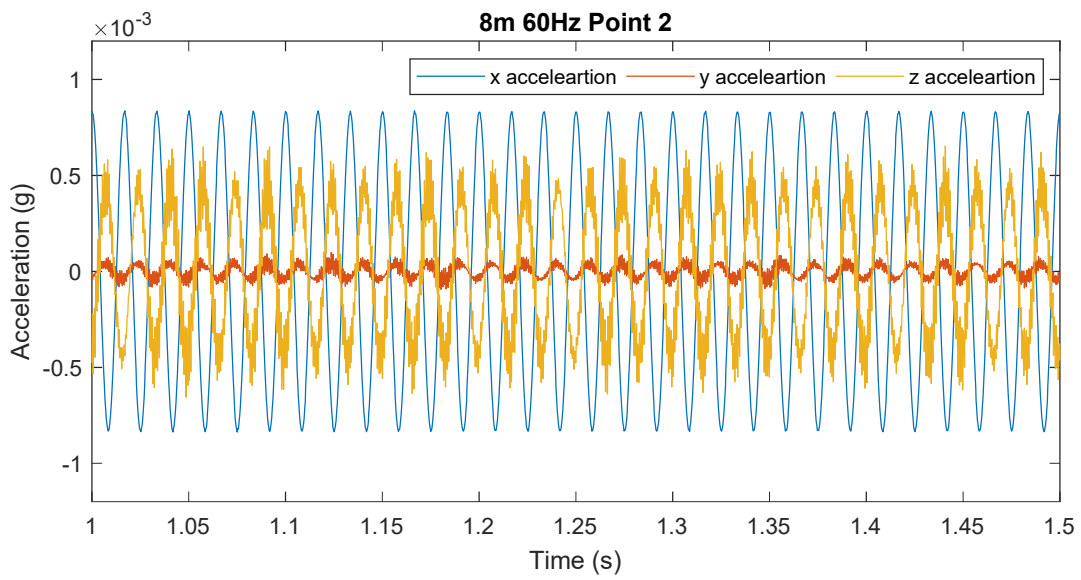


Figure A-26: Time history for 60 Hz at Point 2 of 8-meter shaft length simulation

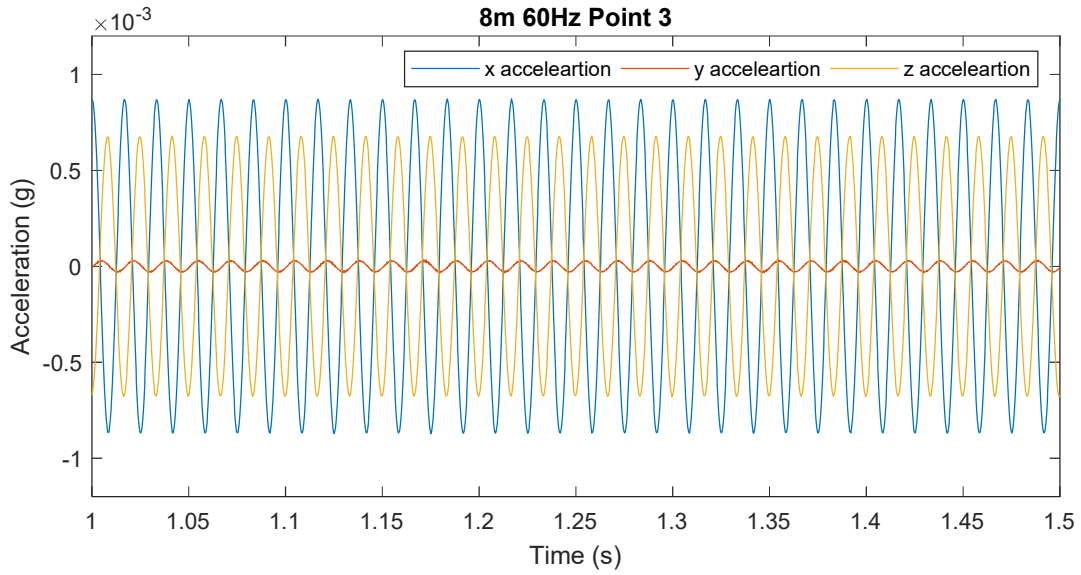


Figure A-27: Time history for 60 Hz at Point 3 of 8-meter shaft length simulation

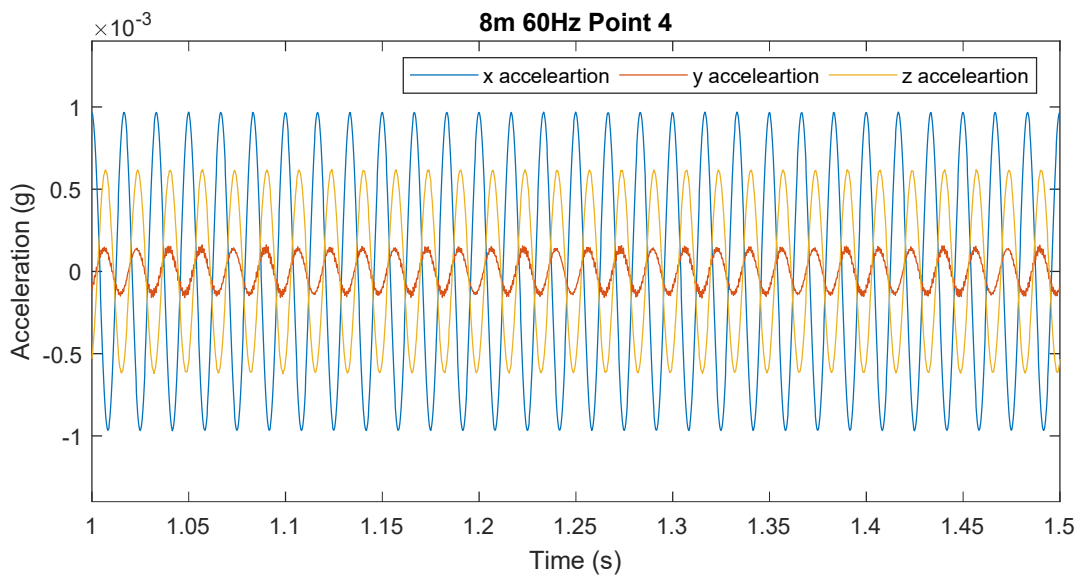


Figure A-28: Time history for 60 Hz at Point 4 of 8-meter shaft length simulation

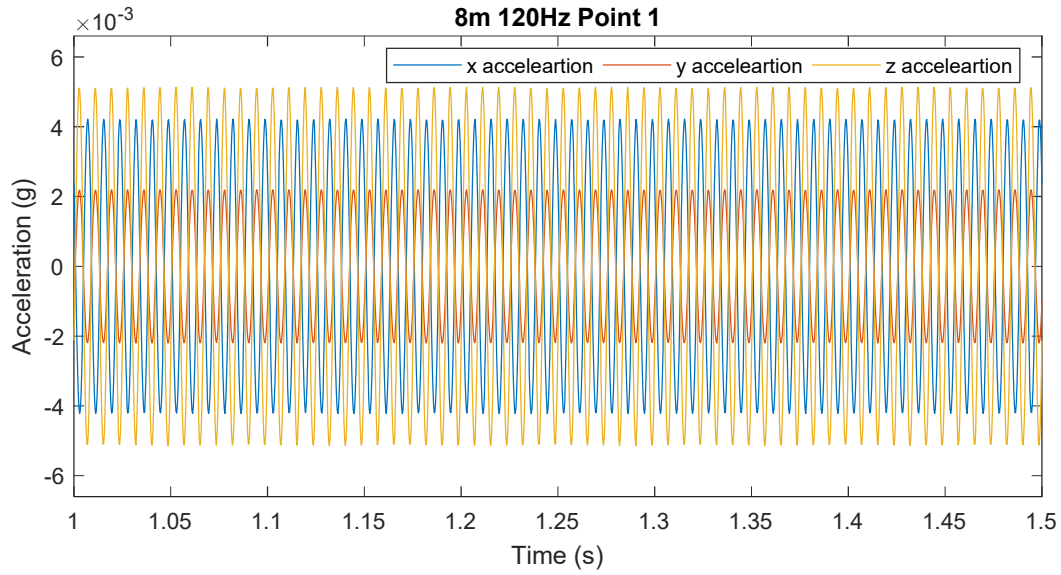


Figure A-29: Time history for 120 Hz at Point 1 of 8-meter shaft length simulation

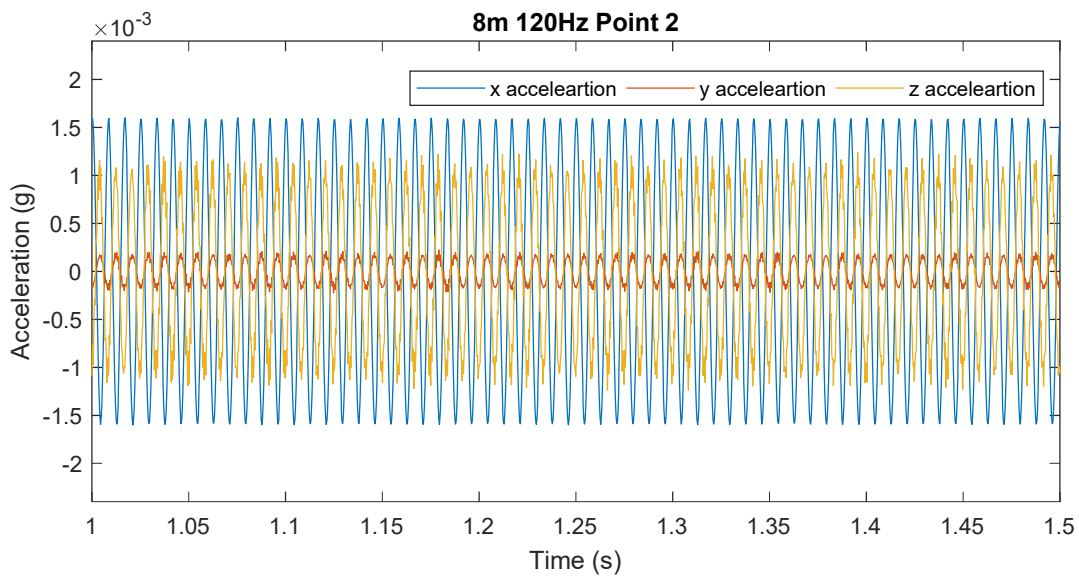


Figure A-30: Time history for 120 Hz at Point 2 of 8-meter shaft length simulation

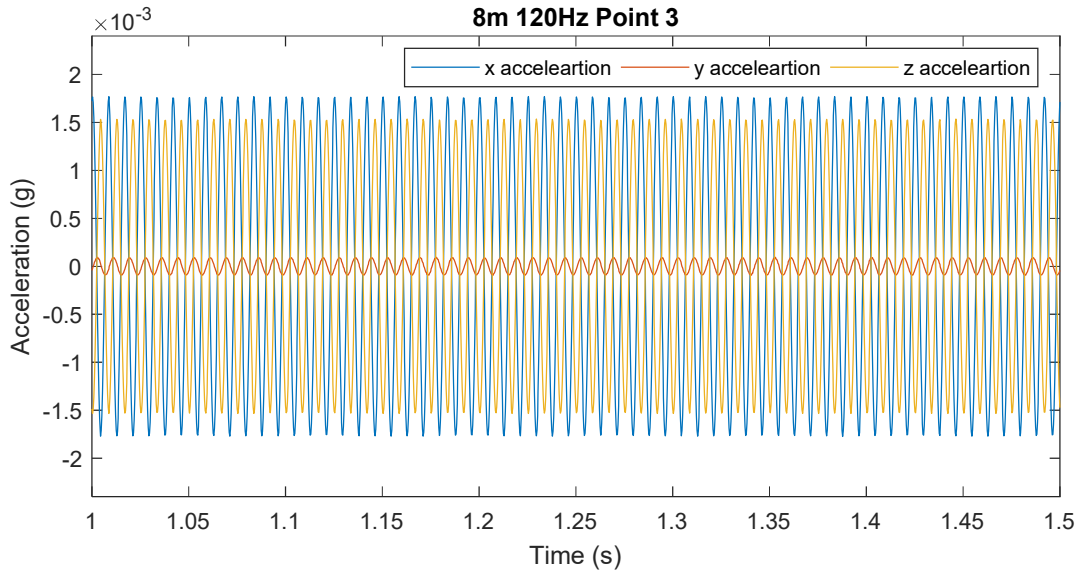


Figure A-31: Time history for 120 Hz at Point 3 of 8-meter shaft length simulation

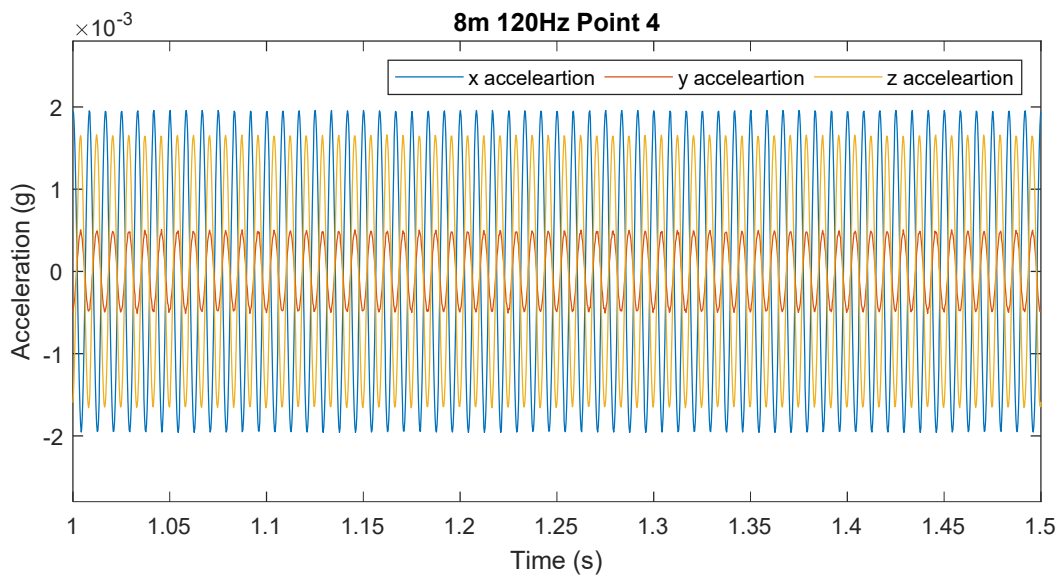


Figure A-32: Time history for 120 Hz at Point 4 of 8-meter shaft length simulation

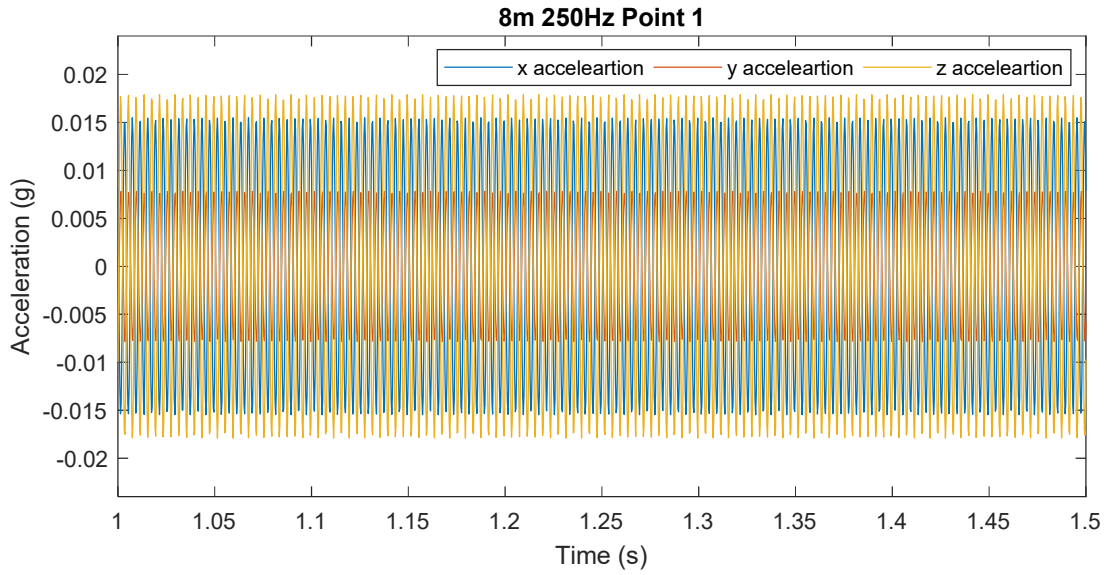


Figure A-33: Time history for 250 Hz at Point 1 of 8-meter shaft length simulation

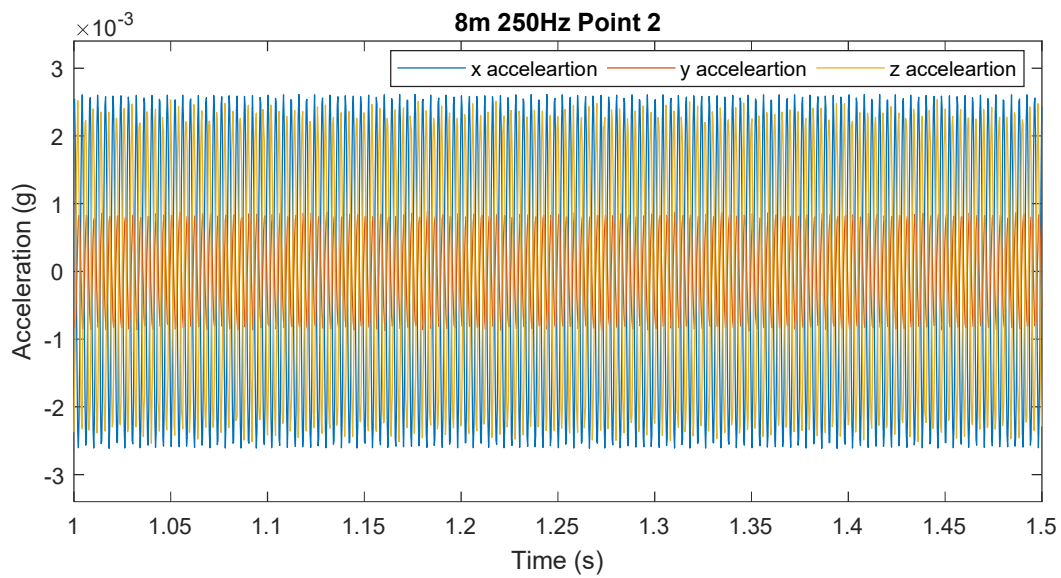


Figure A-34: Time history for 250 Hz at Point 2 of 8-meter shaft length simulation

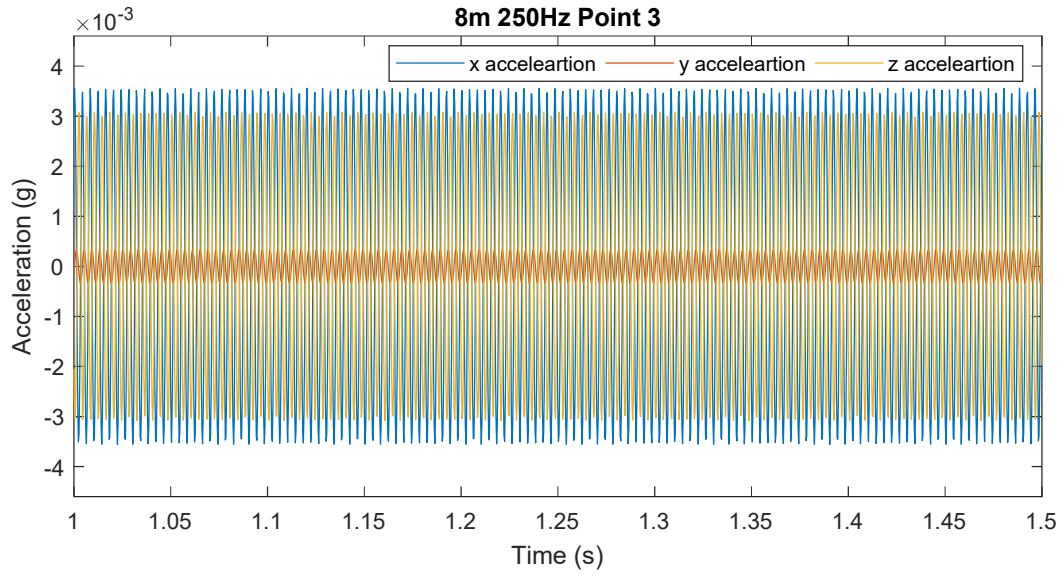


Figure A-35: Time history for 250 Hz at Point 3 of 8-meter shaft length simulation

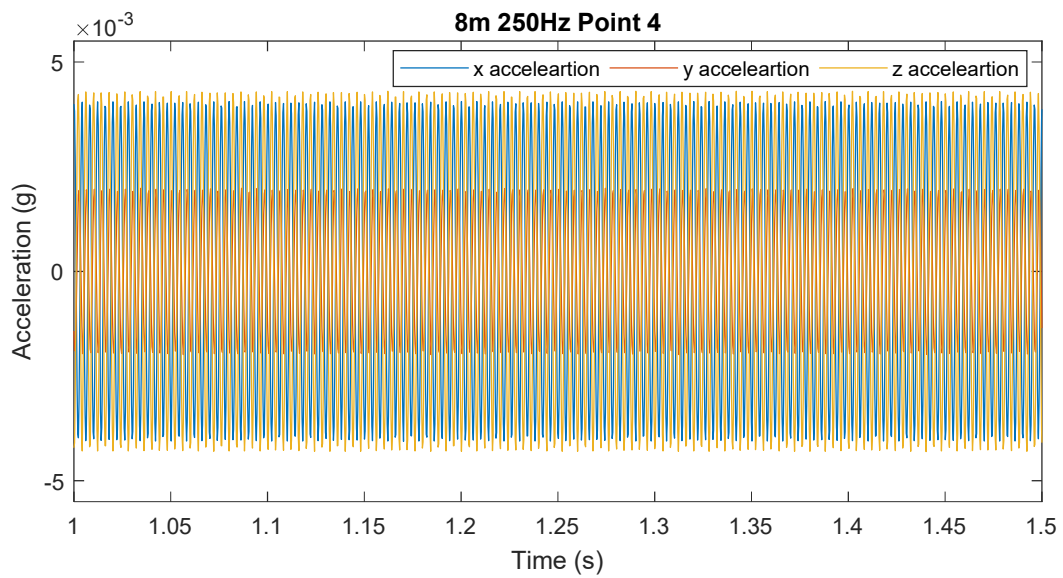


Figure A-36: Time history for 250 Hz at Point 4 of 8-meter shaft length simulation

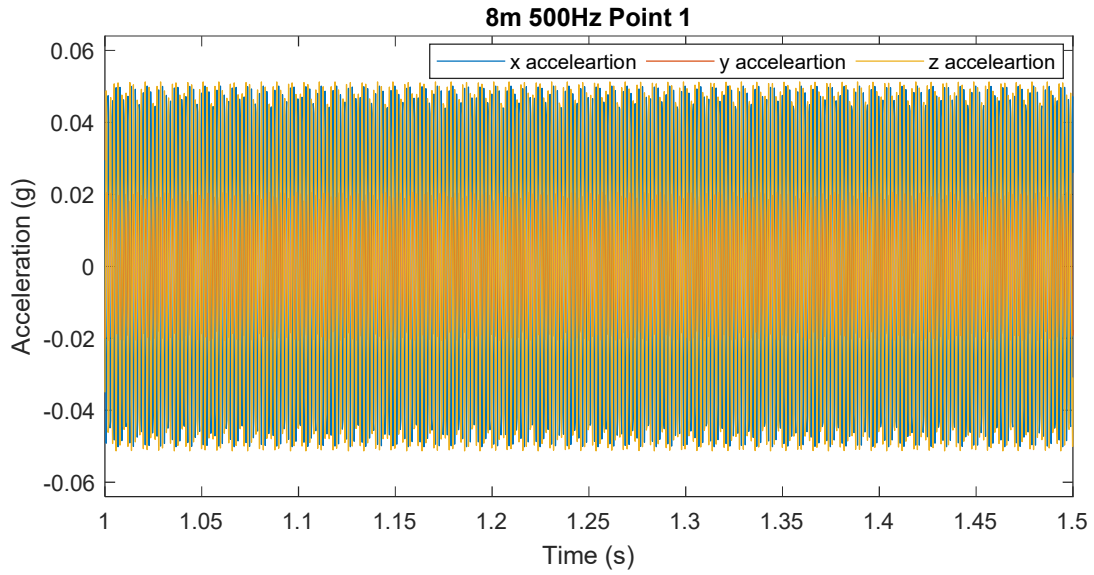


Figure A-37: Time history for 500 Hz at Point 1 of 8-meter shaft length simulation

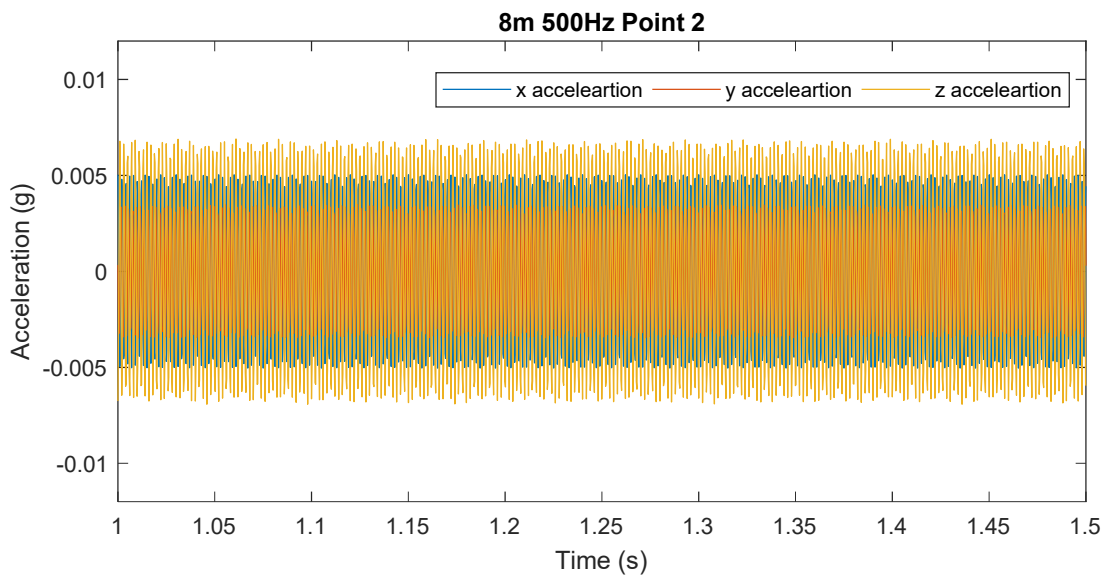


Figure A-38: Time history for 500 Hz at Point 2 of 8-meter shaft length simulation

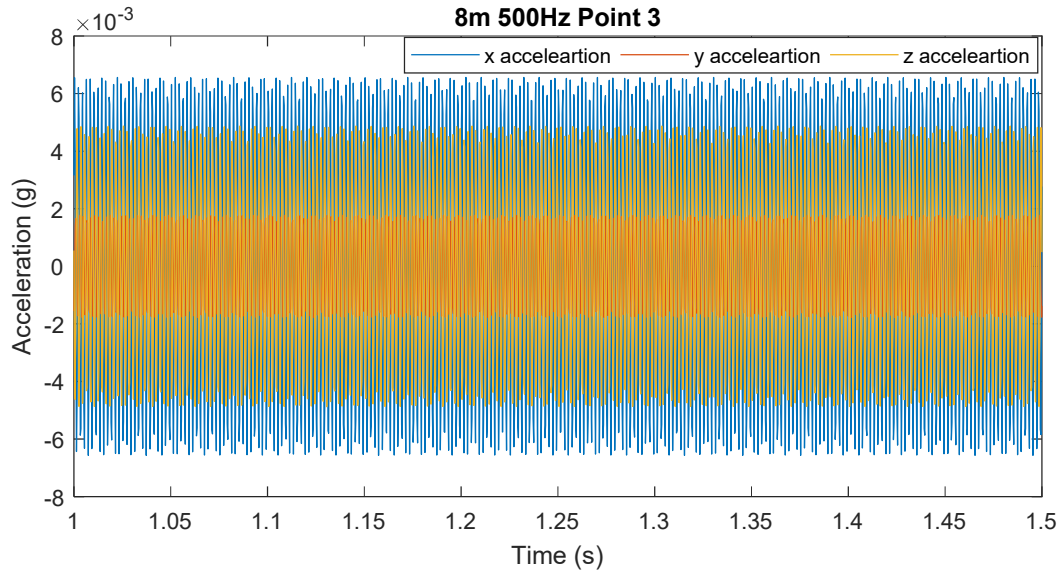


Figure A-39: Time history for 500 Hz at Point 3 of 8-meter shaft length simulation

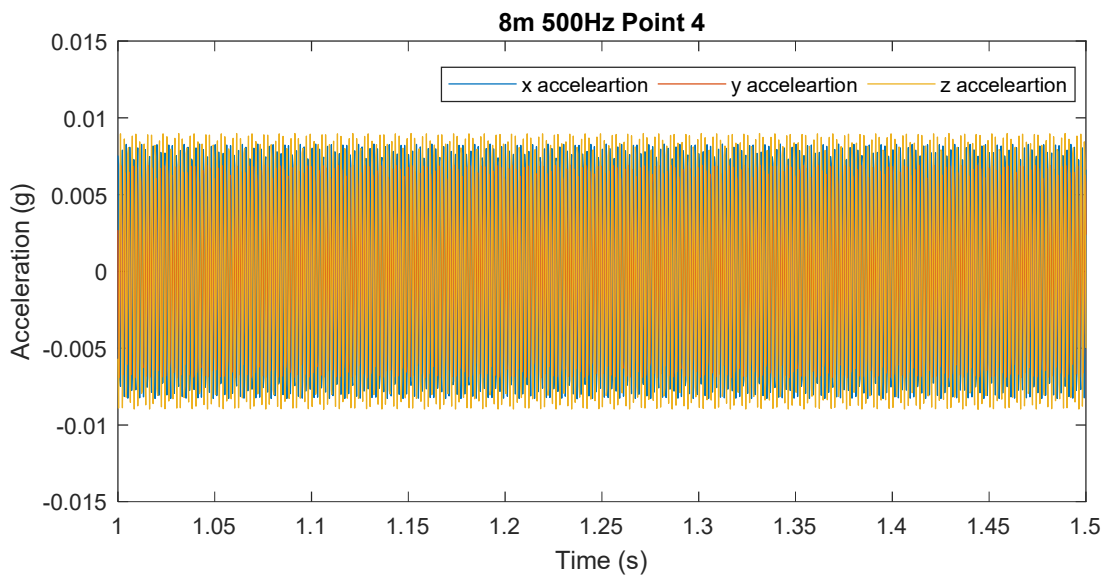


Figure A-40: Time history for 500 Hz at Point 4 of 8-meter shaft length simulation

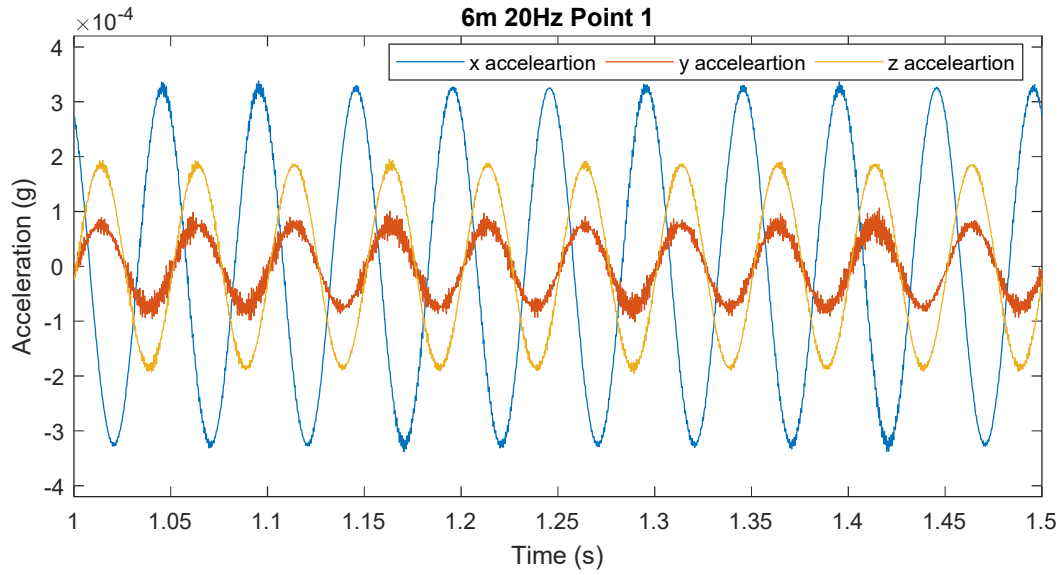


Figure A-41: Time history for 20 Hz at Point 1 of 6-meter shaft length simulation

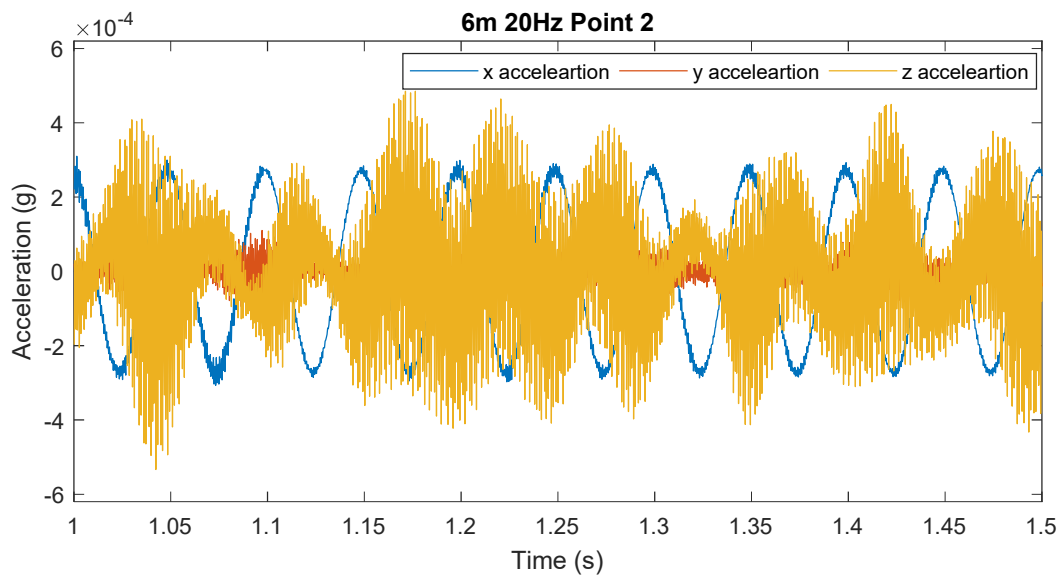


Figure A-42: Time history for 20 Hz at Point 2 of 6-meter shaft length simulation

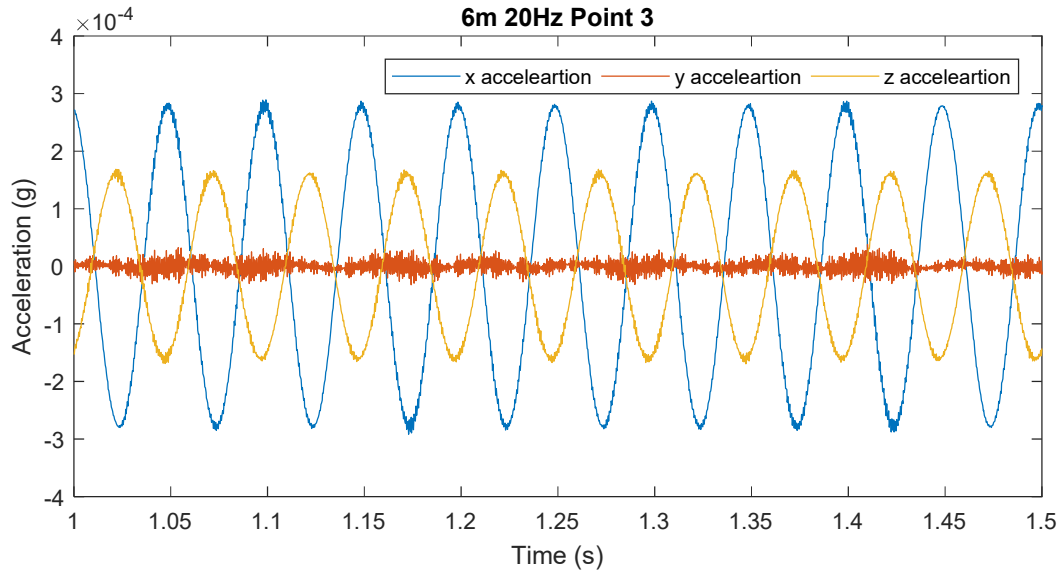


Figure A-43: Time history for 20 Hz at Point 3 of 6-meter shaft length simulation

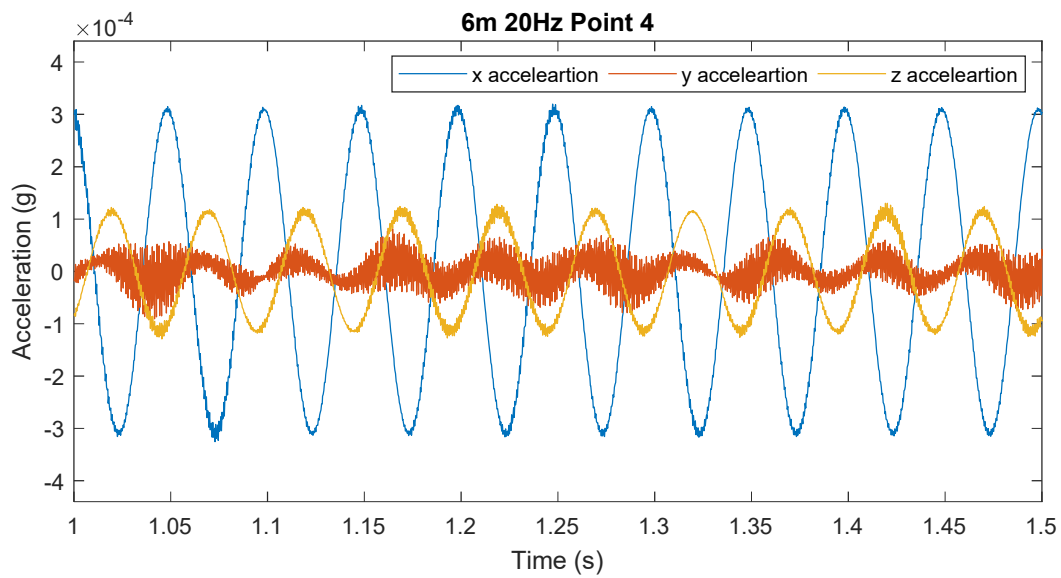


Figure A-44: Time history for 20 Hz at Point 4 of 6-meter shaft length simulation

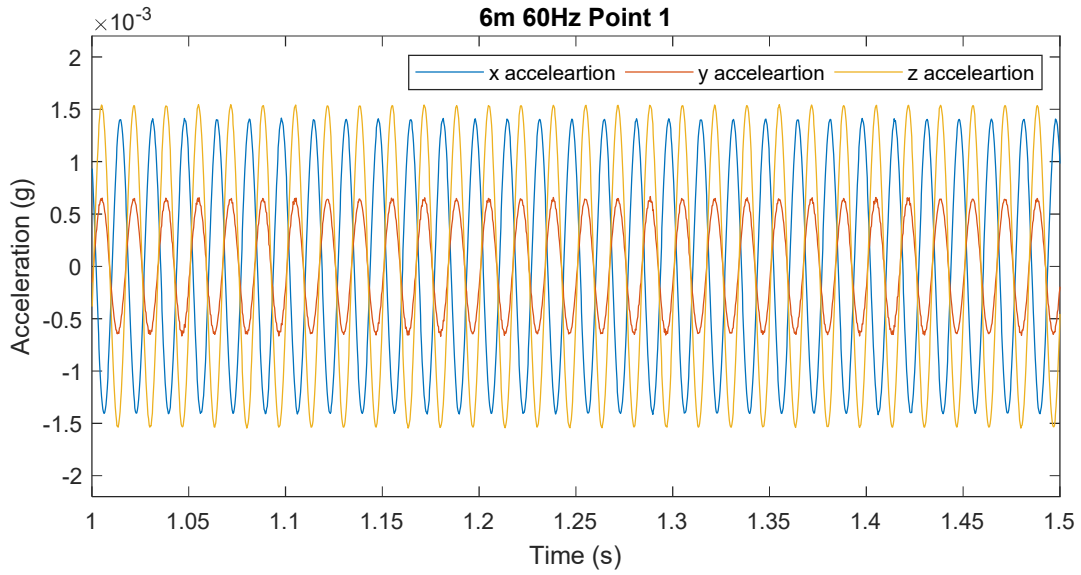


Figure A-45: Time history for 60 Hz at Point 1 of 6-meter shaft length simulation

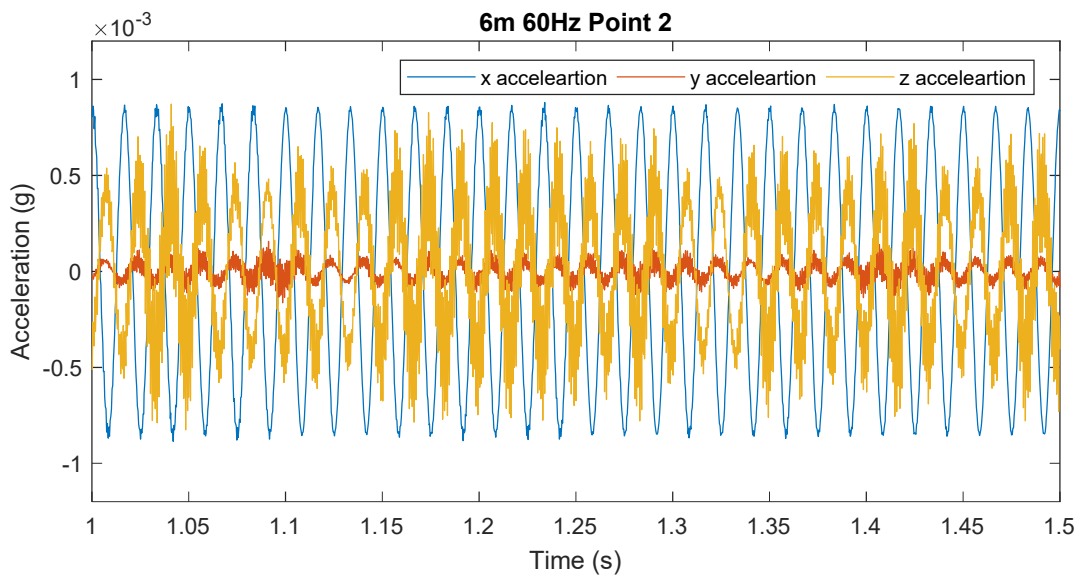


Figure A-46: Time history for 60 Hz at Point 2 of 6-meter shaft length simulation

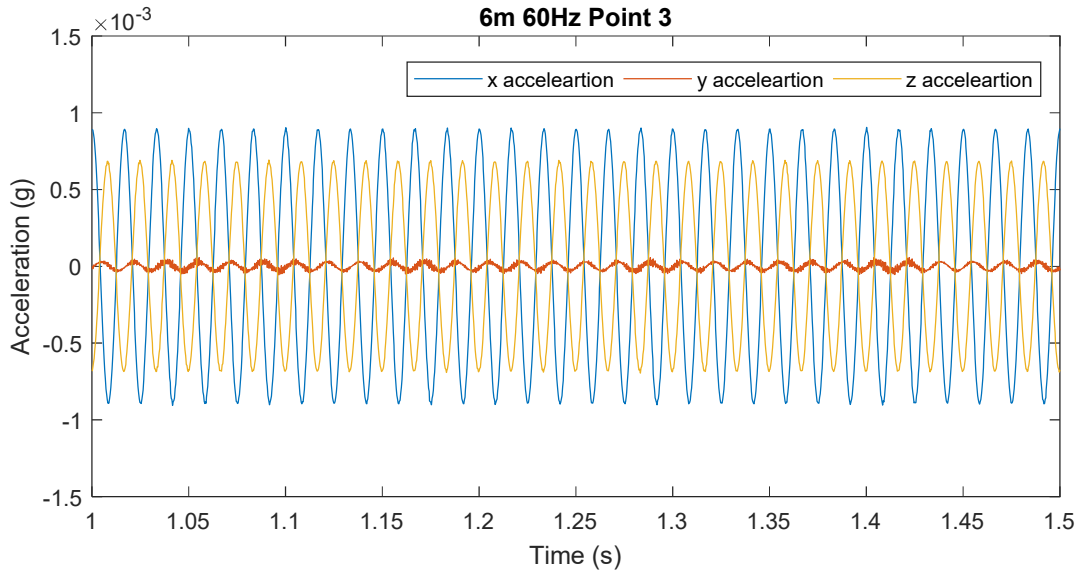


Figure A-47: Time history for 60 Hz at Point 3 of 6-meter shaft length simulation

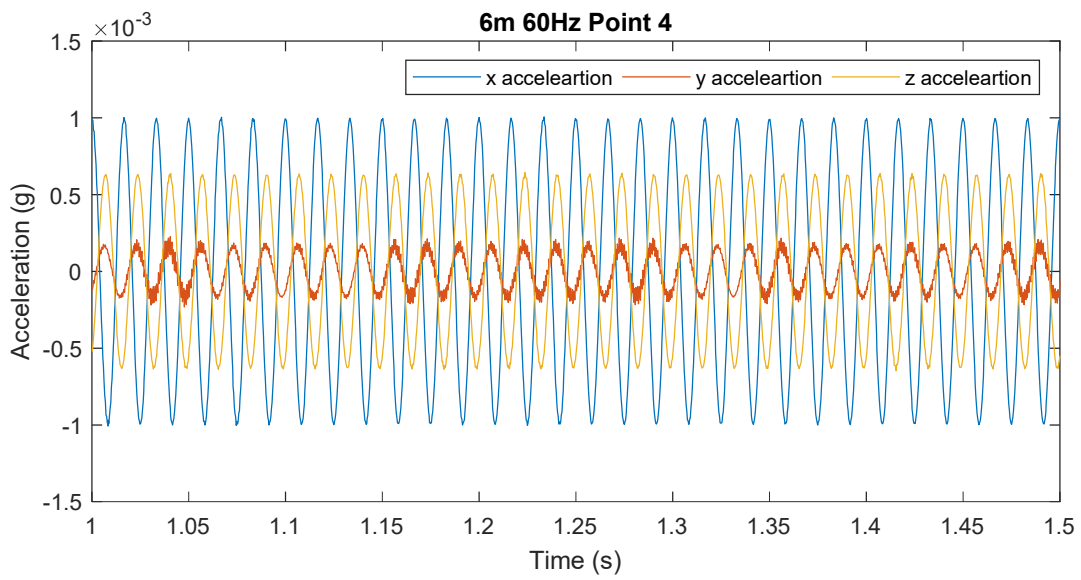


Figure A-48: Time history for 60 Hz at Point 4 of 6-meter shaft length simulation

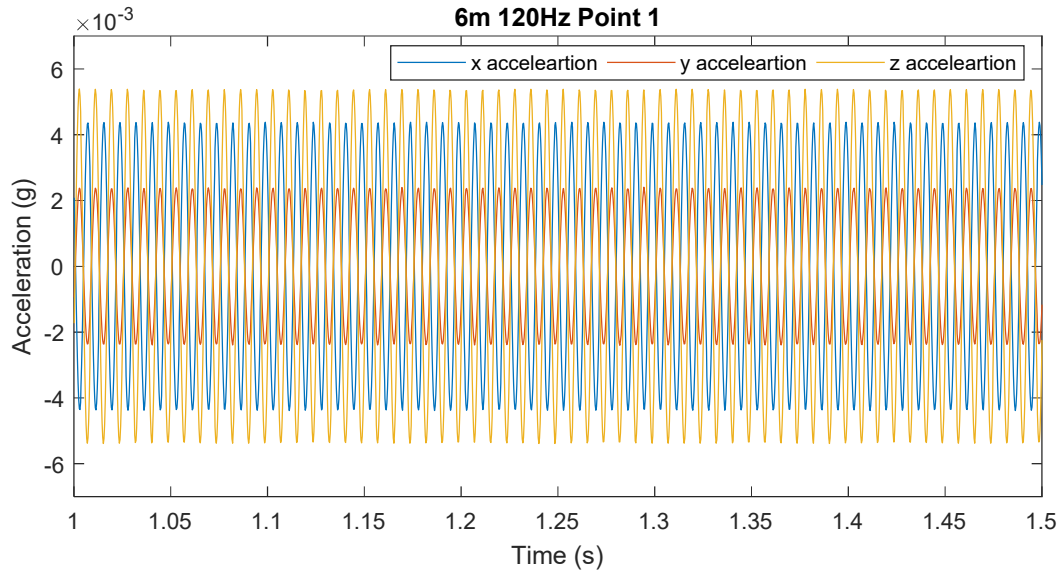


Figure A-49: Time history for 120 Hz at Point 1 of 6-meter shaft length simulation

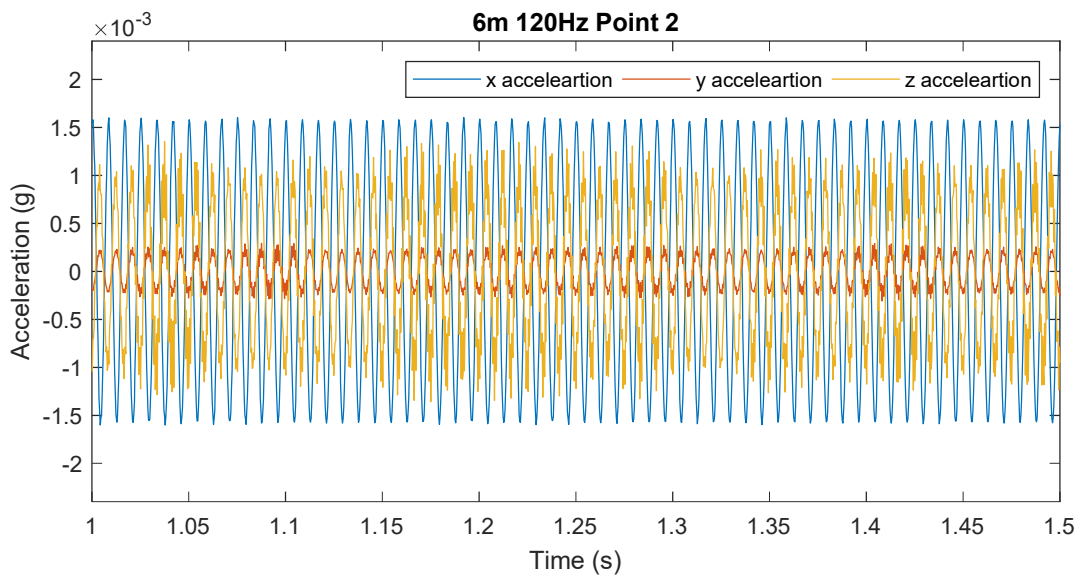


Figure A-50: Time history for 120 Hz at Point 2 of 6-meter shaft length simulation

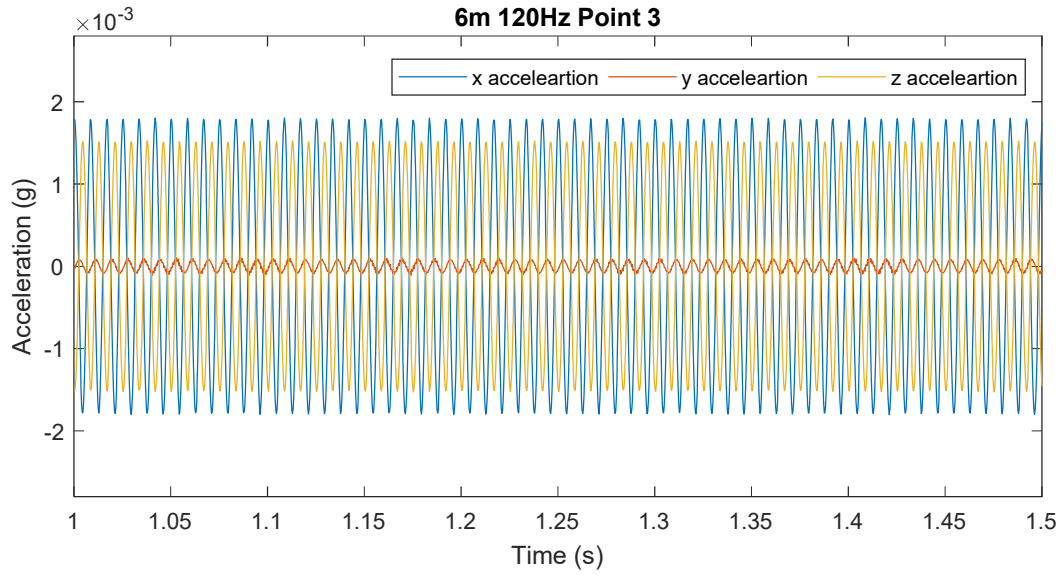


Figure A-51: Time history for 120 Hz at Point 3 of 6-meter shaft length simulation

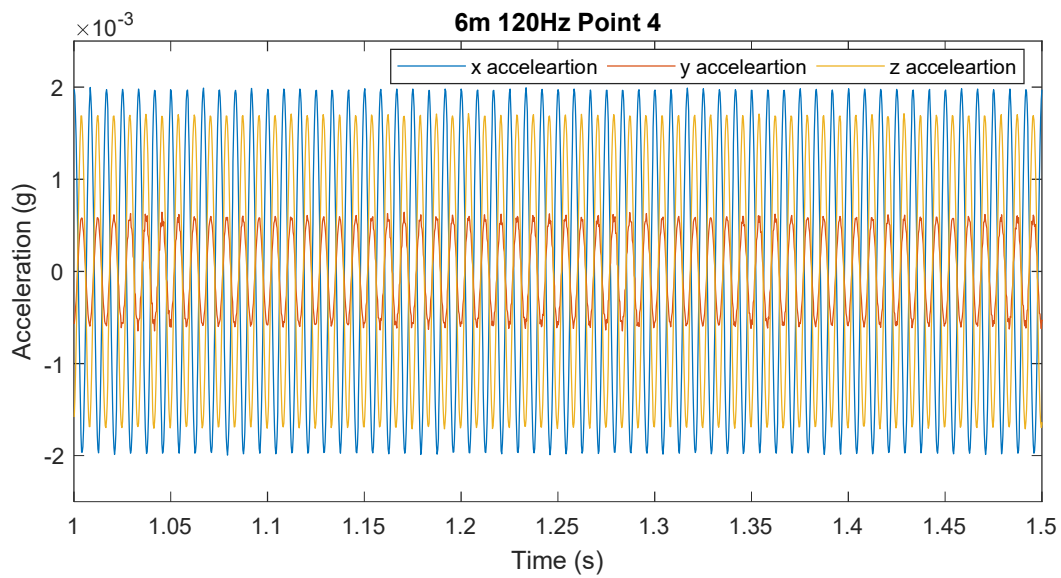


Figure A-52: Time history for 120 Hz at Point 4 of 6-meter shaft length simulation

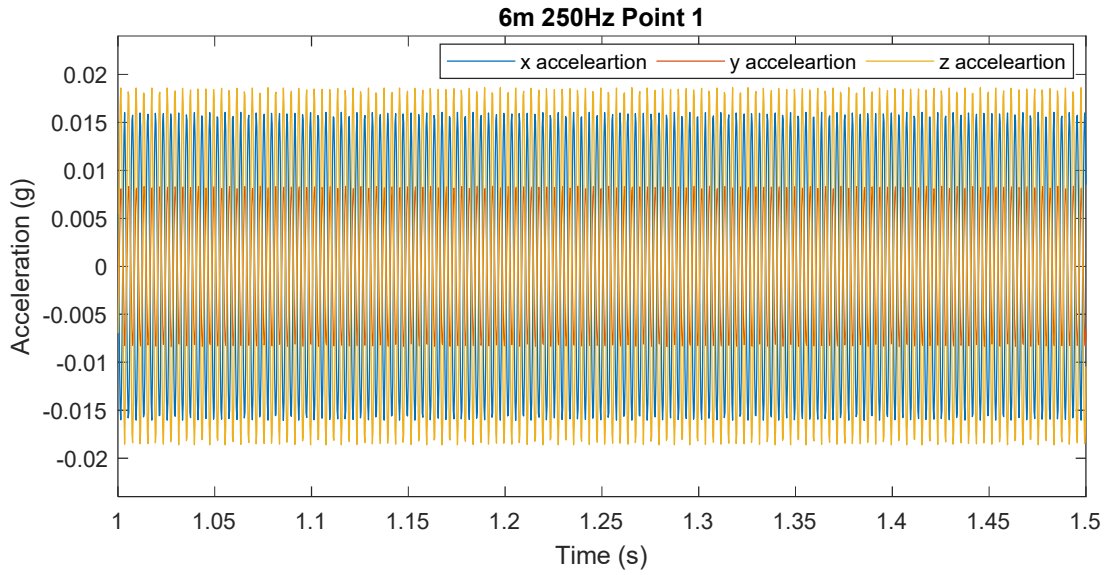


Figure A-53: Time history for 250 Hz at Point 1 of 6-meter shaft length simulation

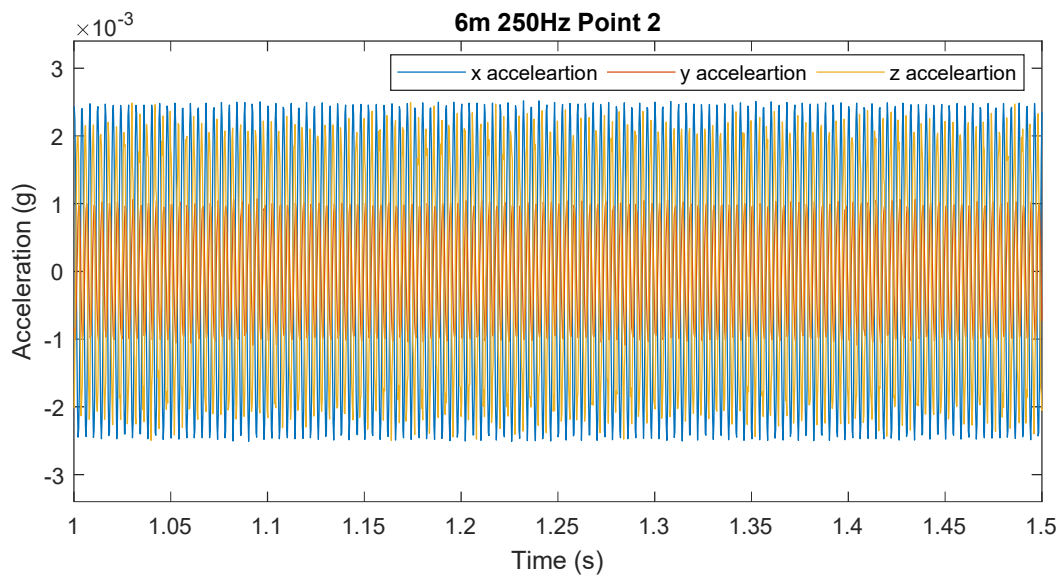


Figure A-54: Time history for 250 Hz at Point 2 of 6-meter shaft length simulation

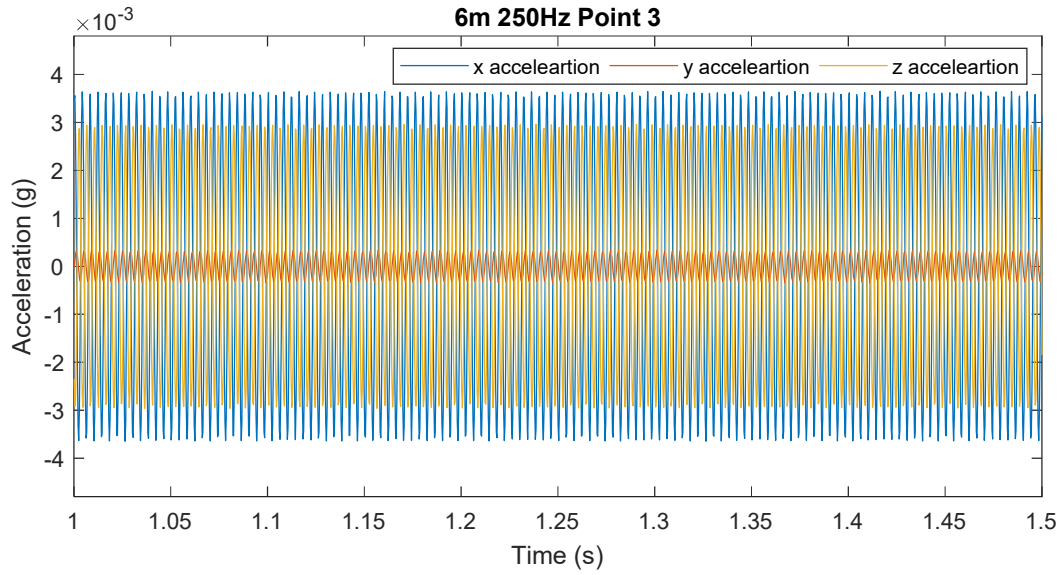


Figure A-55: Time history for 250 Hz at Point 3 of 6-meter shaft length simulation

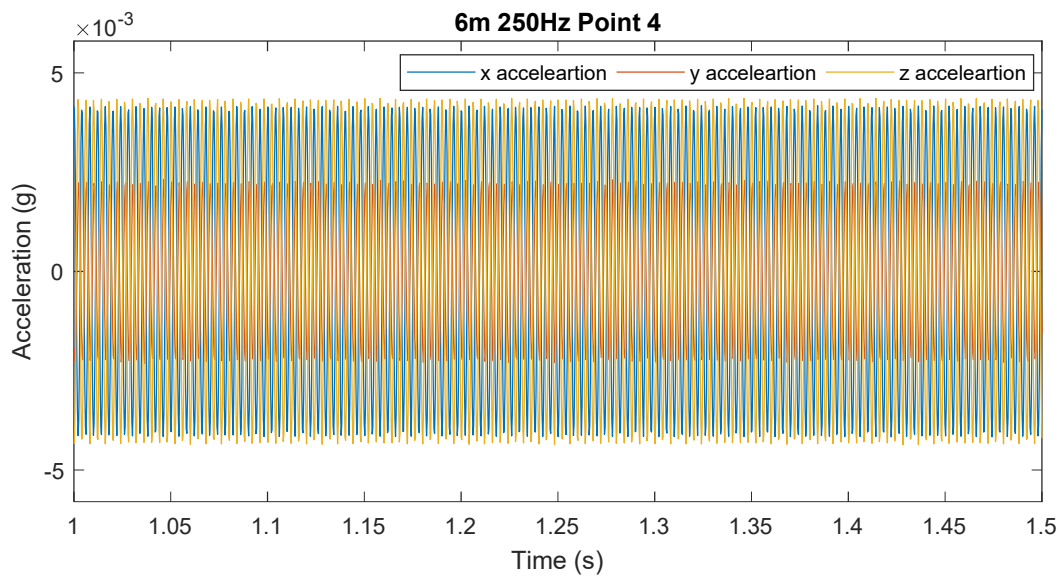


Figure A-56: Time history for 250 Hz at Point 4 of 6-meter shaft length simulation

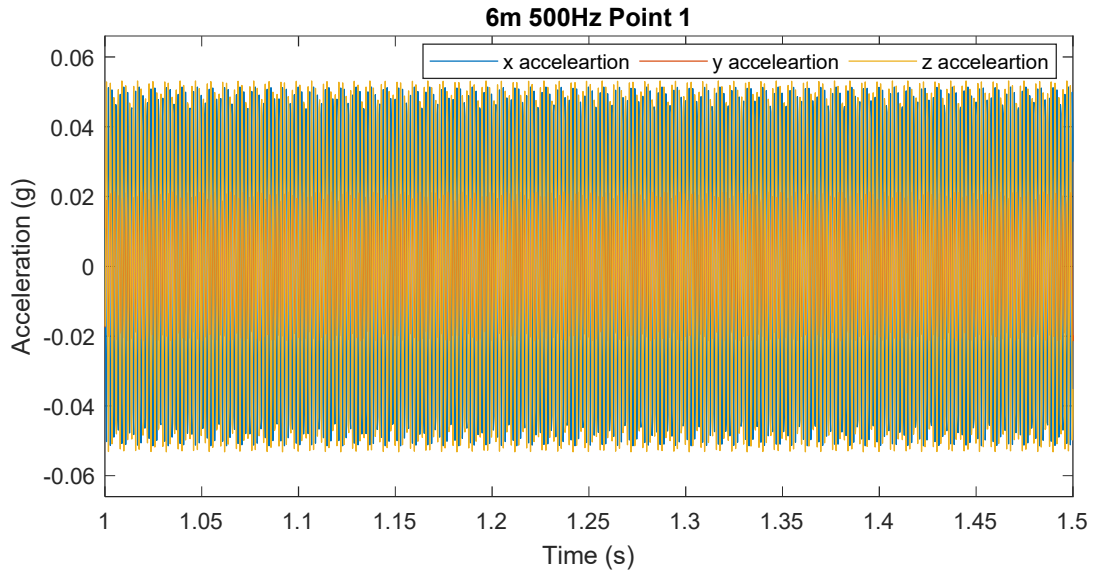


Figure A-57: Time history for 500 Hz at Point 1 of 6-meter shaft length simulation

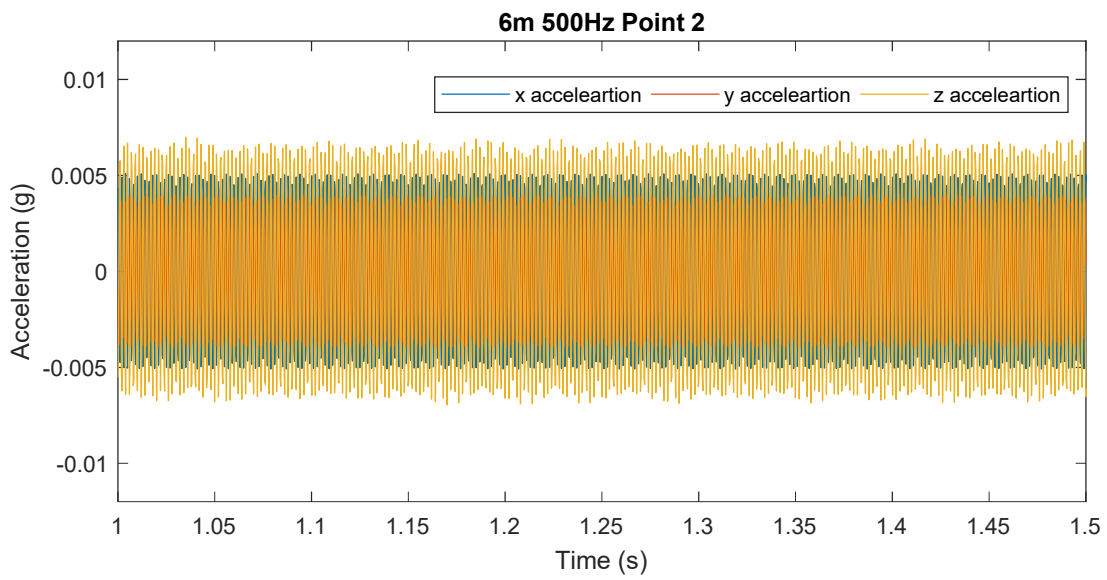


Figure A-58: Time history for 500 Hz at Point 2 of 6-meter shaft length simulation

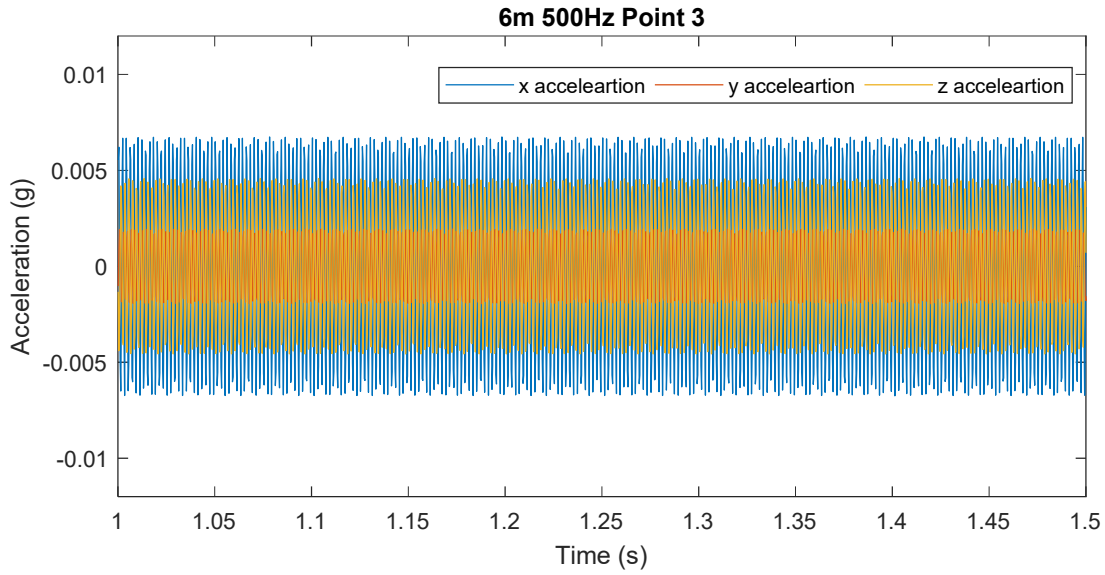


Figure A-59: Time history for 500 Hz at Point 3 of 6-meter shaft length simulation

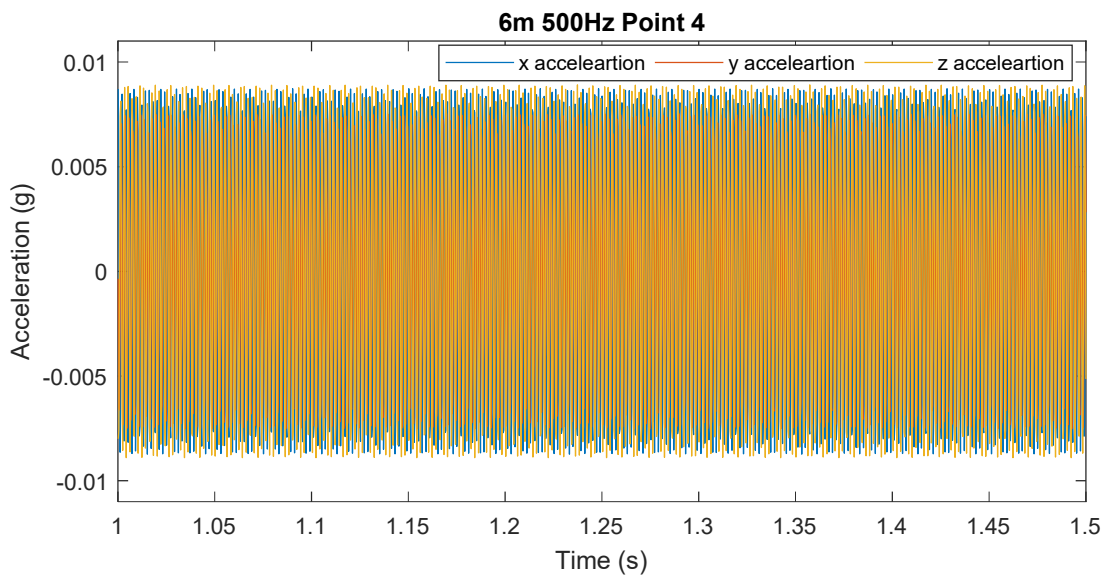


Figure A-60: Time history for 500 Hz at Point 4 of 6-meter shaft length simulation

APPENDIX B: POWER SPECTRAL DENSITIES FROM THE NUMERICAL SIMULATIONS

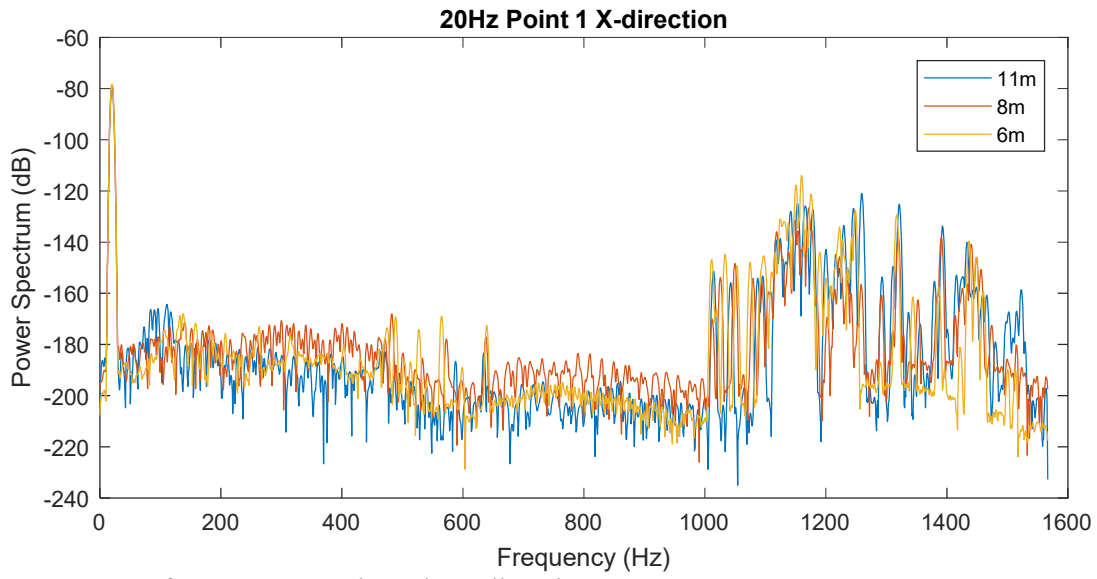


Figure B-1: PSD for 20 Hz at Point 1 in x-direction

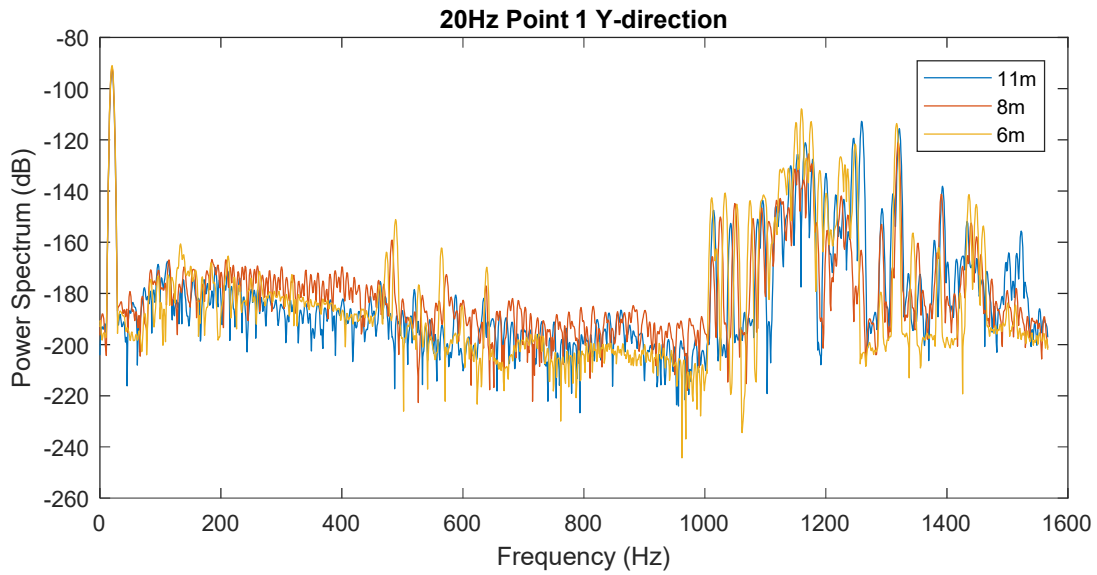


Figure B-2: PSD for 20 Hz at Point 1 in y-direction

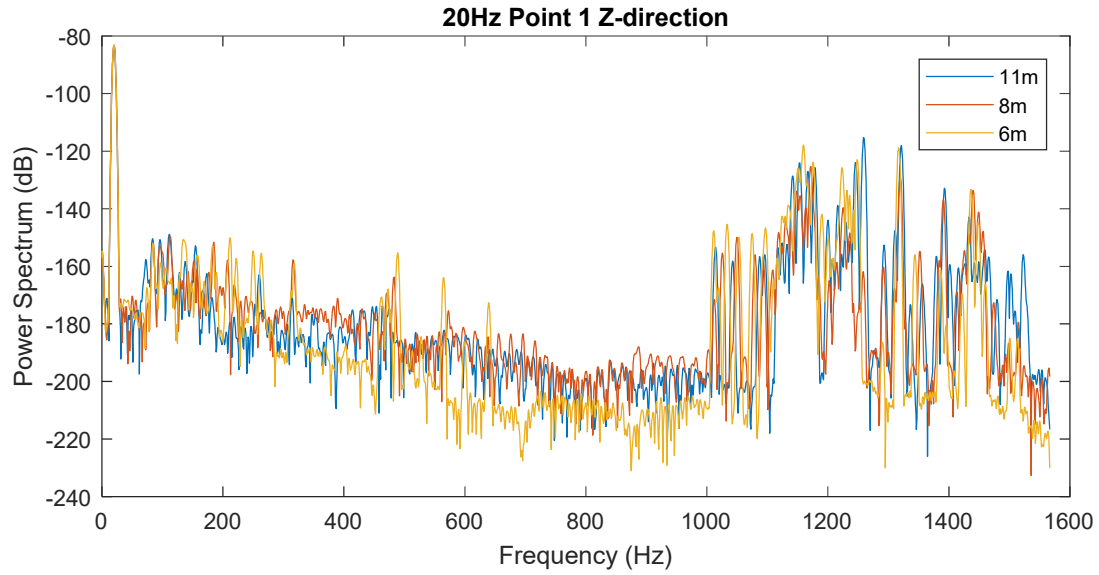


Figure B-3: PSD for 20 Hz at Point 1 in z-direction

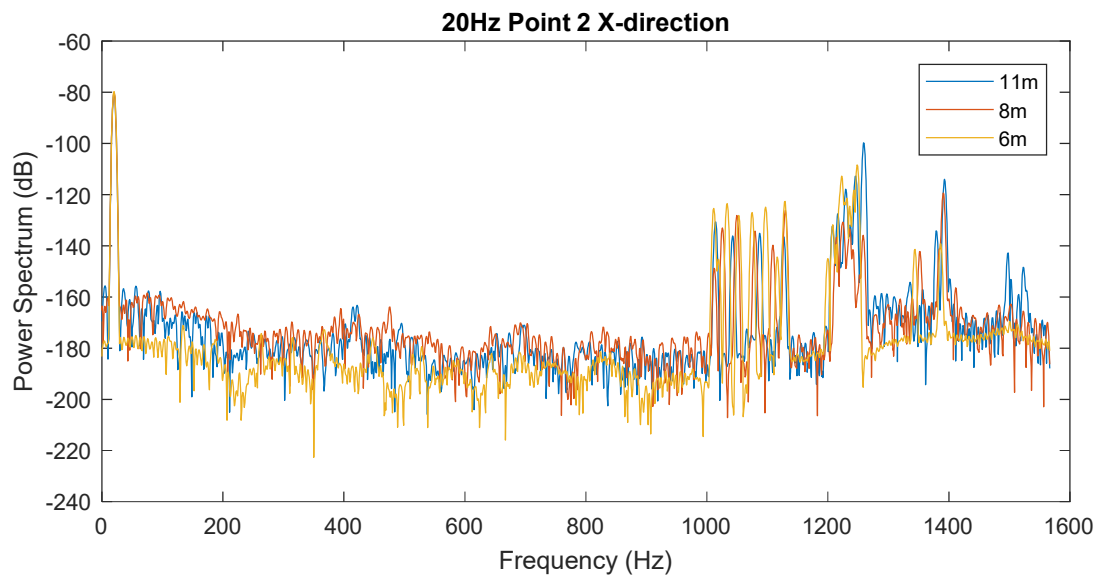


Figure B-4: PSD for 20 Hz at Point 2 in x-direction

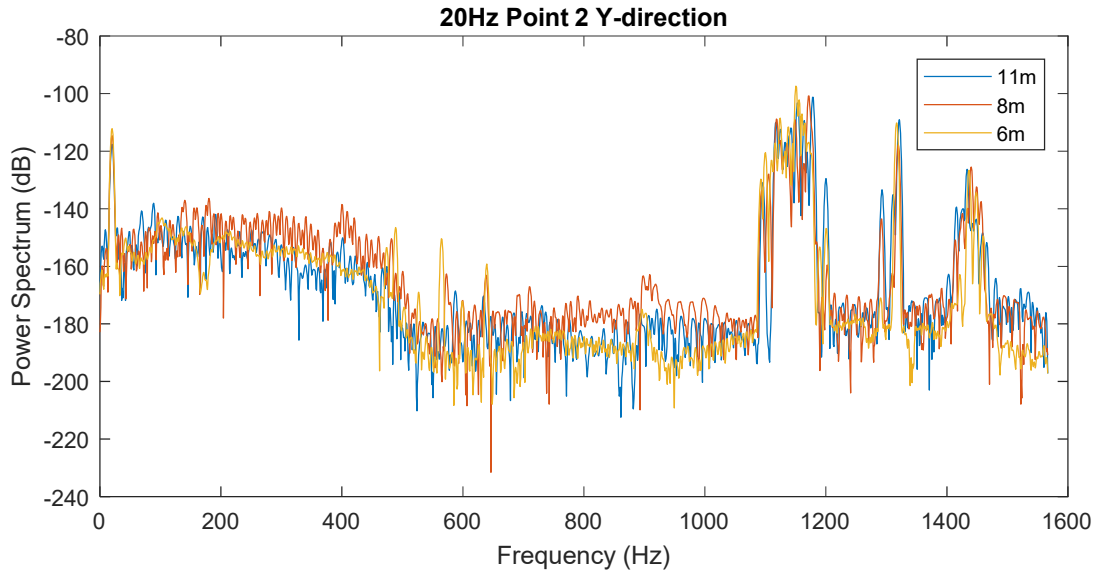


Figure B-5: PSD for 20 Hz at Point 2 in y-direction

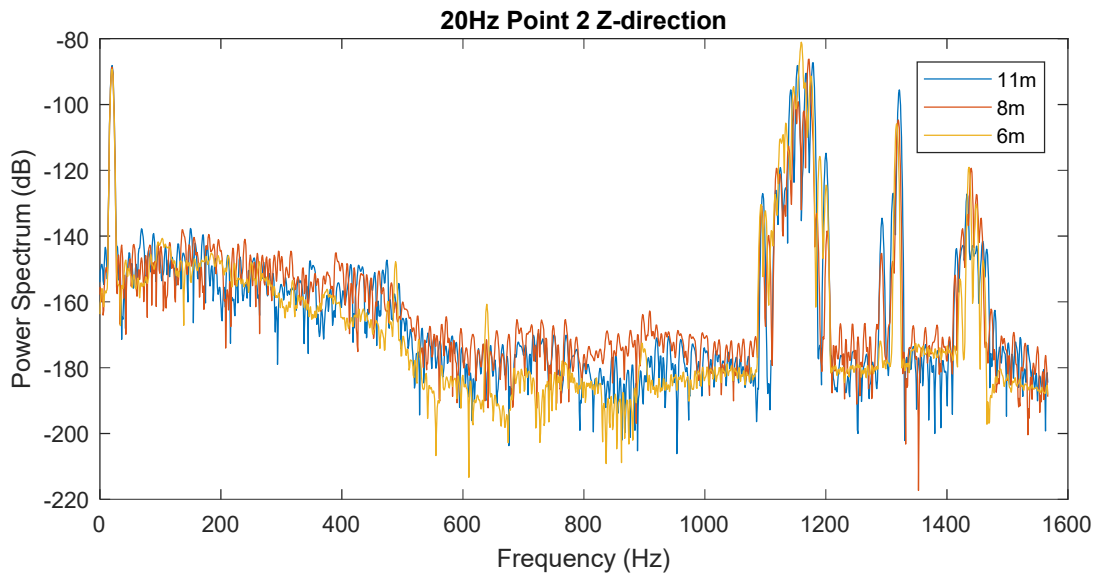


Figure B-6: PSD for 20 Hz at Point 2 in z-direction

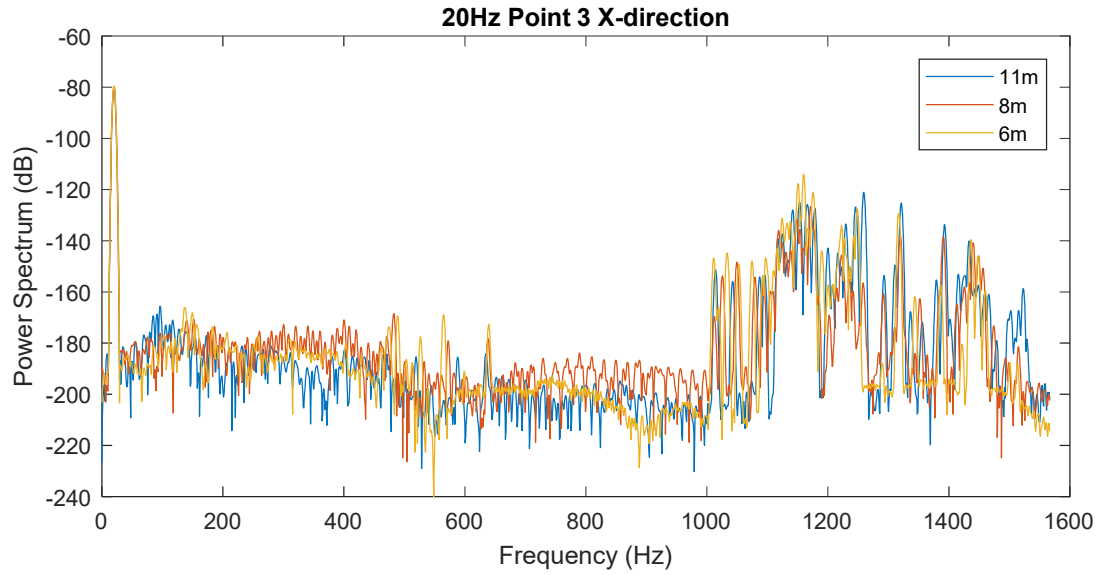


Figure B-7: PSD for 20 Hz at Point 3 in x-direction

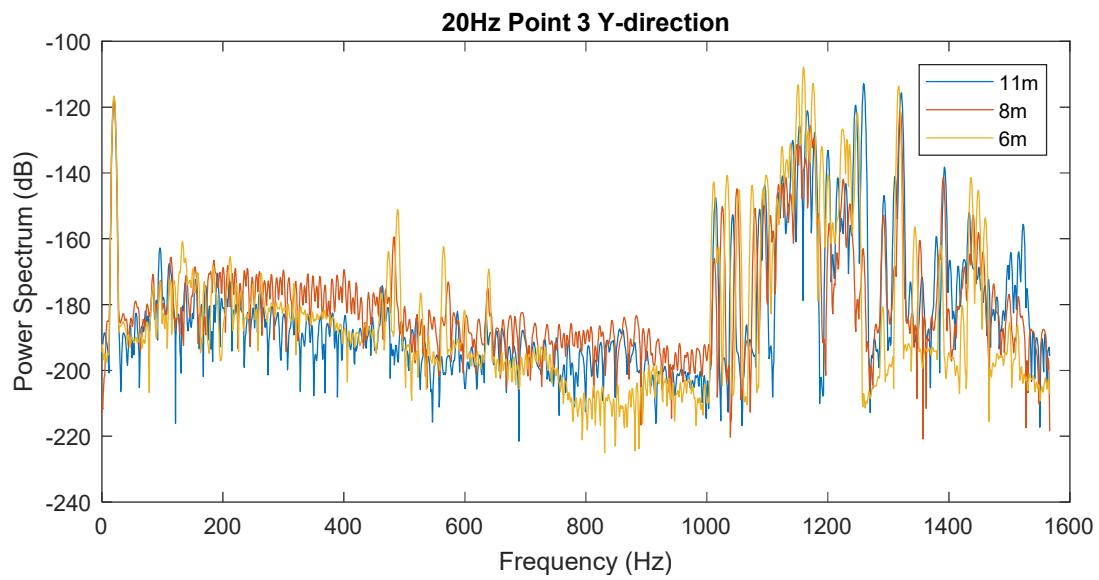


Figure B-8: PSD for 20 Hz at Point 3 in y-direction

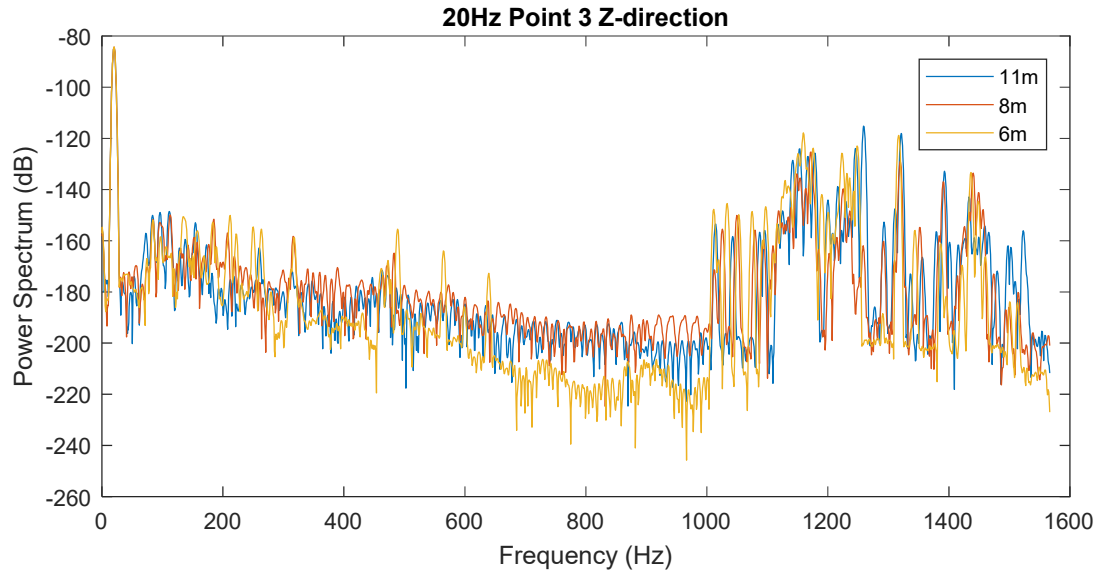


Figure B-9: PSD for 20 Hz at Point 3 in z-direction

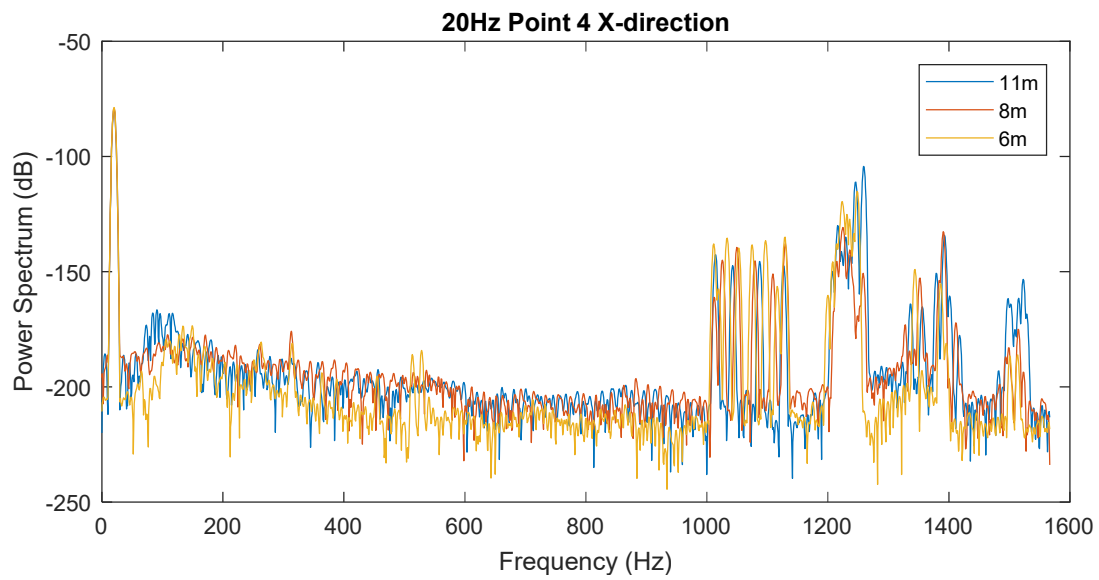


Figure B-10: PSD for 20 Hz at Point 4 in x-direction

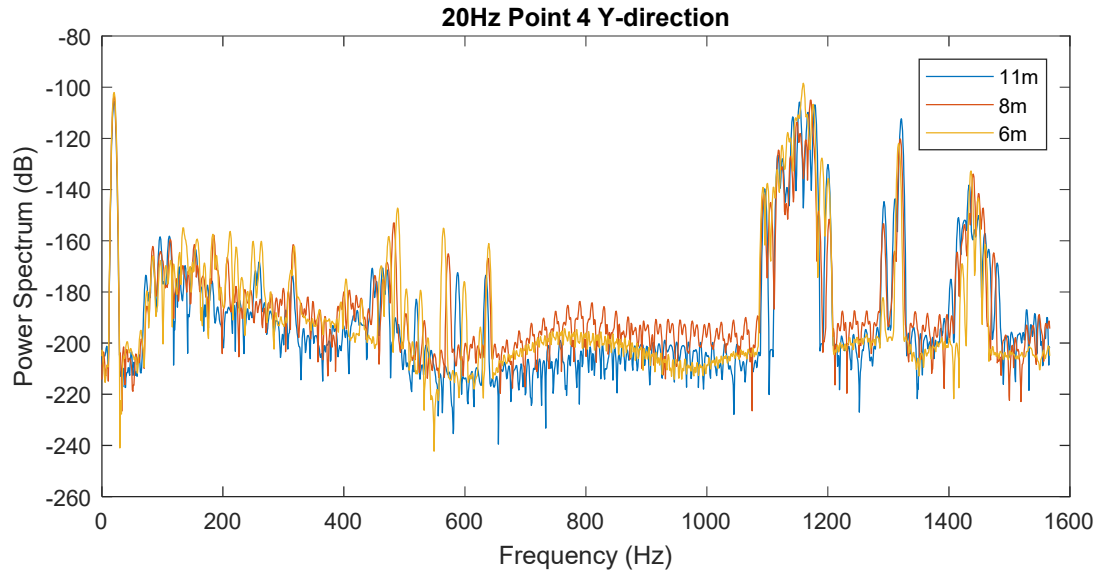


Figure B-11: PSD for 20 Hz at Point 4 in y-direction

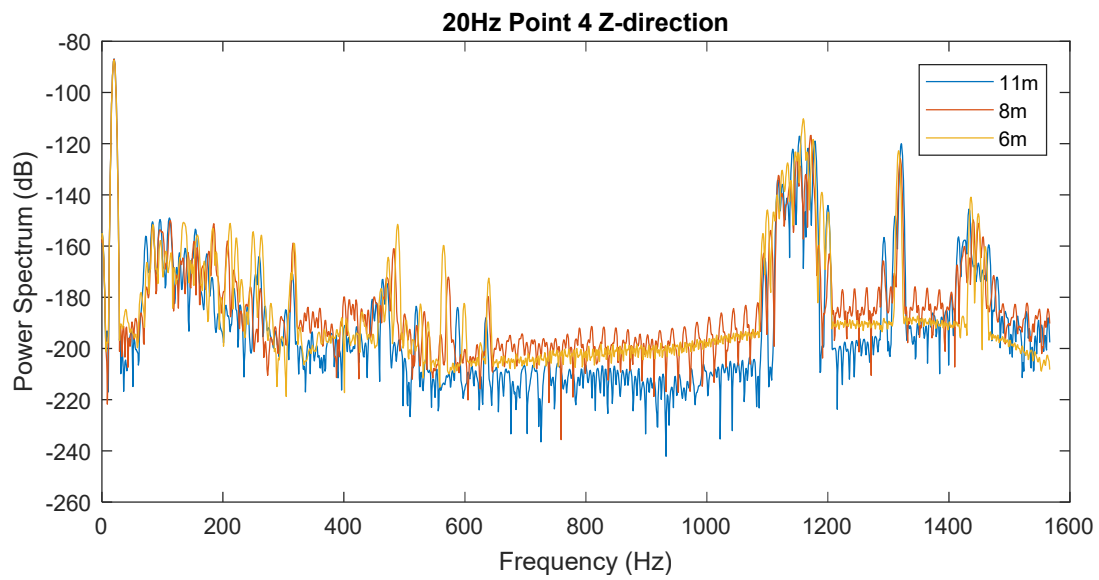


Figure B-12: PSD for 20 Hz at Point 4 in z-direction

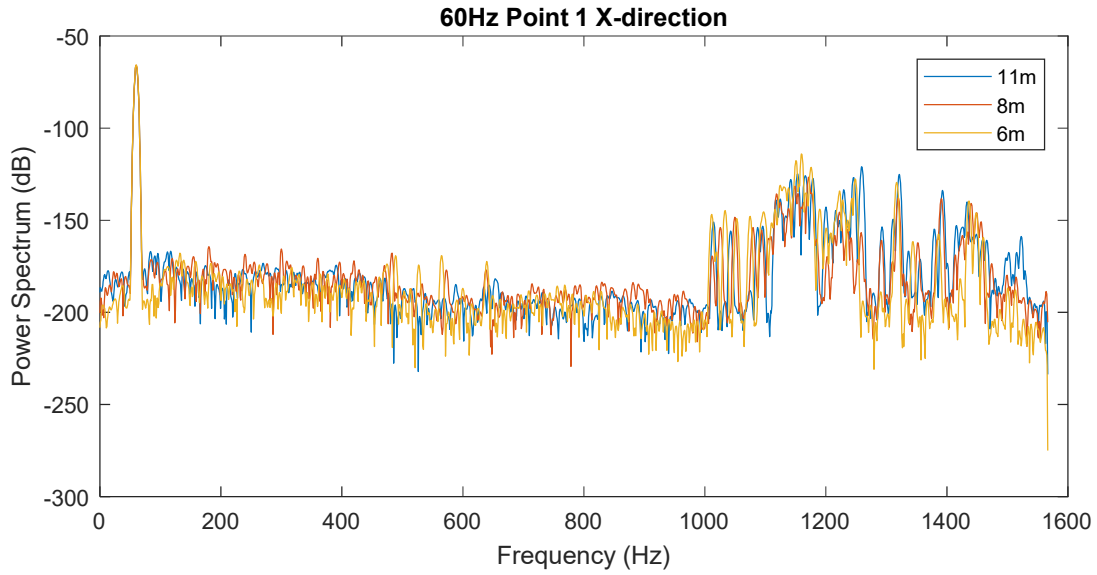


Figure B-13: PSD for 60 Hz at Point 1 in x-direction

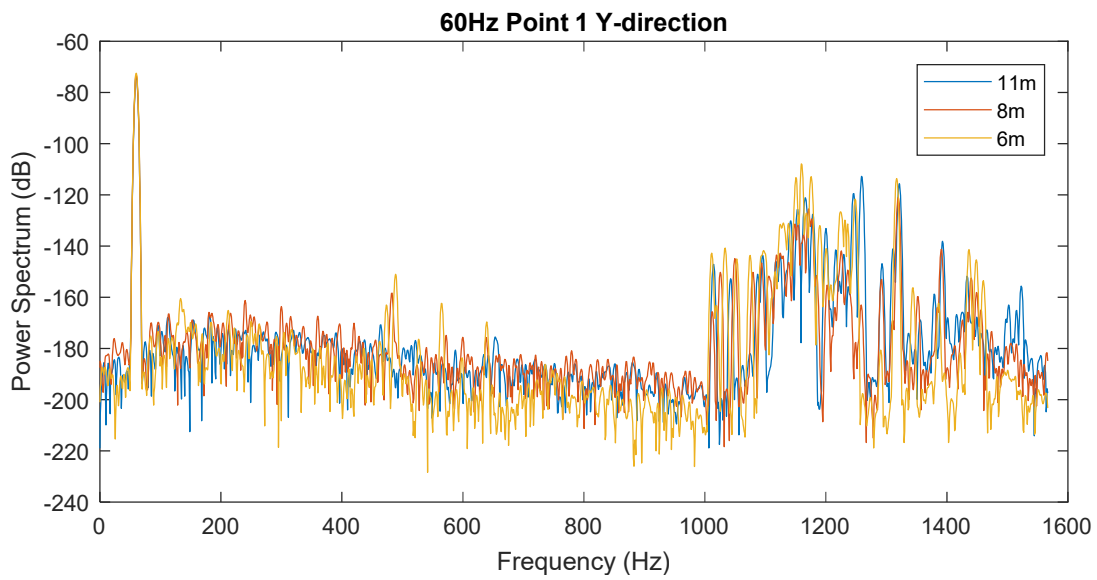


Figure B-14: PSD for 60 Hz at Point 1 in y-direction

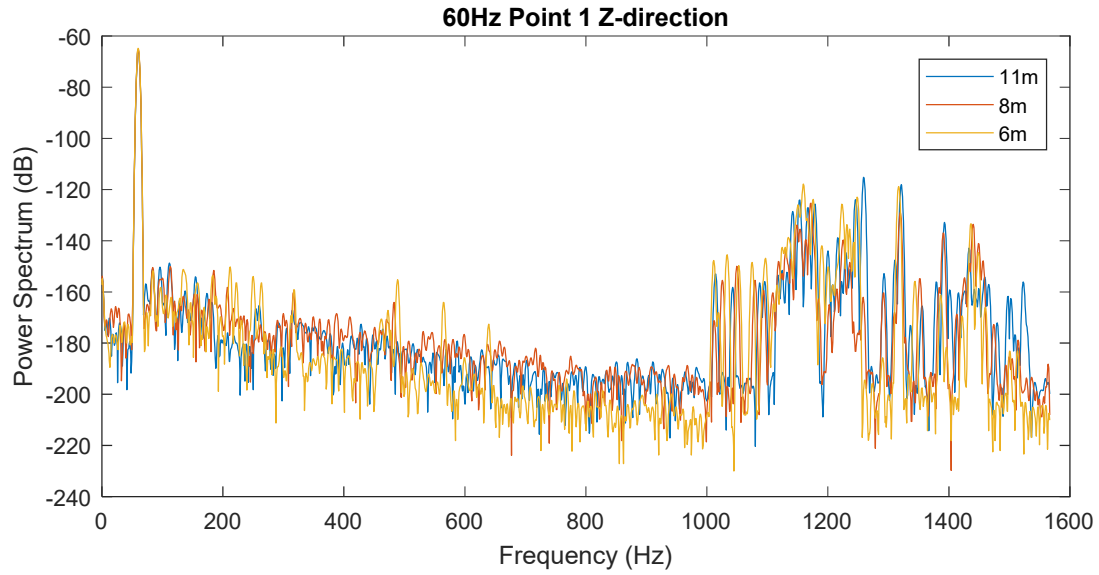


Figure B-15: PSD for 60 Hz at Point 1 in z-direction

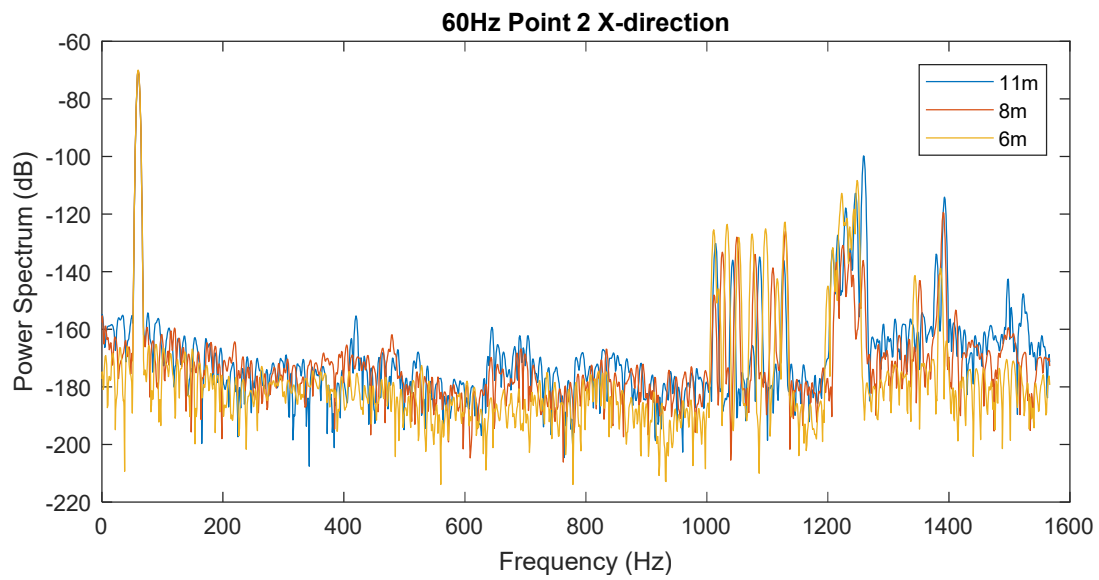


Figure B-16: PSD for 60 Hz at Point 2 in x-direction

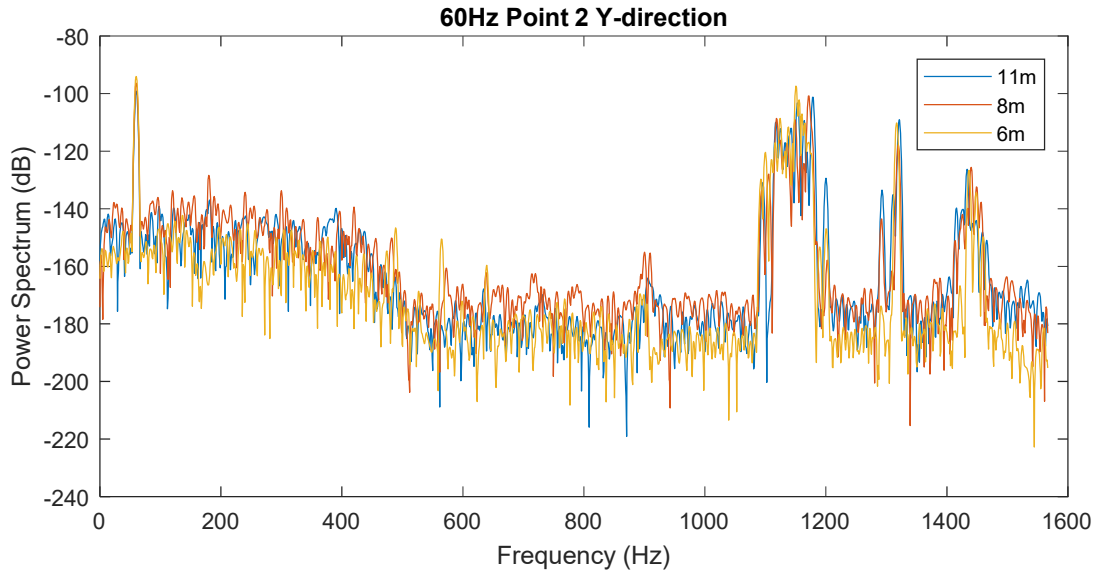


Figure B-17: PSD for 60 Hz at Point 2 in y-direction

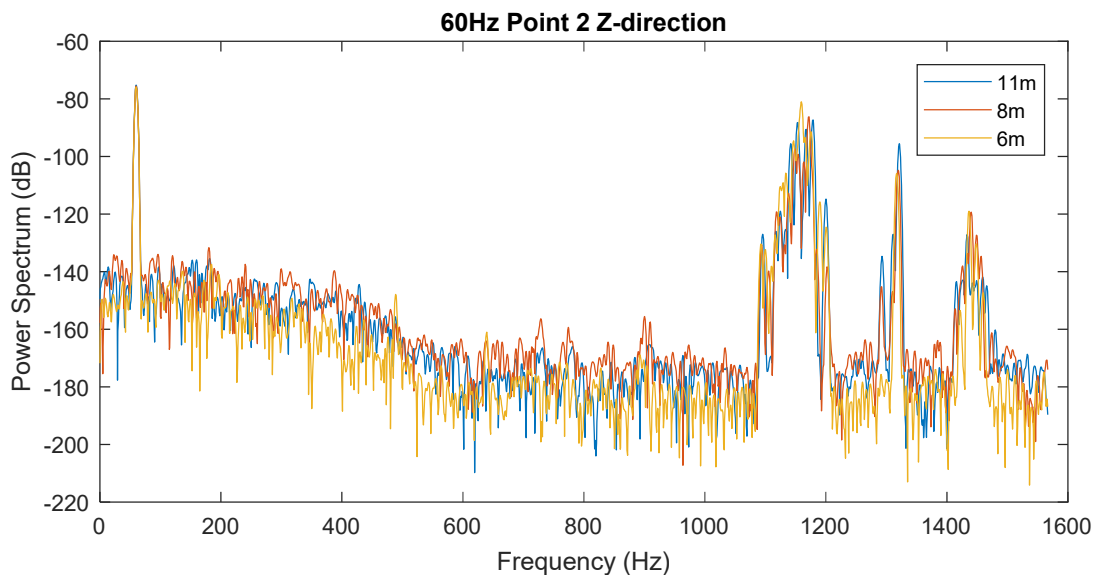


Figure B-18: PSD for 60 Hz at Point 2 in z-direction

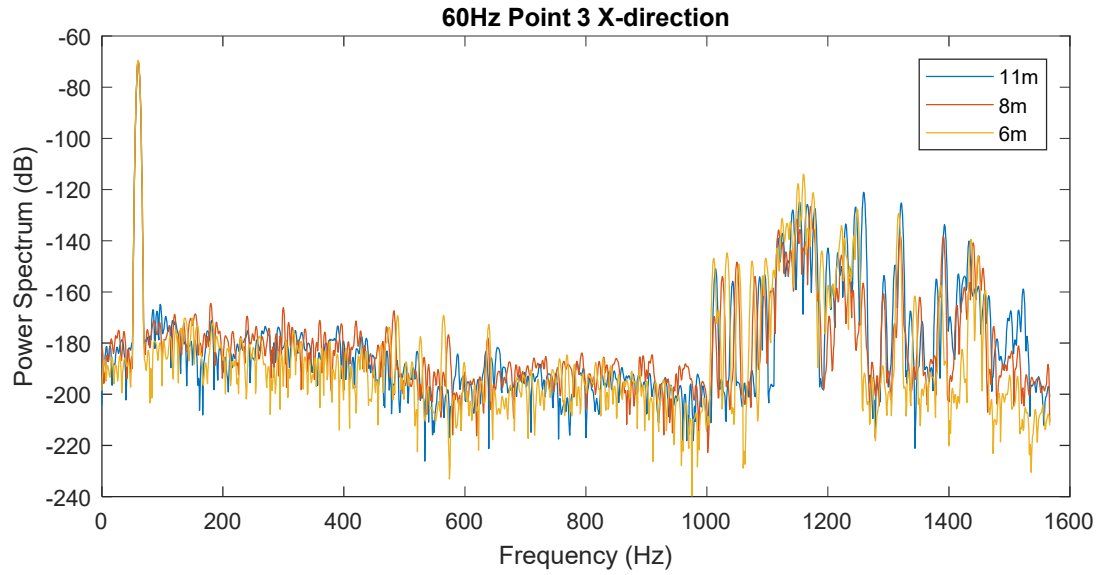


Figure B-19: PSD for 60 Hz at Point 3 in x-direction

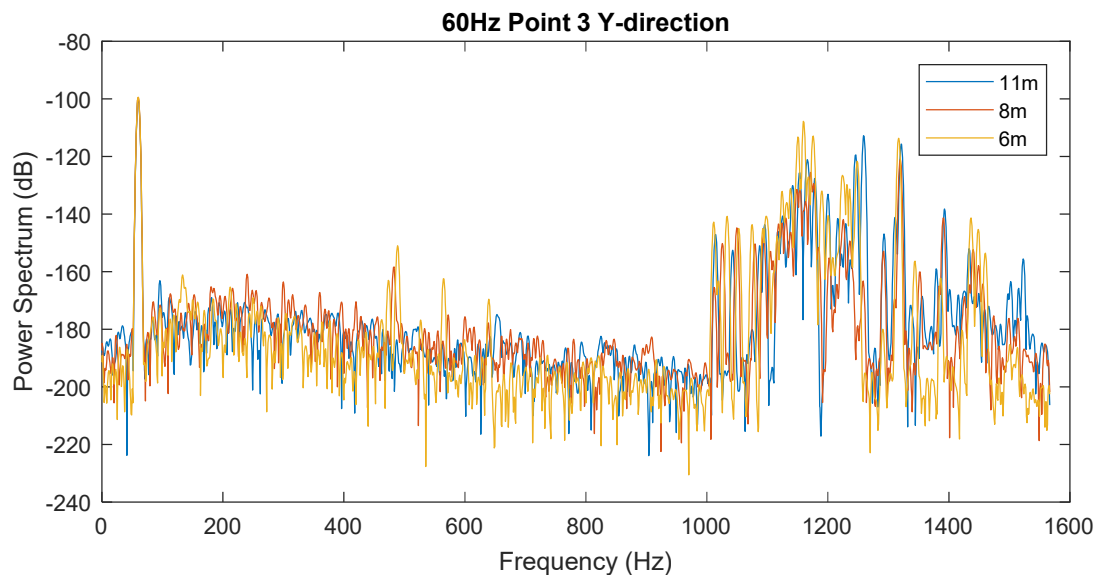


Figure B-20: PSD for 60 Hz at Point 3 in y-direction

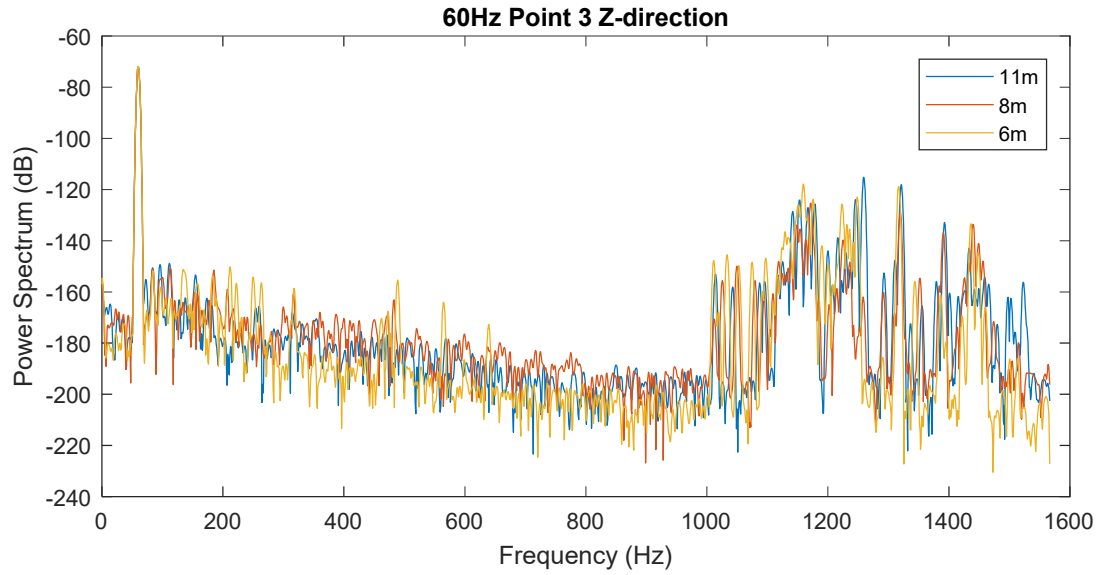


Figure B-21: PSD for 60 Hz at Point 3 in z-direction

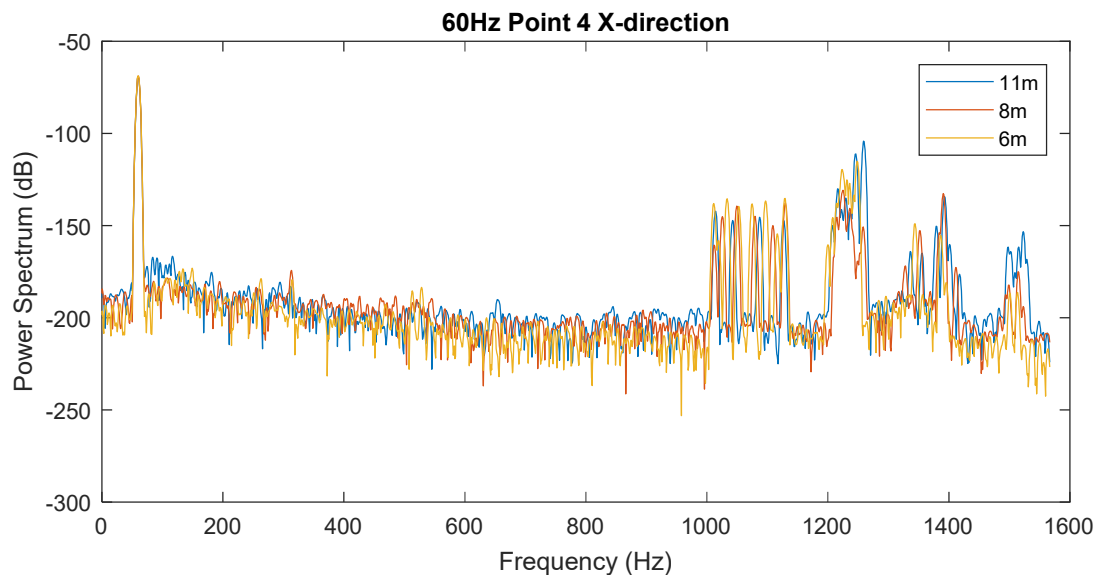


Figure B-22: PSD for 60 Hz at Point 4 in x-direction

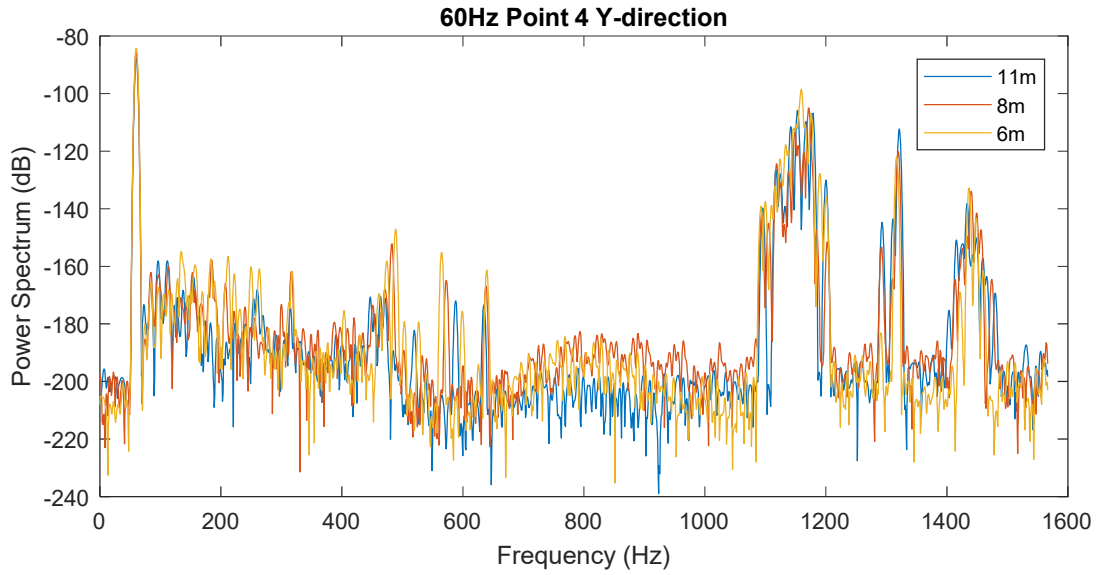


Figure B-23: PSD for 60 Hz at Point 4 in y-direction

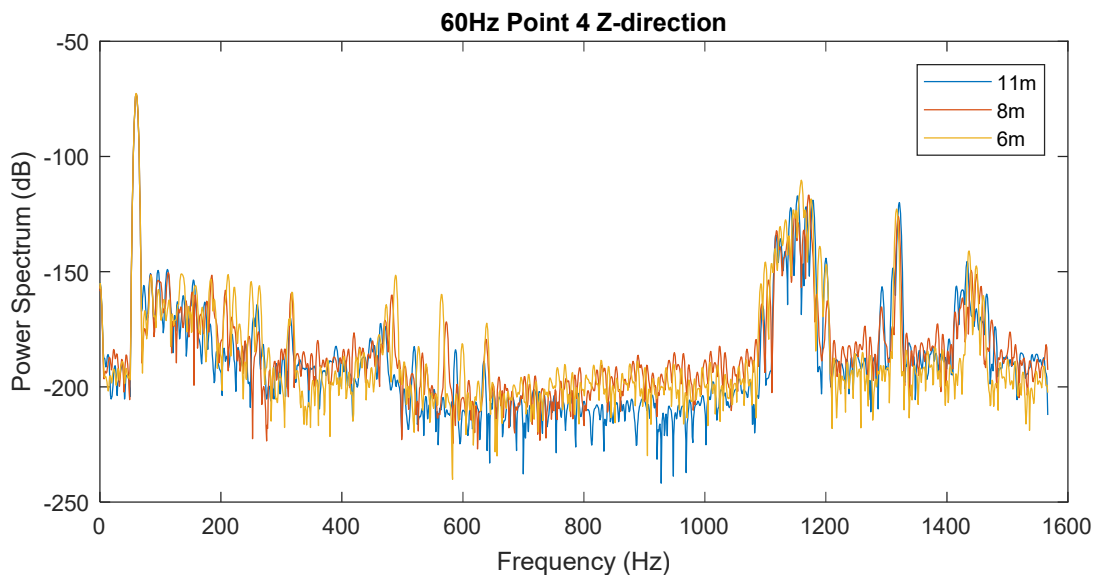


Figure B-24: PSD for 60 Hz at Point 4 in z-direction

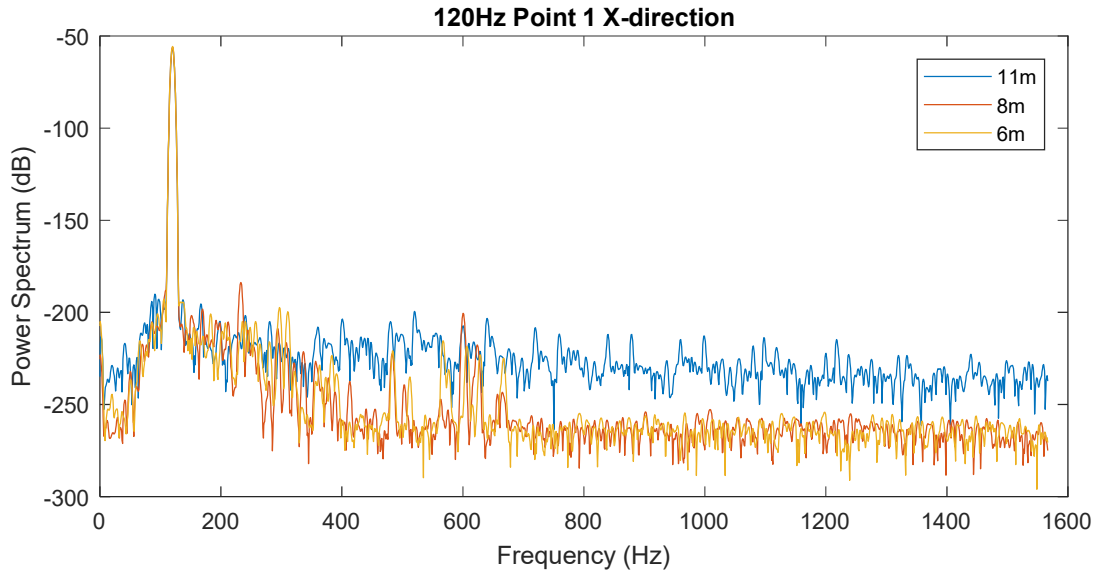


Figure B-25: PSD for 120 Hz at Point 1 in x-direction

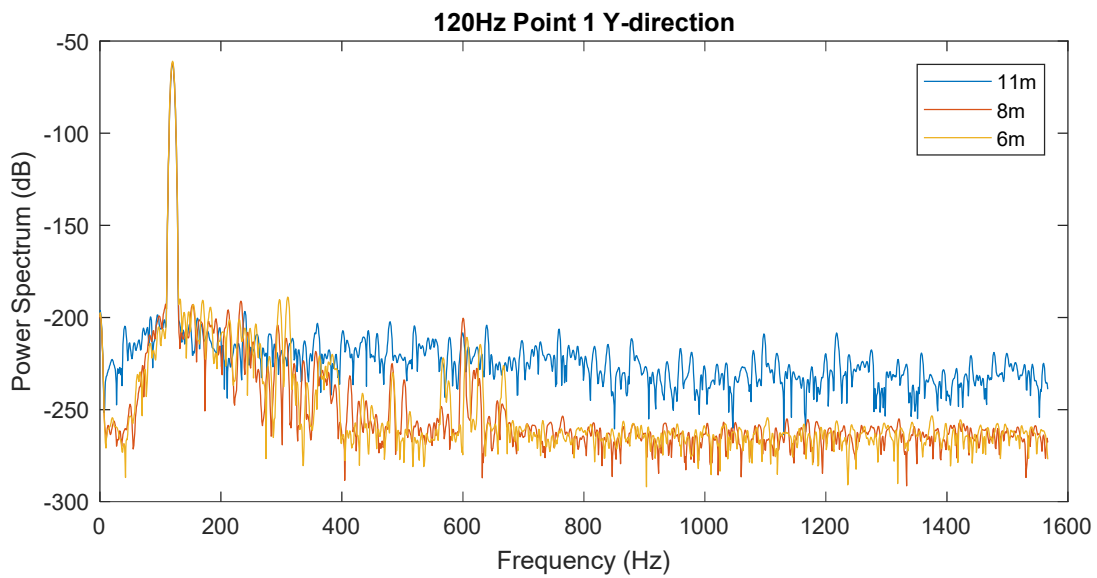


Figure B-26: PSD for 120 Hz at Point 1 in y-direction

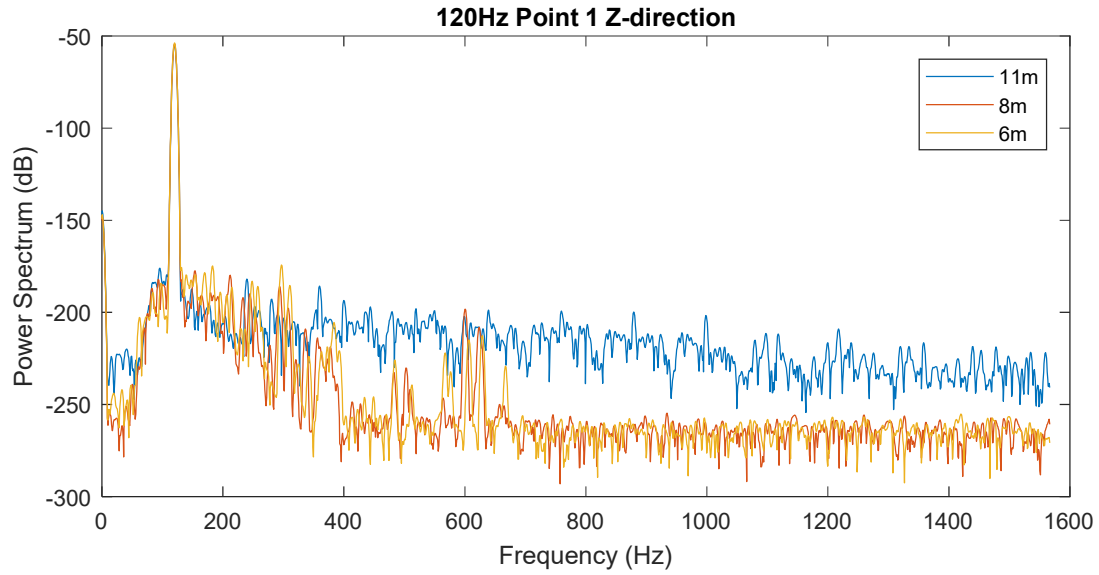


Figure B-27: PSD for 120 Hz at Point 1 in z-direction

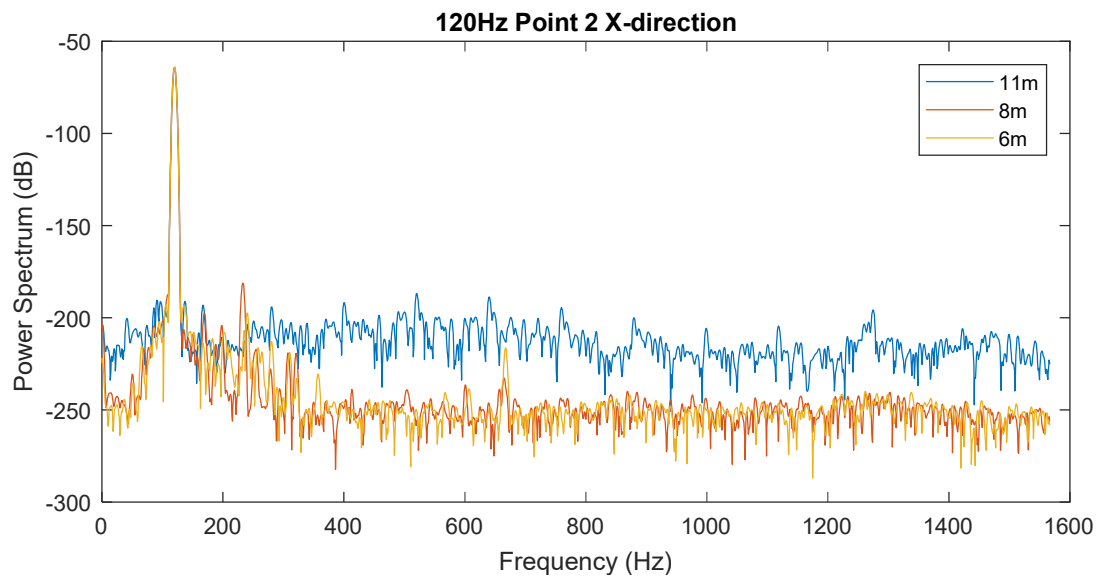


Figure B-28: PSD for 120 Hz at Point 2 in x-direction

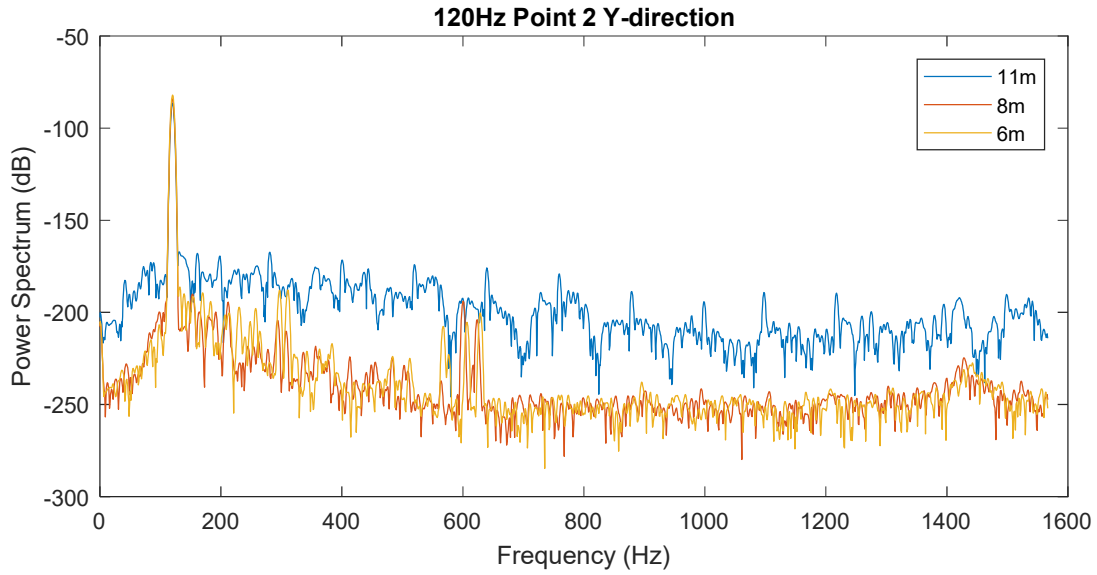


Figure B-29: PSD for 120 Hz at Point 2 in y-direction

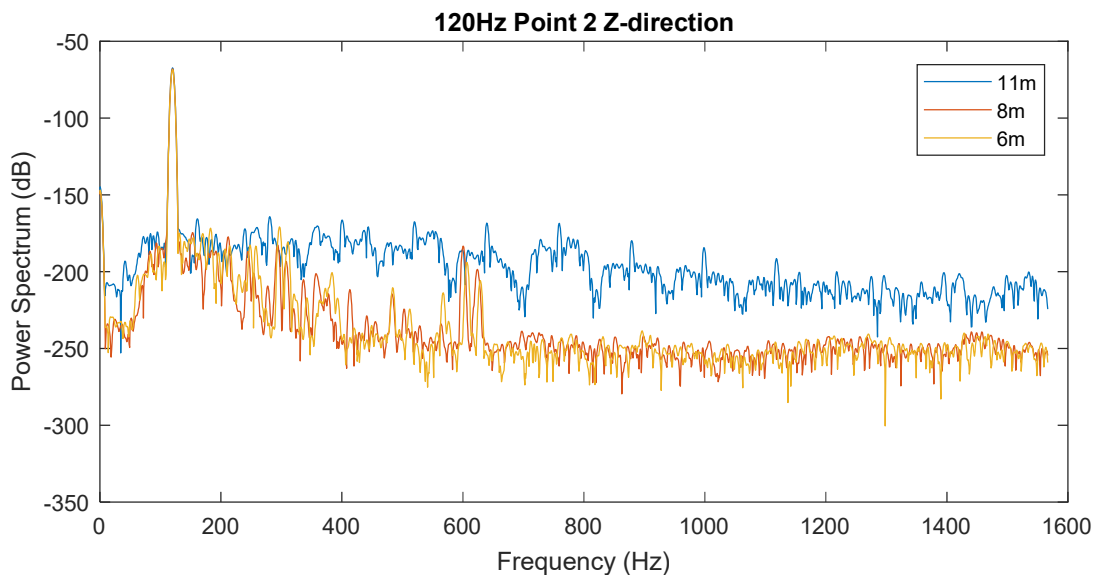


Figure B-30: PSD for 120 Hz at Point 2 in z-direction

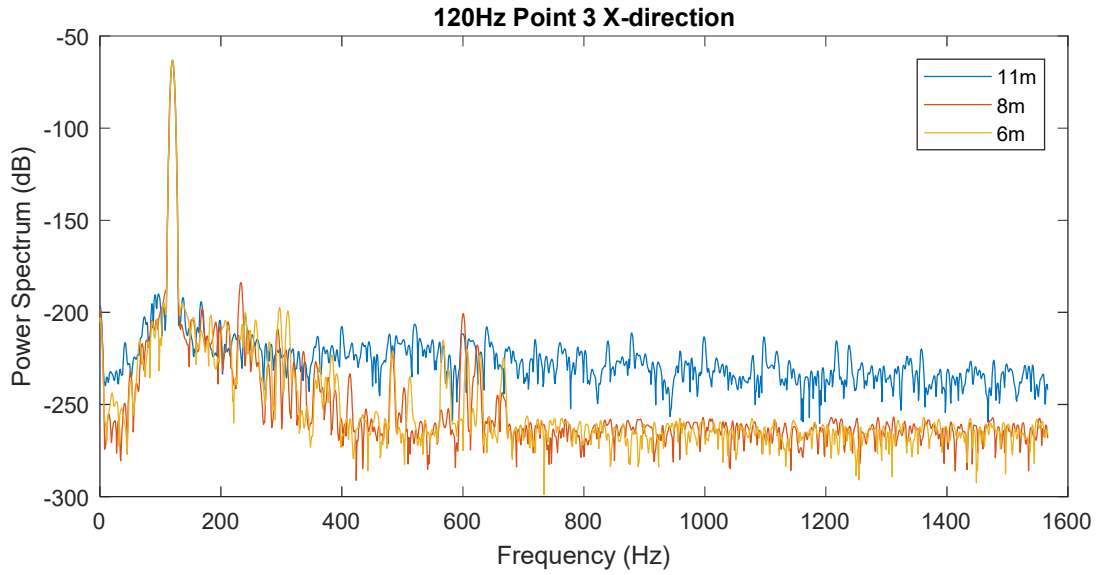


Figure B-31: PSD for 120 Hz at Point 3 in x-direction

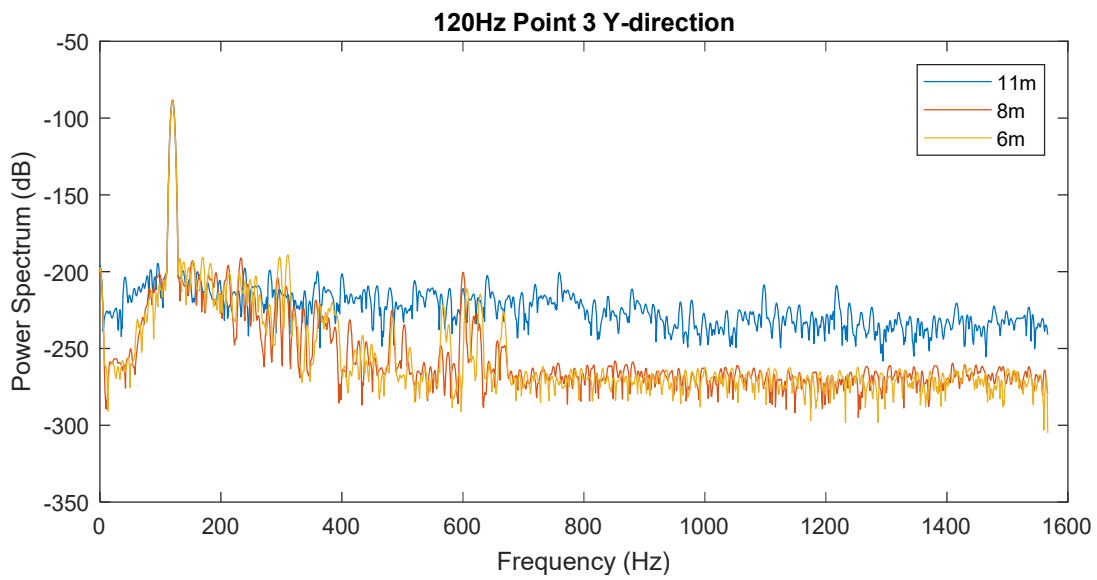


Figure B-32: PSD for 120 Hz at Point 3 in y-direction

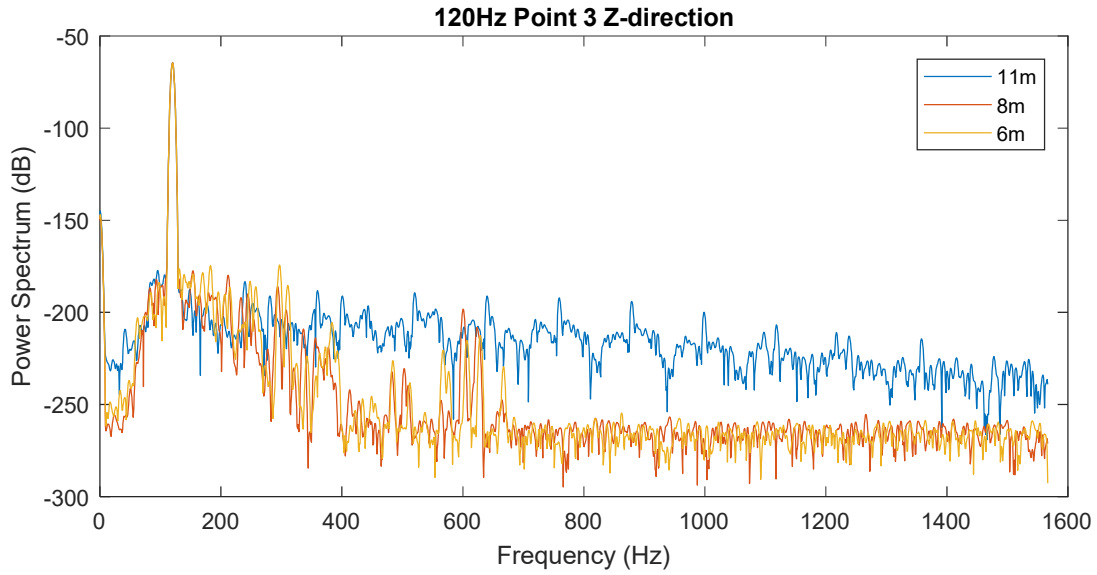


Figure B-33: PSD for 120 Hz at Point 3 in z-direction

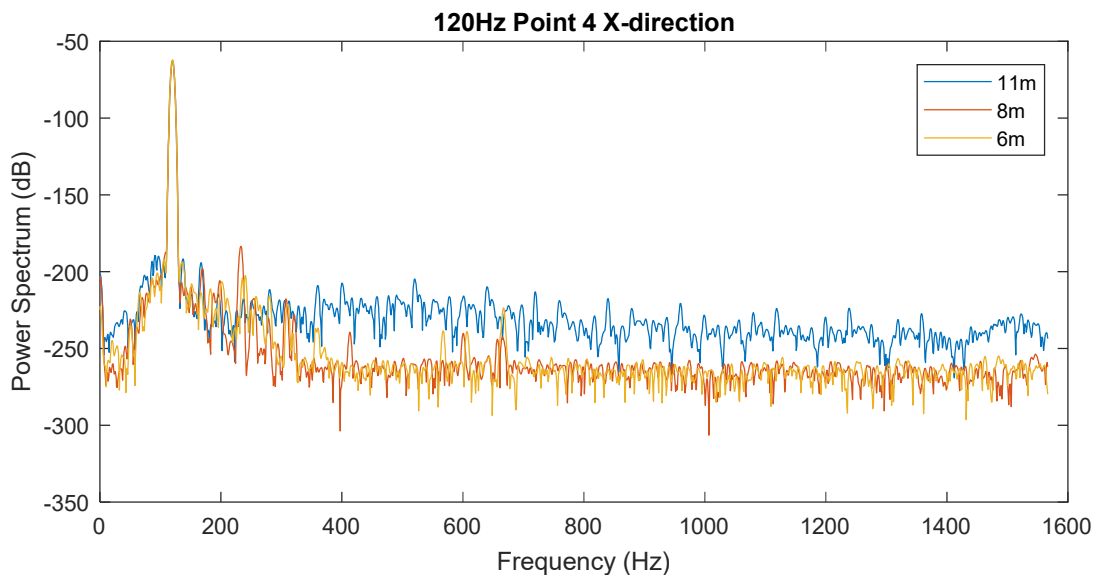


Figure B-34: PSD for 120 Hz at Point 4 in x-direction

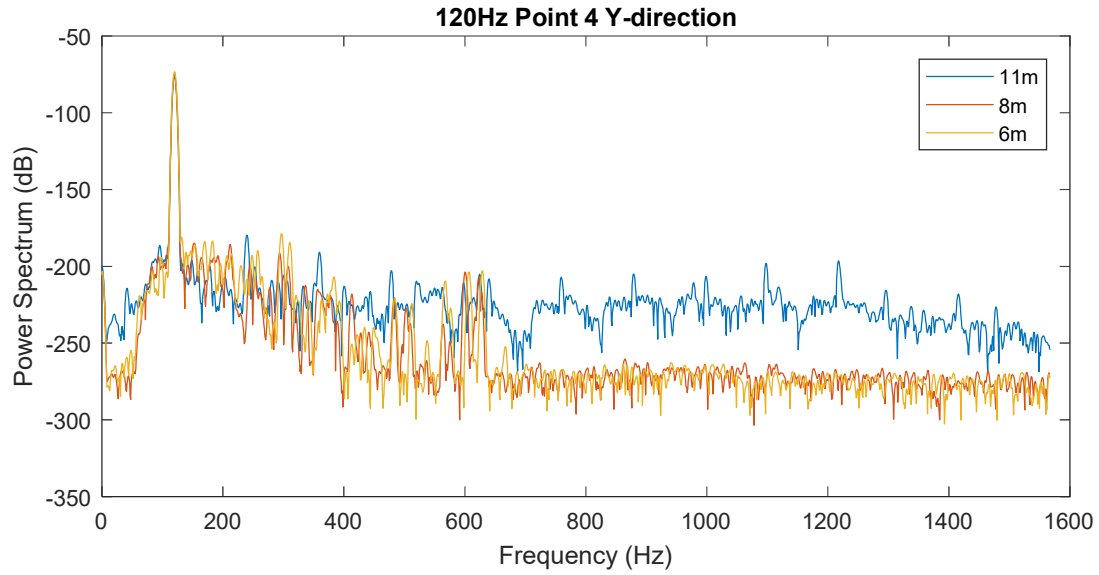


Figure B-35: PSD for 120 Hz at Point 4 in y-direction

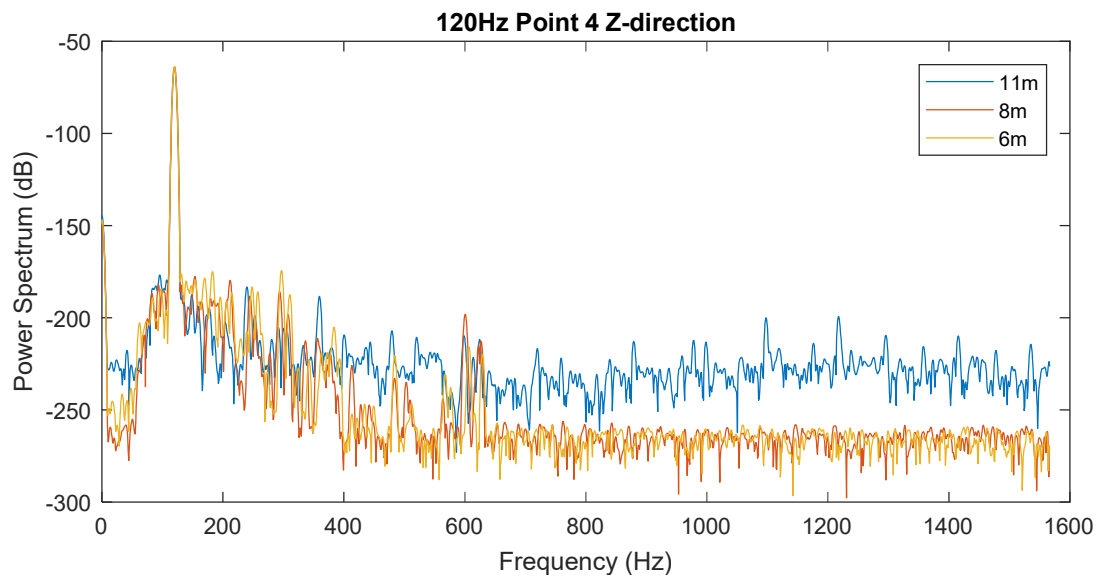


Figure B-36: PSD for 120 Hz at Point 4 in z-direction

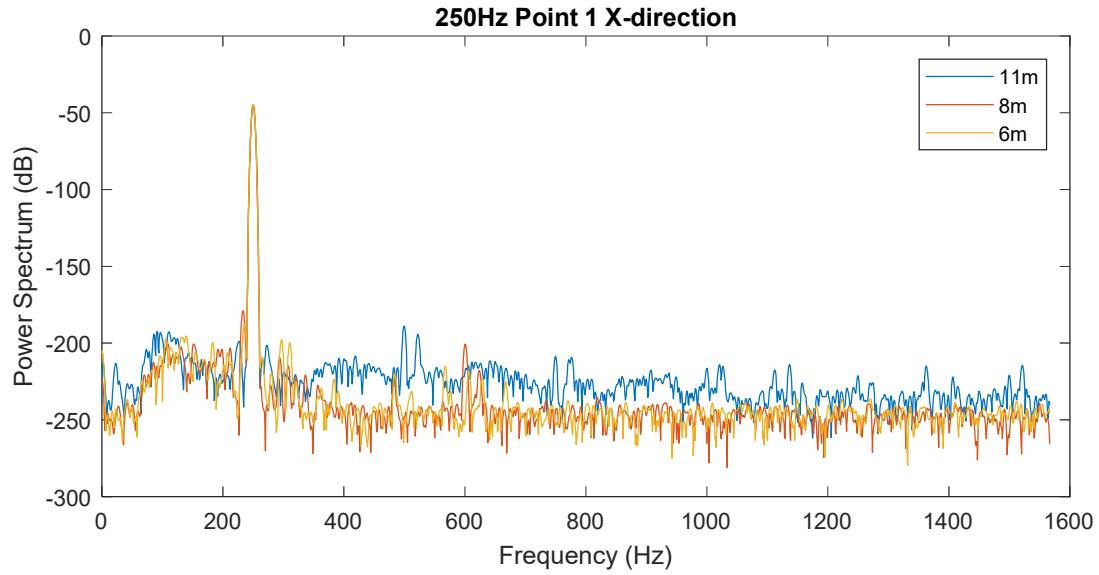


Figure B-37: PSD for 250 Hz at Point 1 in x-direction

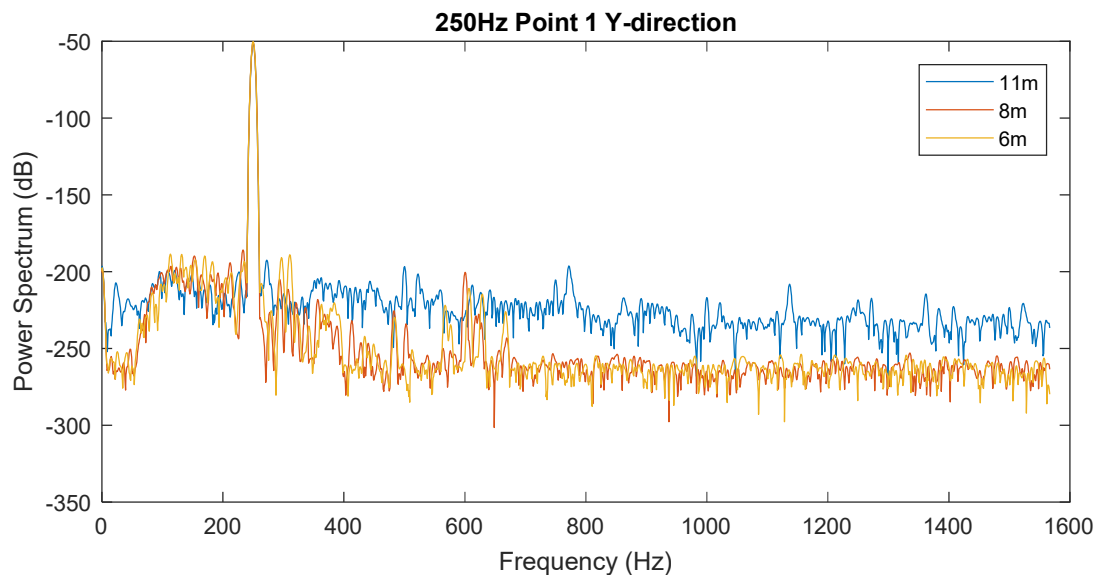


Figure B-38: PSD for 250 Hz at Point 1 in y-direction

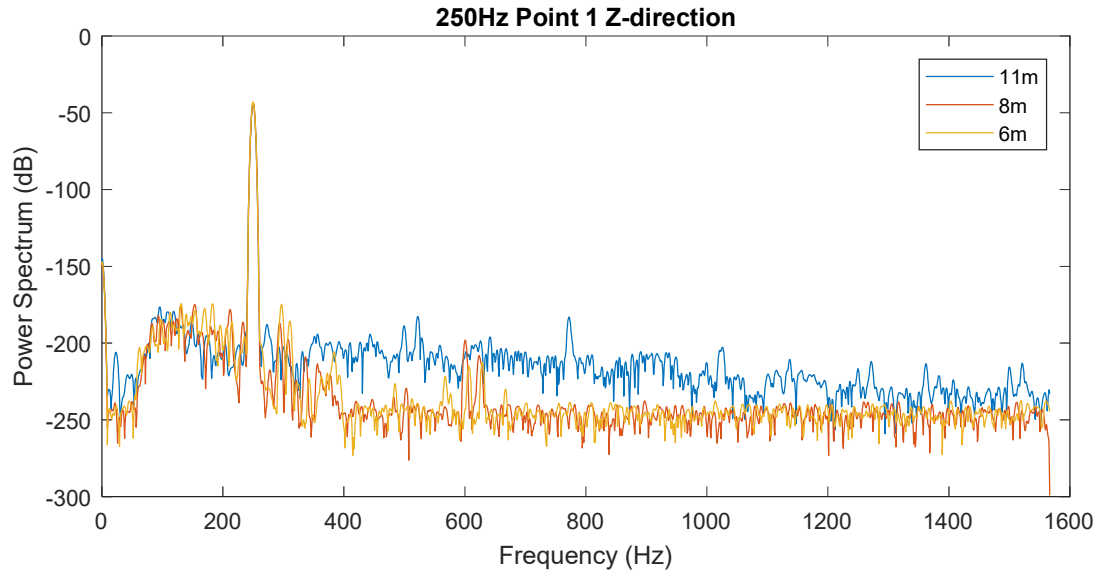


Figure B-39: PSD for 250 Hz at Point 1 in z-direction

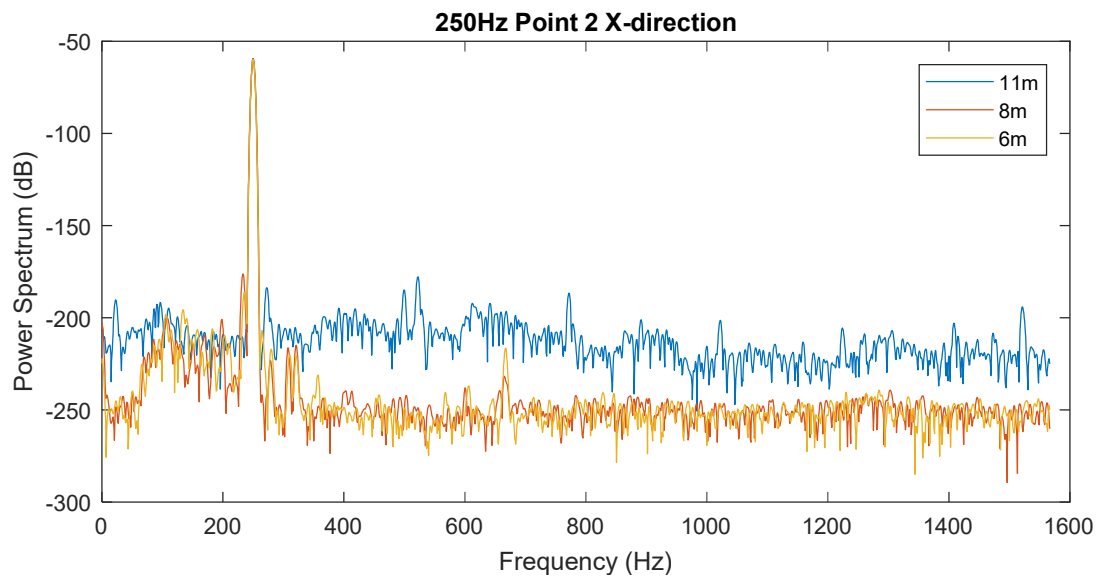


Figure B-40: PSD for 250 Hz at Point 2 in x-direction

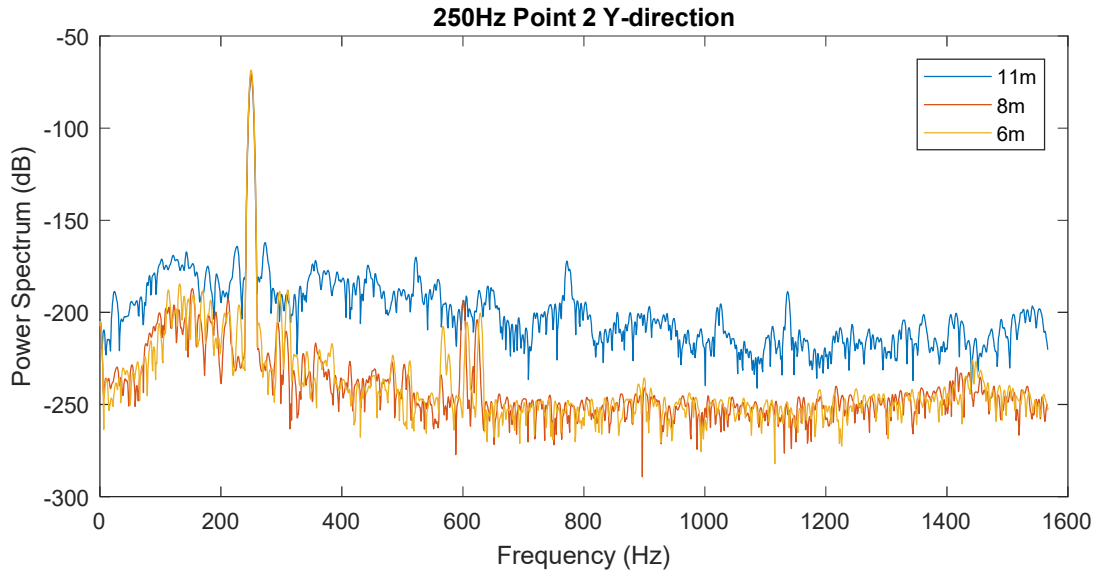


Figure B-41: PSD for 250 Hz at Point 2 in y-direction

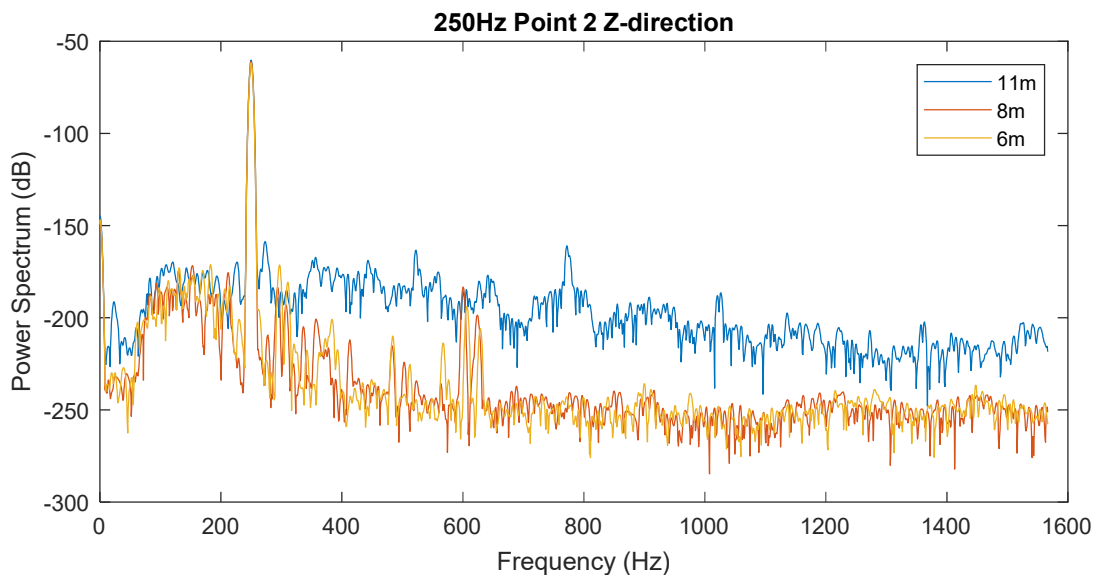


Figure B-42: PSD for 250 Hz at Point 2 in z-direction

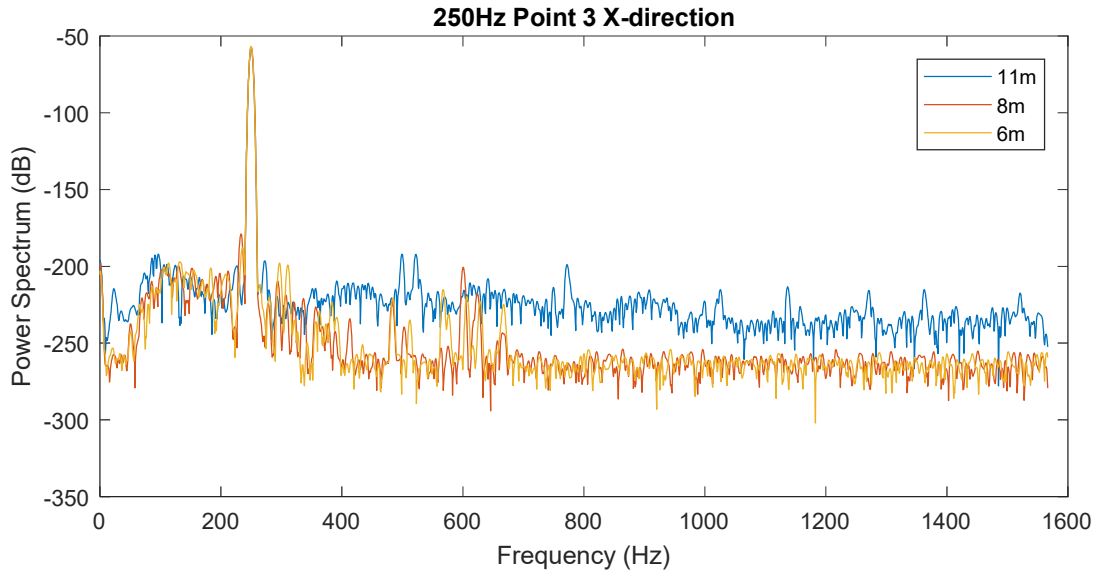


Figure B-43: PSD for 250 Hz at Point 3 in x-direction

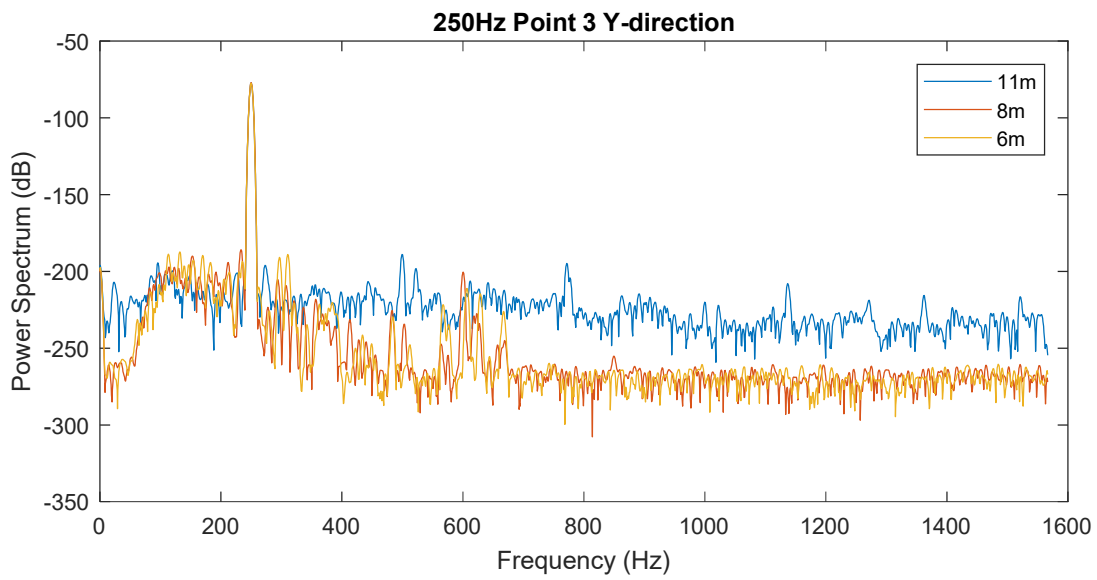


Figure B-44: PSD for 250 Hz at Point 3 in y-direction

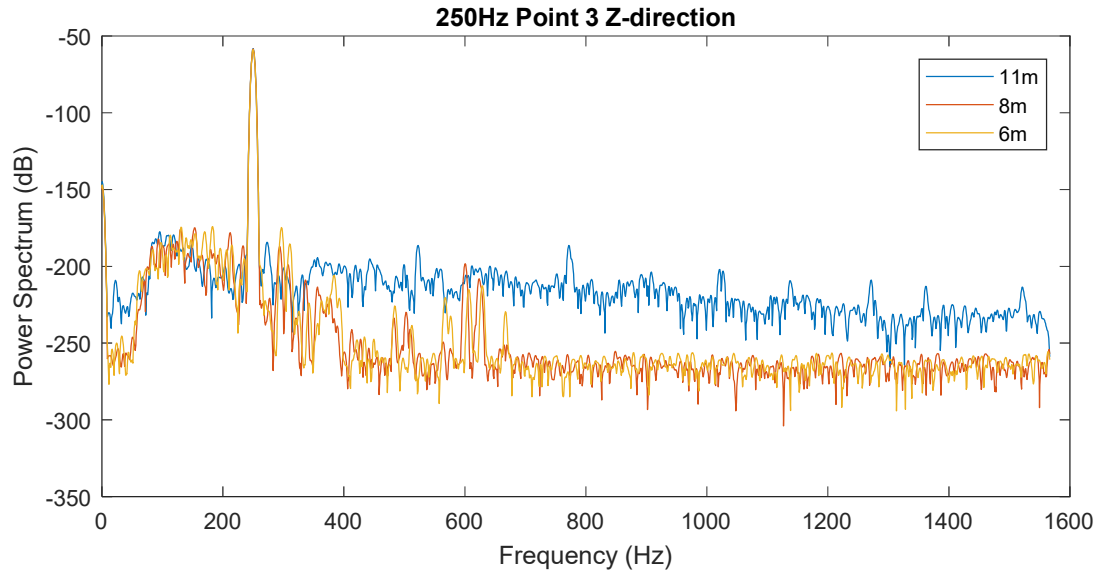


Figure B-45: PSD for 250 Hz at Point 3 in z-direction

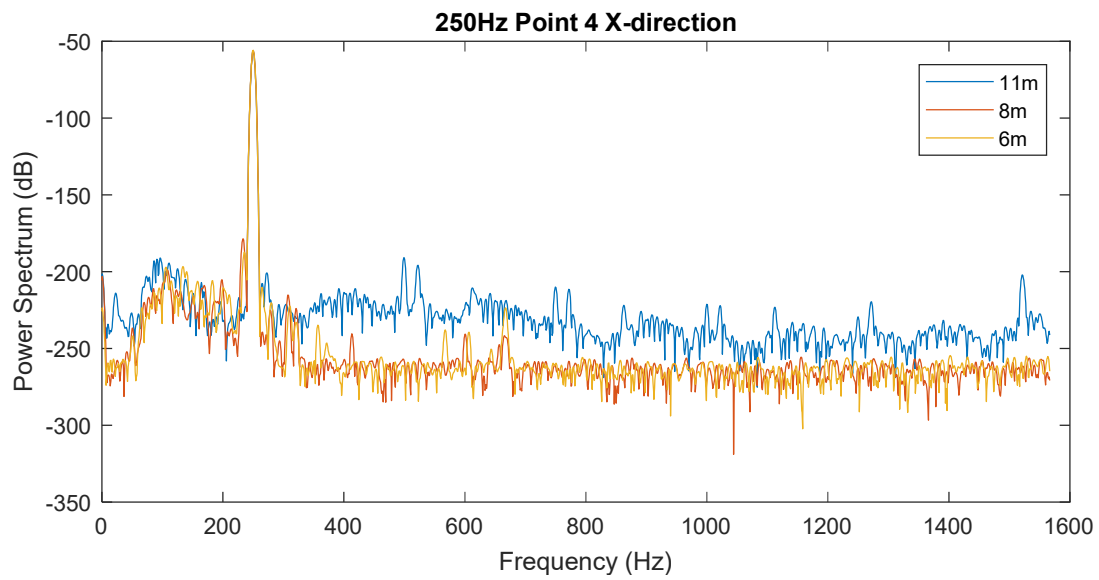


Figure B-46: PSD for 250 Hz at Point 4 in x-direction

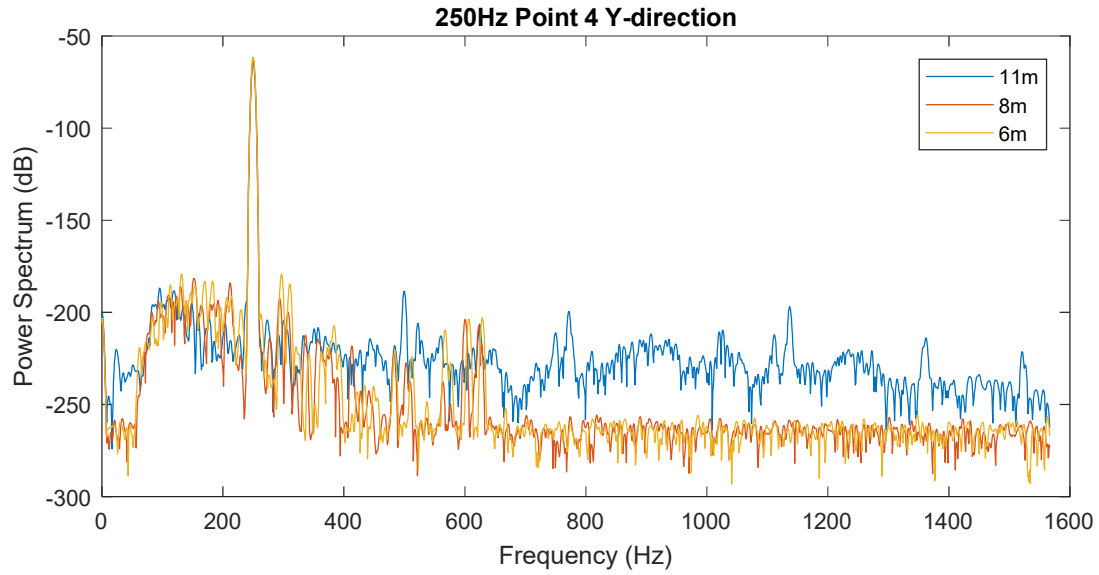


Figure B-47: PSD for 250 Hz at Point 4 in y-direction

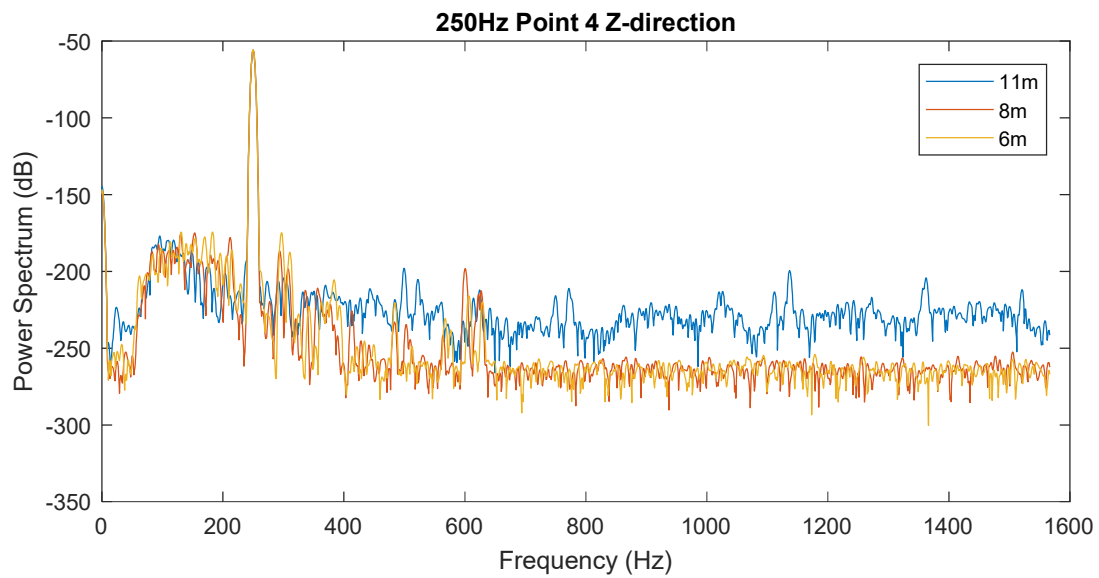


Figure B-48: PSD for 250 Hz at Point 4 in z-direction

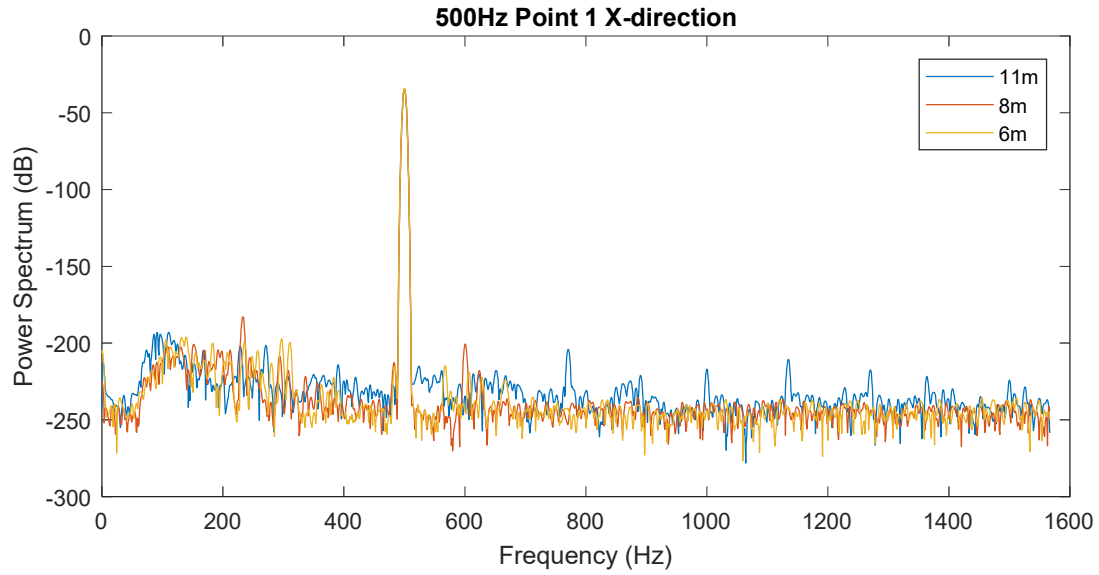


Figure B-49: PSD for 500 Hz at Point 1 in x-direction

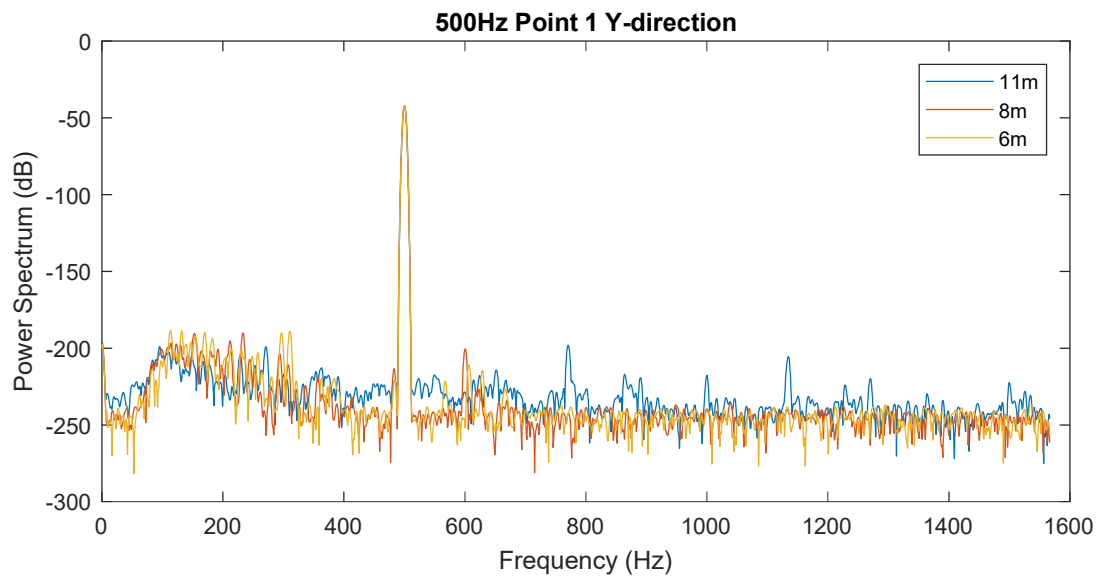


Figure B-50: PSD for 500 Hz at Point 1 in y-direction

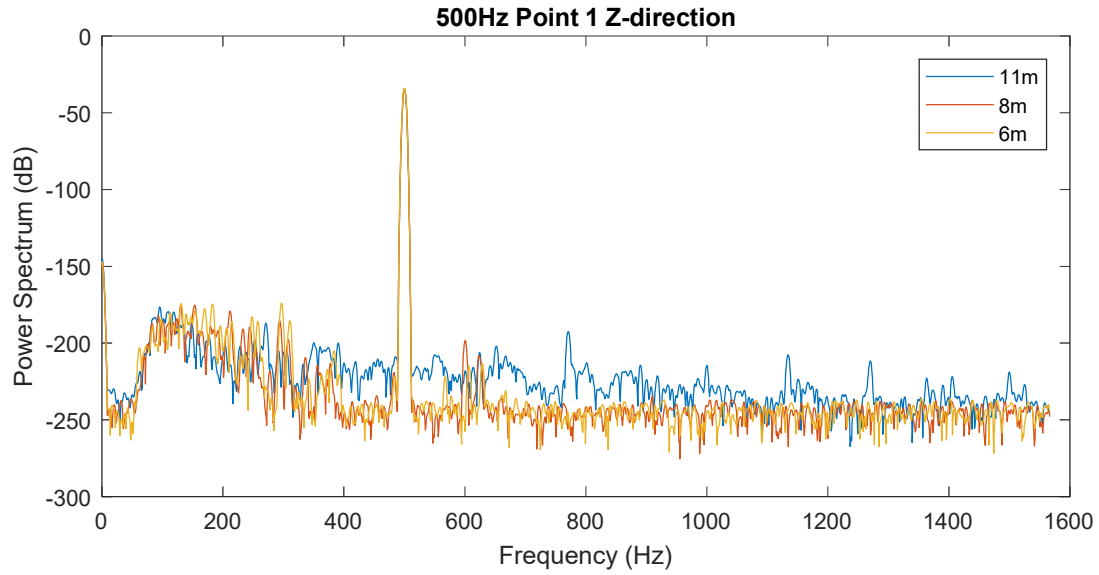


Figure B-51: PSD for 500 Hz at Point 1 in z-direction

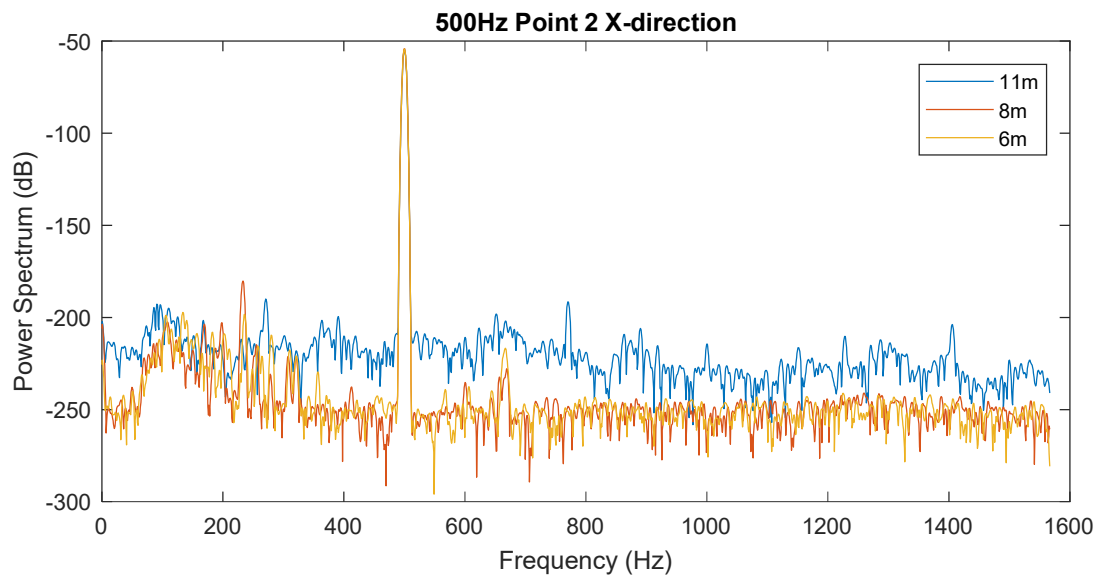


Figure B-52: PSD for 500 Hz at Point 2 in x-direction

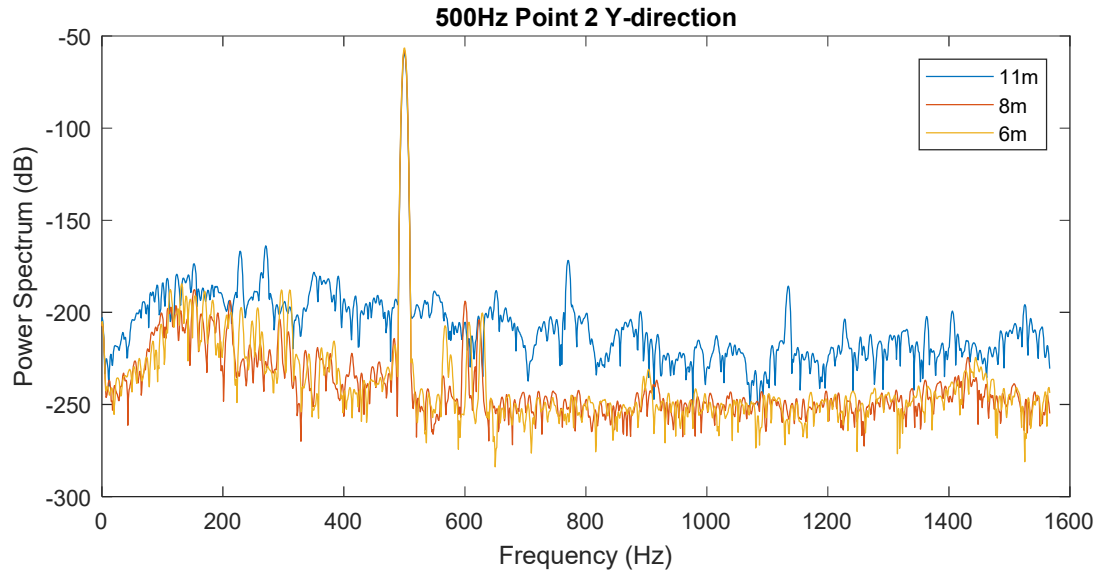


Figure B-53: PSD for 500 Hz at Point 2 in y-direction

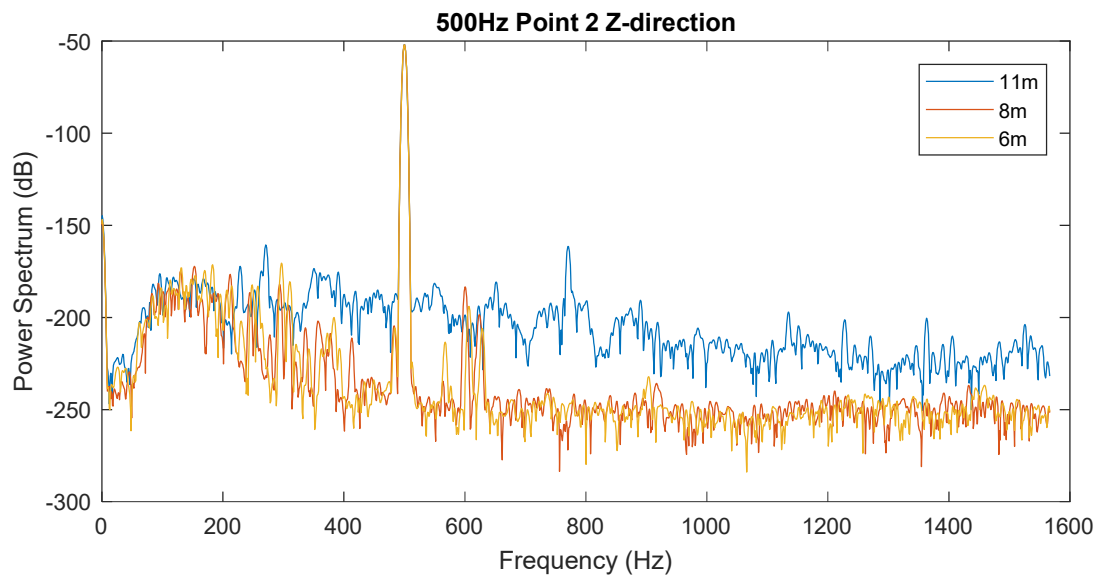


Figure B-54: PSD for 500 Hz at Point 2 in z-direction

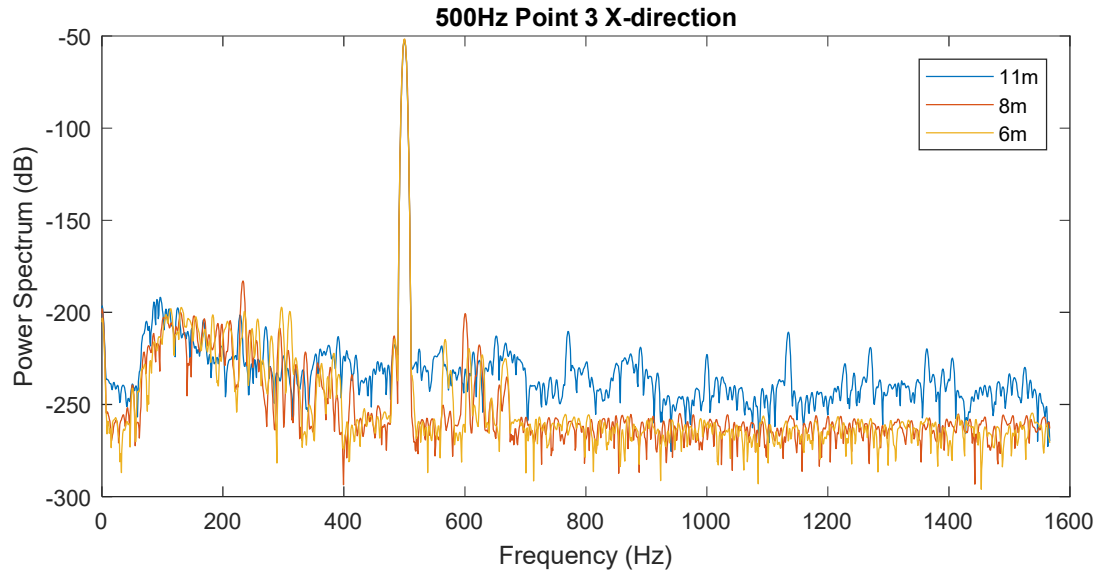


Figure B-55: PSD for 500 Hz at Point 3 in x-direction

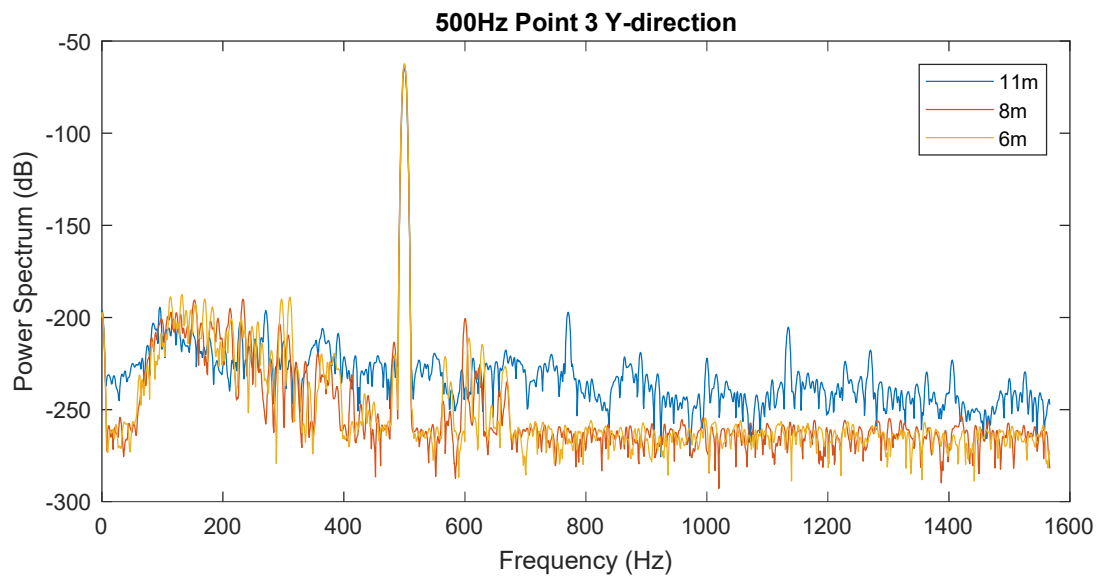


Figure B-56: PSD for 500 Hz at Point 3 in y-direction

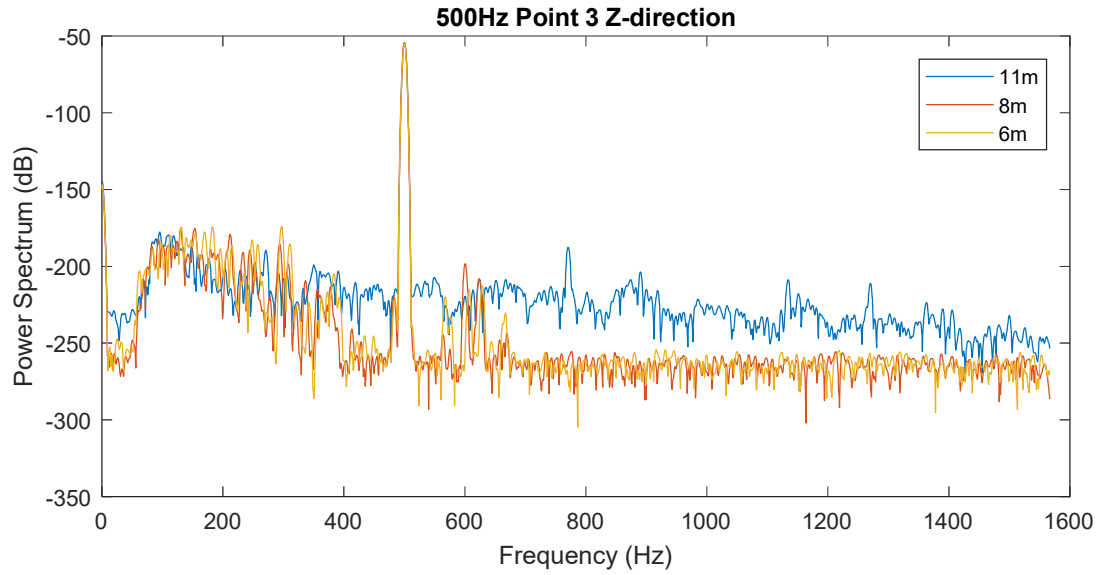


Figure B-57: PSD for 500 Hz at Point 3 in z-direction

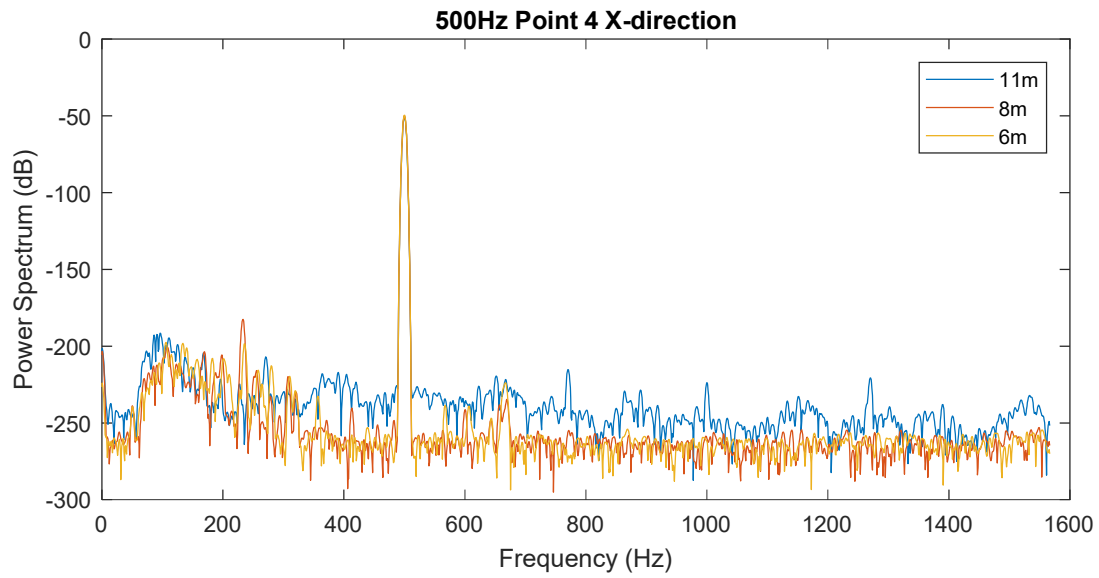


Figure B-58: PSD for 500 Hz at Point 4 in x-direction

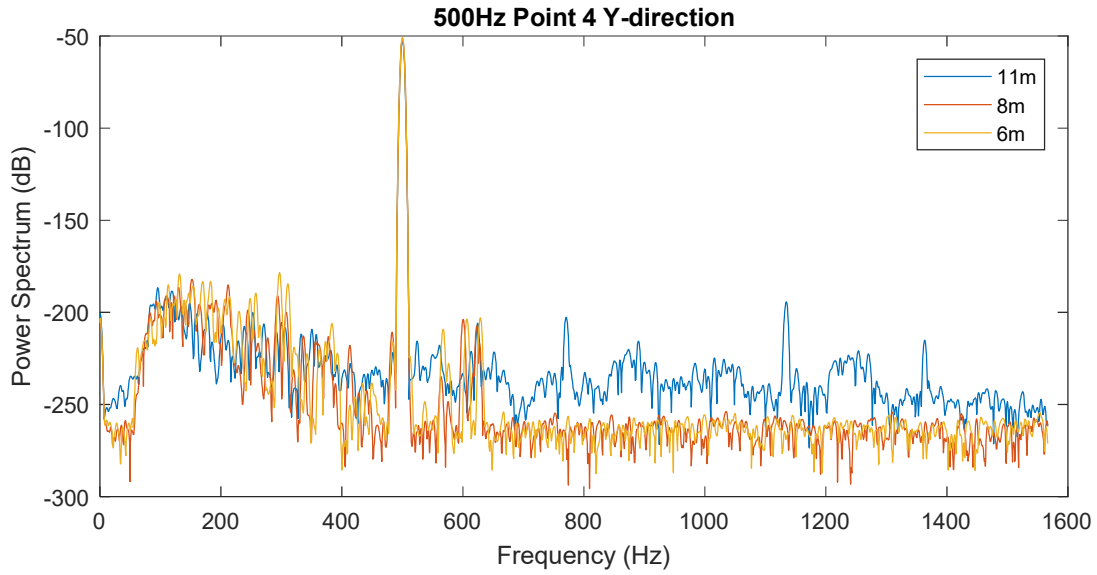


Figure B-59: PSD for 500 Hz at Point 4 in y-direction

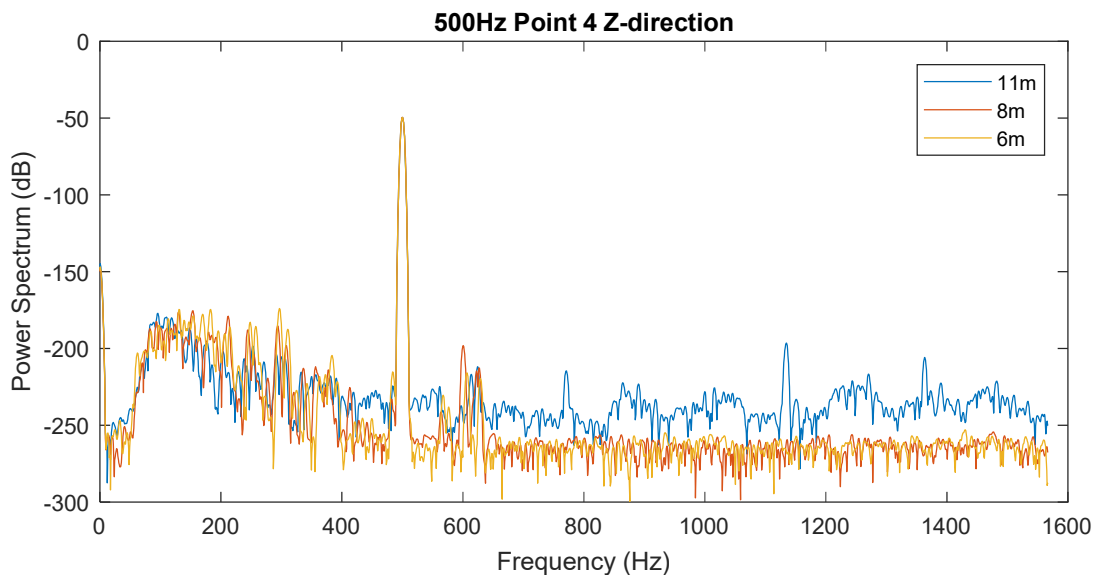


Figure B-60: PSD for 500 Hz at Point 4 in z-direction